

USING SKIN-MOUNTED MICROPHONES FOR RECONSTRUCTING
IN VIVO INTERSKELETAL FORCES:
A FEASIBILITY STUDY

by

BRANDON COLE MCCHRISTIAN

W. STEVE SHEPARD, COMMITTEE CHAIR
KEITH A. WILLIAMS
TODD J. FREEBORN

A THESIS

Submitted in partial fulfillment of the requirements
for the degree of Master of Science
in the department of Mechanical Engineering
in the Graduate School of
The University of Alabama

TUSCALOOSA, ALABAMA

2020

Copyright Brandon Cole McChristian 2020
ALL RIGHTS RESERVED

ABSTRACT

This study investigates the feasibility of using a non-invasive external measurement technique utilizing microphones on the surface of human skin to enable characterization of forces transferred through bone structures during natural motion. While the measurement of forces within the skeleton during human movement is of great interest to researchers and clinicians alike, the requirement for non-invasive sensors does not allow for direct measurement of these forces. The conventional inverse dynamical method of determining internal bone-on-bone forces in biomechanics can be limiting due to the necessity of performing measurements in a laboratory environment and the reliance on a link-segment model, which tends to propagate error. The novel method investigated in this study involves the measurement of pressure waves that propagate through human soft tissue during dynamic loading of the skeletal frame. This research uses a simplified anatomical test specimen consisting of a hollow aluminum bar cast in ballistic gelatin, representing a femur and the surrounding soft tissues, to experimentally examine the feasibility of this new measurement technique. In these tests, an impact force representing interskeletal forces is applied to the bar with an impact hammer and surface-mounted electret microphones measure the resulting pressure waves transferred to the surface of the ballistic gel. Feasibility of the measurement technique was determined by applying least squares regression fits to measured acoustic autospectral data treated as a function of impact force characteristics in the time-domain. The acoustic autospectral amplitudes and energy in frequency bands were found to be highly correlated with both the peak impact force and impulse. Ultimately, results

show that the measurement technique is feasible, thus providing a motivation for the development of more advanced inverse methods utilizing this measurement technique.

DEDICATION

This thesis is dedicated to my parents. Thank you for supporting me throughout my college career and all of my other endeavors.

I would also like to thank so many of my friends who have provided me with every kind of support imaginable, including reading through this paper for edits. Some specific people I would like to mention for their support are Austin Raney, Jonathan Cappola, and Nikki Frazer.

LIST OF ABBREVIATIONS AND SYMBOLS

<i>a</i>	Acceleration (m/s ² , ft/s ²)
<i>AC</i>	Alternating Current
<i>AIC</i>	Akaike Information Criterion
<i>BIC</i>	Bayesian Information Criterion
<i>BK</i>	Brüel & Kjær
<i>COM</i>	Center of Mass
<i>d</i>	Distance measurement (mm, in)
<i>DAQ</i>	Data Acquisition (System)
<i>dB</i>	Decibel
<i>F</i>	Force (N, lb _f)
<i>FBD</i>	Free Body Diagram
<i>FE</i>	Finite Element
<i>FFT</i>	Fast Fourier Transform
<i>FRF</i>	Frequency Response Function

g	Gravitational constant (m/s^2 , ft/s^2)
GRF	Ground Reaction Force
$h(t)$	Impulse response function
$H(f)$	Frequency response function
I_0	Moment of inertia about center of mass ($\text{kg} \cdot \text{m}^2$, $\text{lb}_f \cdot \text{ft} \cdot \text{s}^2$)
ID	Inner Diameter (mm, in)
IP	In-Plane
IRF	Impulse Response Function
J	Impulse ($\text{N} \cdot \text{s}$, $\text{lb}_f \cdot \text{s}$)
m	Mass (kg , lb_m)
M	Moment ($\text{N} \cdot \text{m}$, $\text{lb}_f \cdot \text{in}$)
$MEMS$	Microelectromechanical System
$MDOF$	Multi Degree of Freedom
OD	Outer Diameter
OOP	Out-of-Plane
P	Pressure (Pa)
P_{ref}	Reference pressure level ($20 \mu\text{Pa}$)
RMS	Root Mean Square

R	Reaction force (N, lb _f)
R^2_{adj}	Adjusted coefficient of determination
SPL	Sound Pressure Level
t	Time (sec)
$x(t)$	System input
$X(f)$	Frequency response of system input
$y(t)$	System output
$Y(f)$	Frequency response of system output
α	Angular acceleration (rad/sec ²)
$\delta(t)$	Dirac delta function
Δt	Time difference (sec)
θ	Angular displacement (rad, °)
\mathcal{F}	Fourier operator
*	Convolution operator

ACKNOWLEDGEMENTS

This thesis was supported with funding from the University of Alabama through the Graduate Council Fellowship.

Thank you to my advisor, Steve Shepard, for all of the guidance and instruction throughout the development of this project. Thank you to the other members of my committee, Keith Williams and Todd Freeborn, for providing their input and expertise. I would also like to thank William “Trip” Taylor for being an outstanding partner to work with and his substantial contributions to this research and paper, including his creation of the mold used to construct the experimental model and generation of engineering drawings of experimental setups used in this paper. Thanks also goes to Caitlin Freeman for her hard work in early development of the project, particularly with development of the physical model used in testing.

CONTENTS

ABSTRACT.....	ii
DEDICATION.....	iv
LIST OF ABBREVIATIONS AND SYMBOLS	v
ACKNOWLEDGEMENTS.....	viii
LIST OF TABLES.....	xiii
LIST OF FIGURES	xvii
CHAPTER 1. INTRODUCTION.....	1
CHAPTER 2. LITERATURE REVIEW AND THEORETICAL BACKGROUND.....	4
2.1 The Conventional Method of Determining Internal Bone Forces.....	4
2.2 Motivation for a Novel Inverse Method.....	7
2.3 Excitations of the Lower Body During Locomotion Modeled as an Impulse	11
2.4 Vibrations of Bone: Impulse and Frequency Response	14
2.5 Ballistics Gel as a Soft Tissue Analog.....	18
2.6 Acoustic Measurement of Body Sounds	20
2.7 Background Summary.....	21
CHAPTER 3. EXPERIMENTAL SETUP	23

3.1	Physical Model.....	23
3.1.1	Physical Model Dimensions	24
3.1.2	Physical Model Construction: Gelatin Mixing and Casting	27
3.1.3	Physical Model Boundary Conditions	28
3.2	Testing Configurations and Instrumentation.....	29
3.2.1	Electret Microphone Drive Circuit and Calibration.....	30
3.2.2	Noise Threshold Measurements.....	34
3.2.3	Air Gap Device Efficacy.....	37
3.2.4	Feasibility Study Setup	43
3.3	Experimental Setup Summary.....	49
CHAPTER 4. EXPERIMENTAL RESULTS		51
4.1	Axial Impact Results	52
4.1.1	Axial Impact Regression Models.....	62
4.1.2	Autospectral Amplitudes as a Function of Peak Force	63
4.1.3	Energy in a Frequency Band as a Function of Peak Force	69
4.1.4	Autospectral Amplitude as a Function of the Primary Impulse.....	72
4.1.5	Energy in a Frequency Band as a Function of the Primary Impulse	74
4.1.6	Axial Impact Results Summary	76
4.2	Transverse Impact with In-Plane Measurements	77
4.2.1	IP Transverse Impact Regression Models.....	82

4.2.2	Autospectral Amplitude as a Function of Peak Force	83
4.2.3	Energy in a Frequency Band as a Function of Peak Force	85
4.2.4	Autospectral Amplitude as a Function of Primary Impulse.....	87
4.2.5	Energy in a Frequency Band as a Function of Primary Impulse	89
4.2.6	Transverse IP Impact Results Summary	90
4.3	Transverse Impact with Out-of-plane Measurements	91
4.3.1	OOP Transverse Impact Regression Models	96
4.3.2	Autospectral Amplitude as a Function of Peak Force	96
4.3.3	Energy in a Frequency Band as a Function of Peak Force	98
4.3.4	Autospectral Amplitude as a Function of Primary Impulse.....	99
4.3.5	Energy in a Frequency Band as a Function of Primary Impulse	101
4.3.6	Transverse OOP Impact Results Summary.....	102
CHAPTER 5. CONCLUSIONS AND RECOMMENDATIONS		103
5.1	Conclusions	104
5.2	Future Direction Recommendations.....	106
REFERENCES		112
APPENDICES		116
A1.	Ballistic Gelatin Casting Process and Test Conditions	116
A2.	Supplementary Impact Hammer Model Criteria Tables: IP Transverse Impact	118

A3. Supplementary Impact Hammer Model Criteria Tables: OOP Transverse Impact 119

A4. MATLAB Code for Post-Processing and Figure Generation 121

LIST OF TABLES

Table 1. Femoral mean dimensions (Black, 1978) and model dimensions	24
Table 2. Axial Impact Model Criteria for Electret 1: Acoustic Autospectral Amplitude vs. Peak Impact	66
Table 3. Axial Impact Model Criteria for Electret 2: Acoustic Autospectral Amplitude vs. Peak Impact	67
Table 4. Axial Impact Model Criteria for Accelerometer: Acoustic Autospectral Amplitude vs. Peak Impact	67
Table 5. Axial Impact Model Criteria for Impact Hammer: Acoustic Autospectral Amplitude vs. Peak Impact	67
Table 6. Axial Impact Model Criteria for Electret 1: Acoustic Band Energy vs. Peak Impact	70
Table 7. Axial Impact Model Criteria for Electret 2: Acoustic Band Energy vs. Peak Impact	70
Table 8. Axial Impact Model Criteria for Accelerometer: Acoustic Bandwidth Energy vs. Peak Impact	71
Table 9. Axial Impact Model Criteria for Impact Hammer: Acoustic Bandwidth Energy vs. Peak Impact	71
Table 10. Axial Impact Model Criteria for Electret 1: Acoustic Autospectral Amplitude vs. Primary Impulse	72
Table 11. Axial Impact Model Criteria for Electret 2: Acoustic Autospectral Amplitude vs. Primary Impulse	73
Table 12. Axial Impact Model Criteria for Accelerometer: Autospectral Amplitude vs. Primary Impulse	73

Table 13. Axial Impact Model Criteria for Impact Hammer: Autospectral Amplitude vs. Primary Impulse	73
Table 14. Axial Impact Model Criteria for Electret 1: Bandwidth Energy vs. Primary Impulse .	75
Table 15. Axial Impact Model Criteria for Electret 2: Bandwidth Energy vs. Primary Impulse .	75
Table 16. Axial Impact Model Criteria for Accelerometer: Bandwidth Energy vs. Primary Impulse	75
Table 17. Axial Impact Model Criteria for Hammer Impact: Bandwidth Energy vs. Primary Impulse	75
Table 18. Transverse IP Impact Model Criteria for Electret 1: Acoustic Autospectral Amplitude vs. Peak Force	83
Table 19. Transverse IP Impact Model Criteria for Electret 2: Acoustic Autospectral Amplitude vs. Peak Impact	84
Table 20. Transverse IP Impact Model Criteria for Accelerometer: Acoustic Autospectral Amplitude vs. Peak Impact	84
Table 21. Transverse IP Impact Model Criteria for Electret 1: Acoustic Frequency Band Energy vs. Peak Impact Force	85
Table 22. Transverse IP Impact Model Criteria for Electret 2: Acoustic Frequency Band Energy vs. Peak Impact Force	86
Table 23. Transverse IP Impact Model Criteria for Accelerometer: Frequency Band Energy vs. Peak Impact Force	86
Table 24. Transverse IP Impact Model Criteria for Electret 1: Acoustic Autospectral Amplitude vs. Primary Impulse	87
Table 25. Transverse IP Impact Model Criteria for Electret 2: Acoustic Autospectral Amplitude vs. Primary Impulse	88
Table 26. Transverse IP Impact Model Criteria for Accelerometer: Autospectral Amplitude vs. Primary Impulse	88

Table 27. Transverse IP Impact Model Criteria for Electret 1: Acoustic Frequency Band Energy vs. Primary Impulse.....	89
Table 28. Transverse IP Impact Model Criteria for Electret 2: Acoustic Frequency Band Energy vs. Primary Impulse.....	89
Table 29. Transverse IP Impact Model Criteria for Accelerometer: Frequency Band Energy vs. Primary Impulse.....	89
Table 30. Transverse OOP Impact Model Criteria for Electret 1: Acoustic Autospectral Amplitude vs. Peak Force	96
Table 31. Transverse OOP Impact Model Criteria for Electret 2: Acoustic Autospectral Amplitude vs. Peak Impact	97
Table 32. Transverse OOP Impact Model Criteria for Accelerometer: Acoustic Autospectral Amplitude vs. Peak Impact Force	97
Table 33. Transverse OOP Impact Model Criteria for Electret 1: Acoustic Frequency Band Energy vs. Peak Impact Force	98
Table 34. Transverse OOP Impact Model Criteria for Electret 2: Acoustic Frequency Band Energy vs. Peak Impact Force	98
Table 35. Transverse OOP Impact Model Criteria for Accelerometer: Frequency Band Energy vs. Peak Impact Force	98
Table 36. Transverse OOP Impact Model Criteria for Electret 1: Acoustic Autospectral Amplitude vs. Primary Impulse	99
Table 37. Transverse OOP Impact Model Criteria for Electret 2: Acoustic Autospectral Amplitude vs. Primary Impulse	100
Table 38. Transverse OOP Impact Model Criteria for Accelerometer: Autospectral Amplitude vs. Primary Impulse	100
Table 39. Transverse OOP Impact Model Criteria for Electret 1: Acoustic Frequency Band Energy vs. Primary Impulse.....	101

Table 40. Transverse OOP Impact Model Criteria for Electret 2: Acoustic Frequency Band Energy vs. Primary Impulse.....	101
Table 41. Transverse OOP Impact Model Criteria for Accelerometer Acoustic Frequency Band Energy vs. Primary Impulse	101
Table A1.1. Gelatin Temperature and Mass Data During Testing	117
Table A2.1. Transverse IP Impact Model Criteria for Impact Hammer: Autospectral Amplitude vs. Peak Impact.....	118
Table A2.2. Transverse IP Impact Model Criteria for Impact Hammer: Acoustic Band Energy vs. Peak Impact.....	118
Table A2.3. Transverse IP Impact Model Criteria for Impact Hammer: Autospectral Amplitude vs. Peak Impact.....	118
Table A2.4. Transverse IP Impact Model Criteria for Impact Hammer: Acoustic Band Energy vs. Peak Impact.....	119
Table A3.1. Transverse OOP Impact Model Criteria for Impact Hammer: Autospectral Amplitude vs. Peak Impact.....	119
Table A3.2. Transverse OOP Impact Model Criteria for Impact Hammer: Acoustic Band Energy vs. Peak Impact.....	119
Table A3.3. Transverse OOP Impact Model Criteria for Impact Hammer: Autospectral Amplitude vs. Peak Impact.....	120
Table A3.4. Transverse OOP Impact Model Criteria for Impact Hammer: Acoustic Band Energy vs. Peak Impact.....	120

LIST OF FIGURES

Figure 1. Link-segment model and FBD used in inverse dynamics (Winter, 2009)	5
Figure 2. Complete FBD of a segment from a link-segment model (Winter, 2009)	6
Figure 3. Sample force-time curve for a drop height jump (McKay, 2005)	12
Figure 4. Graphical representation of the delta function, $\delta(t)$ (Control Systems, 2017)	13
Figure 5. Model longitudinal cross section with associated dimensions	25
Figure 6. Visible Human Project cross-section A-A location (IMAIOS.com)	26
Figure 7. Visible Human cross-section A-A with labeled femoral and soft tissue outer diameters (IMAIOS.com)	27
Figure 8. Physical model cross-sectional dimensions: Bar inner diameter (ID) and outer diameter (OD) and gel diameter	27
Figure 9. 3D Printed mold used to construct experimental model	28
Figure 10. Experimental model suspended with test line	29
Figure 11. Electret microphone drive circuit repeated from its datasheet (Mouser, 2015)	31
Figure 12. Electret calibration setup utilizing a loudspeaker	32
Figure 13. Autospectra of electret microphones during calibration	33
Figure 14. Electret calibration curves and FRF (H3) for electret microphones	34
Figure 15. Ambient and electrical noise up to 1600 Hz	35
Figure 16. Ambient and electrical noise up to 500 Hz	36

Figure 17. Air gap device cross-sectional view	38
Figure 18. Drawing of air gap efficacy experimental setup.....	39
Figure 19. Experimental setup to determine an air gap cavity’s effect on measurements.....	39
Figure 20. Frequency response (linear) of both electrets and accelerometer below 1200 Hz.	41
Figure 21. Frequency response (dB) below 1200 Hz for all sensors	41
Figure 22. Frequency response (dB) below 500 Hz for all sensors	42
Figure 23. Normalized frequency response below 500 Hz for all sensors	43
Figure 24. Sensor dimensional locations for analog experimental setup.....	44
Figure 25. Feasibility study setup with electrets and accelerometer labeled	45
Figure 26. Solidworks modal analysis: first 6 modal shapes frequencies of aluminum bar.....	46
Figure 27. Impact orientation for axial, IP transverse, and OOP transverse impacts and relative sensor array placement.....	48
Figure 28. Sample time data of impact hammer for three axial impacts with labeled peaks and impulse times	54
Figure 29. Sample time data of Electret 1 for three axial impacts.....	55
Figure 30. Autospectrum of Electret 1 signal for three axial impacts ($f \leq 1200$ Hz)	56
Figure 31. Autospectrum (dB) of Electret 1 signal for three axial impacts ($f \leq 1200$ Hz)	56
Figure 32. Autospectrum (dB) of Electret 1 signal for three axial impacts ($f \leq 500$ Hz)	57
Figure 33. Autospectrum (dB) of Electret 2 signal for three axial impacts ($f \leq 500$ Hz)	58
Figure 34. Vibration response of accelerometer signal for three axial impacts ($f \leq 10,000$ Hz)...	60
Figure 35. Vibration response of accelerometer signal for three axial impacts ($f \leq 500$ Hz).....	61

Figure 36. Linear model of Electret 1 autospectrum magnitude at 160 Hz as a function of peak impact force	64
Figure 37. Linear model of Electret 2 autospectrum magnitude at 160 Hz as a function of peak impact force	64
Figure 38. Quadratic model of Electret 1 autospectrum magnitude at 160 Hz as a function of peak impact force	65
Figure 39. Quadratic model of Electret 2 autospectrum magnitude at 160 Hz as a function of peak impact force	65
Figure 40. Sample time data of impact hammer for three transverse IP impacts with labeled peaks and impulse times	78
Figure 41. Sample time data of Electret 1 for three IP transverse impacts.....	79
Figure 42. Autospectrum (dB) of Electret 1 signal for three IP transverse impacts ($f \leq 500\text{Hz}$). 80	
Figure 43. Autospectrum (dB) of Electret 2 signal for three IP transverse impacts ($f \leq 500\text{Hz}$). 80	
Figure 44. Vibration response of accelerometer signal for three IP transverse impacts ($f \leq 500\text{Hz}$).....	82
Figure 45. Sample time data of impact hammer for three transverse impacts with OOP measurements with labeled peaks and impulse times.....	92
Figure 46. Sample time data of Electret 1 for three OOP transverse impacts	92
Figure 47. Autospectrum (dB) of Electret 1 signal for three OOP transverse impacts ($f \leq 500\text{Hz}$).....	93
Figure 48. Autospectrum (dB) of Electret 2 signal for three OOP transverse impacts ($f \leq 500\text{Hz}$).....	94
Figure 49. Vibration response of accelerometer signal for three OOP transverse impacts ($f \leq 500\text{Hz}$).....	95

Figure 50. A 3 x 3 microphone array with would symmetrical axial placements and
45-degree radial offsets 109

CHAPTER 1. INTRODUCTION

The need for non-invasive measurement techniques in biomechanical analysis is apparent, and the development of such methods is central to the progress of the analysis of *in vivo* systems. This need for non-invasive measurements results from the ongoing desire to better understand forces inside the human body during various forms of uninhibited skeletal motion, as this information can aid doctors, therapists, sports trainers, assistive technology developers, and others working in related fields. Common types of analyzed human motion include walking, running, and jumping from a drop height. Often, the goal of biomechanical analyses of these motions is to estimate internal forces transferred through joints via the skeletal structure in order to infer information about the musculoskeletal health or performance of a subject. The study described in this thesis tests the feasibility of using skin-mounted microphones to measure pressure waveforms propagating through soft tissue in order to infer information about, or reconstruct, the impulse force transferred between bones in an accurate and non-invasive manner during natural movement.

Prior to an in-depth discussion of the new approach examined here, it is worth further reviewing the inverse dynamic method typically used to determine internal bone forces. This quick review helps provide the motivation for the proposed work as well as introduce the techniques that must be understood prior to evaluating the feasibility of the new experimental technique evaluated in the current work. The conventional approach to inferring internal forces transferred through joints via the bone structure applies an inverse dynamic method. A detailed

explanation of how this model is applied to a biomechanical system and a synopsis of its limitations are given in Sections 2.1 and 2.2, respectively. These limitations highlight the need for a new measurement technique, such as the one under consideration in this study. The choice of investigating acoustic measurements as a tool for determining internal bone forces is outlined in Sections 2.3 and 2.4. While this particular application of acoustics in biomechanics is novel, the usage of acoustic measurements of body sounds as a diagnostic tool in biological systems is summarized in Section 2.6.

The focus of the current work is to show that measured acoustic pressure waves on the skin's surface can possibly be used as part of an inverse method to predict internal bone forces. In order to present the challenges associated with this, it is best to explain how an internal force relates to a measurable acoustic signal at the skin's surface. First, a biomechanical motion causes internal bone structures to collide with one another, causing them to vibrate. This vibration then induces wave motion in the viscoelastic soft tissues that surround the bones. The induced waveforms propagate through the viscoelastic tissues, causing the skin at the surface to vibrate. Resulting skin vibrations then create small acoustic pressure waves, which are measured by the microphones on the skin's surface. This process of generating resultant pressure waves in air from a vibrating bone is very complex in nature. Factors which might affect the ability to correlate the measured acoustic signal with internal bone forces include the complex nature and material properties of viscoelastic soft tissues and how waves are transmitted at boundary layers, such as at the skin-air interface. Boundary layers may cause transmission loss and reflection of the propagating waves. These combined factors lead to difficulty in utilizing a numerical model to determine the feasibility of the measurement technique proposed. Therefore, an experimental approach was adopted here to determine the feasibility of correlating forces within

musculoskeletal structures of the human body with acoustic measurements taken at the skin's surface.

The assumptions for the physical model tested in this study are based on the kinetics and kinematics of some motions commonly studied in biomechanics, such as jumping from a drop height, as discussed in Section 2.3. In this study, a system composed of a hollow aluminum bar cast inside of a ballistic gel was used as a simplified analog structure representative of a femur and its surrounding tissue. The similarity in properties of human soft tissues and the ballistics gel used in this study is discussed in Section 2.5. Although this gel structure still has non-linear dynamic properties, it is hoped that the system can still be analyzed in the frequency-domain in order to apply a potential inverse method, briefly summarized in Section 2.3, but left to future work to develop. By constructing the physical model used in this study, the complexities associated with considering a non-homogeneous leg model were eliminated, allowing focus to be placed on the effect of the mechanical properties of soft tissues on the ability to measure the acoustic signal transmitted to the skin's surface originating from a vibrating bone structure. During testing on the analog model, an impact hammer was used to excite the internal bar structure (*i.e.* bone), and the electret microphones on the surface of the gel measured the resulting pressure waves generated by the vibrating bar system. A linear least squares regression was then used to determine the correlation between the measured sound signal autospectrum and the peak impulse magnitude of the excitation, which was measured using the instrumented impact hammer. Ultimately, it is hoped that this study will lead to the development of a new method to accurately and non-invasively better understand forces within humans during biomechanical motion.

CHAPTER 2. LITERATURE REVIEW AND THEORETICAL BACKGROUND

This chapter outlines the motivation for the development of the proposed measurement method as well as explains how the experimental setup was developed in order to best determine the method's feasibility. The first section presents how internal forces are conventionally determined during biomechanical analysis through the inverse dynamic method and the second section explores the conventional method's shortcomings, highlighting the motivation behind developing a new inverse method. The third and fourth sections jointly show how the measurement technique investigated in this study might be used within the framework of an inverse method in which a long bone within the body is treated as a Multi Degree of Freedom (MDOF) dynamic system excited by an impulse. The determination of feasibility for the proposed measurement technique is also discussed in the third and fourth sections, based on metrics associated with characterization of the MDOF dynamic system in the frequency-domain. The fourth and fifth sections jointly assert the assumptions made for the physical model used in the current feasibility study. The final section gives an overview of how acoustic measurements have been applied to body sounds, which are in the most general sense, sounds generated by movement of the human body.

2.1 The Conventional Method of Determining Internal Bone Forces

The conventional method of determining interskeletal forces in the lower body during biomechanical motion applies inverse rigid body dynamics to a link-segment model of the human body. This method has been used to estimate bone-on-bone contact forces in the

tibiofemoral joint during walking (Thambyah, 2005), and to determine compressive tibiofemoral force during crouch gait in individuals with cerebral palsy (Steele, 2012). An overview of how this method is applied is provided next.

A link-segment model is a two-dimensional system of inter-connected rigid bodies characterized by length, mass, center of mass (COM), and moment of inertia. In the case of a biomechanical system, limbs are discretized into segments and anatomical joints are represented by hinge joints. Bone segments are assumed to be rigid bodies with a mass and moment of inertia located at the segment's centroid. Figure 1 shows an example of a free body diagram of a two-dimensional link-segment model representative of the lower body.

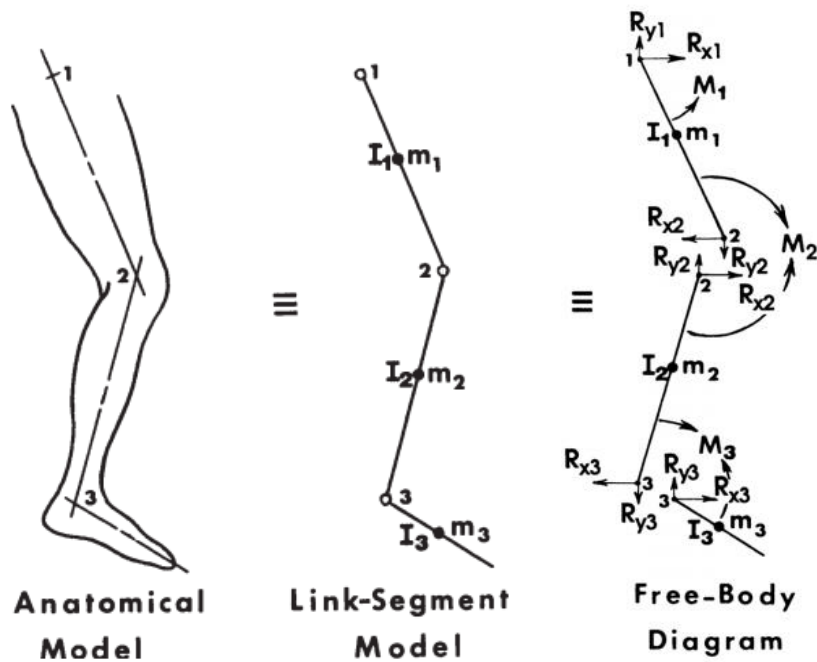


Figure 1. Link-segment model and FBD used in inverse dynamics (Winter, 2009)

Figure 2 shows the complete FBD of a single segment, inclusive of all joint reaction forces and moments, COM acceleration components, gravitational forces, and anthropometric dimensions. R_{xp} and R_{yp} represent the x and y components of the forces at the proximal end of the segment, respectively. Similarly, R_{xd} and R_{yd} represent the respective x and y components of the forces at the distal end of the segment. M_p and M_d are the moments applied at the proximal and distal joints, respectively. The weight, mg , of the segment is applied at point m representative of the centroid of the segment, located at distance d_1 from the distal joint. Finally, joint angle θ is measured in the positive sense as counterclockwise from level ground and angular acceleration of the segment about its COM is denoted as α .

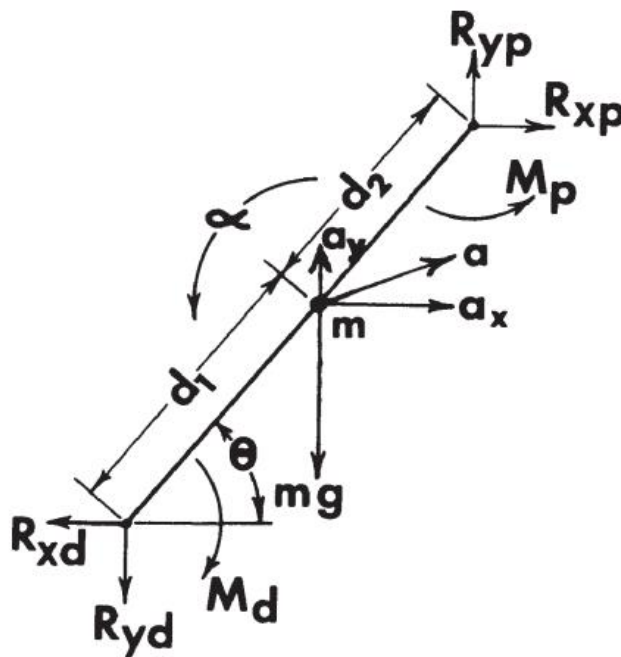


Figure 2. Complete FBD of a segment from a link-segment model (Winter, 2009)

Inverse rigid body dynamics refers to the process of inferring the forces and/or moments present within a link-segment model based on the measured kinematics of the segments in the

system. The inverse dynamic method is applied to a biomechanical system by tracking the kinematic data of the limbs using attached reflective markers via a vision system and measuring the Ground Reaction Force (GRF) using force plates. The measured motion and GRF are then used to analytically reconstruct internal forces as described next.

The first step to reconstructing the internal forces transferred between bones is to treat the GRF as a known input to the distal end of the segment in contact with the ground. The forces and moments at the proximal end of the first segment can then be solved using the Newton-Euler equations of motion such that

$$\sum F_x = ma_x, \quad (1)$$

$$\sum F_y = ma_y, \quad (2)$$

and

$$\sum M = I_0 \alpha, \quad (3)$$

where a_x and a_y are the x- and y-components of the acceleration of the link COM, respectively, and I_0 is the moment of inertia about the segment's COM. After solving for the forces and moments at the proximal end, those values are then used as the input forces to the next segment. This process is applied iteratively to solve for the internal forces at the joints. While straightforward from a calculation standpoint, this method has limitations when it comes to reconstructing *in vivo* forces, discussed in more detail in the next section.

2.2 Motivation for a Novel Inverse Method

This section outlines the motivation for developing a new method of determining internal forces transferred through joints. While the inverse dynamic approach discussed in the previous

section is relatively simple and straightforward, it has limitations related to the logistics of the measurement techniques used to capture data, measurement error, and calculation error inherent to the iterative method employed. Furthermore, link-segment models can oversimplify complex musculoskeletal systems, leading to inaccurate determination of internal forces.

Limitations in how data is collected in order to apply the inverse dynamic method show how cumbersome it can be when it comes to taking data outside of a laboratory environment. The inverse dynamic method requires measuring the GRF, typically with a force plate, and gathering kinematic data with optical sensors by tracking joint centers with attached reflective markers. The need for force plates to measure the GRF and vision systems to track joint markers typically limit the use of inverse dynamic methods to a lab environment. In addition, the number of markers required for motion tracking is significant. According to Wong et al. (2015), in order to simplify biomechanical analysis, developments must be made to reduce the number of sensors required, as well as allow for the ability to take measurements during regular activity outside of a lab environment. Though some advances have been made in developing technologies that increase the portability of measurement systems, these systems are not standard in biomechanical analysis and not yet widely used. Since the conventional inverse dynamic methodology will always require measurement of the GRF and marking of multiple joint centers, it will be difficult to have fewer sensors and the ability to take measurements during regular activity outside of a lab environment without developing new techniques with which to determine internal forces. It is the hope that the method proposed in this study utilizing electret microphones mounted on the surface of the skin will prove feasible and will therefore provide an alternate method that is less cumbersome with respect to data collection.

Apart from logistical challenges associated with the conventional method of determining internal forces, the link-segment model is also very prone to error in force estimations due to measurement error and compounding calculation errors related to its iterative solving process. A source of measurement error associated with the conventional inverse dynamic method comes from the gathering of kinematic data, particularly with respect to the difficulty of placing motion-tracking markers directly on joint centers. This error is due to the marker being placed on fat or muscle tissues and not necessarily being rigidly affixed to a precise location on the bone. Errors due to inaccurate marker placement are exacerbated when working with obese subjects due to difficulty in locating anatomical landmarks (Sebo, 2017). The accuracy of forces estimated using the inverse dynamic approach is also limited by the accuracy of measurements of the geometric and mass properties of its constitutive segments. While length of body segments can be determined for subjects via x-ray, this determination can be impeded by cost or lack of available equipment. If x-rays are not used, segment length is not so easily determined by direct measurement due to uncertainty in locating anatomical joint centers. Furthermore, segment mass must either be determined by a combination of a bone-density scan and x-ray, which is again potentially limiting due to cost or availability of equipment, or by estimating via anthropometric tables (Winter, 2009). If mass is estimated by utilizing anthropometric tables, inaccuracies occur due to biologic variation (Mony, 2016). These errors mentioned with respect to measurement unique to the link-segment model are not inclusive of other errors associated with instrumentation measurement uncertainties. Regardless, either case of measurement error is problematic when it comes to using them in the link-segment model's analytical method used to solve for internal forces.

Errors in the calculation of internal forces in the link-segment model can come from the iterative process of solving for joint forces, where errors are compounded due to using the output forces and moments from one link as input forces and moments for subsequent links in the model. In other words, even small errors in forces or moments calculated at the distal end of the link-segment chain can greatly exacerbate the error in calculations of forces and moments in later segments.

Sources of error when calculating internal forces via the conventional inverse dynamic method can also occur due to elimination of force and moment contributions of the muscular system. For example, joint reaction forces in a link-segment model are typically treated as being directly representative of compressive bone-on-bone forces due to an assumption that the applied moment at each joint is generated by a torque motor (Winter, 2009). These moments are in fact created by retraction of muscle tissue acting as a linear motor. This assumption leads to a lack of representation of forces generated by muscles in the model that are in fact acting at joints within the real system (Winter, 2009). Accounting for muscular forces in order to improve a link-segment model's accuracy is not straightforward due to high variance in muscle and tendon size across subjects. Furthermore, an attempt to accurately represent the muscles and tendons would introduce substantial complexity due to factors like the complex material properties of soft tissue (Pal, 2016) and adjustment of tissue properties by the central nervous system during prolonged activity (Nikooyan, 2012). Particularly with respect to the adjustment of tissue properties, these factors are not yet very well understood. While the measurement method proposed in the current work may also be affected by these properties of soft tissues, the manner in which the novel measurement method is affected would be fundamentally different than the conventional approach and could potentially be overcome. In particular, the current work seeks to determine

the extent to which viscoelastic properties of soft tissues might affect the measurement of acoustic waves that propagate through them.

This section described some of the most pronounced limitations of the inverse dynamic method conventionally used in determining internal forces transferred between bones during human movement, making the motivation for developing a new method clear. These shortcomings of the inverse dynamic method are by no means an exhaustive list but are a focus of this section since most are ameliorated by the method proposed in this study, should it prove to be feasible. This study investigates the efficacy of a method of extrapolating information about forces transferred between bones, such as their magnitude, during mechanical excitation caused by certain types of human motion. It is important to therefore discuss the representation of the forces transferred between bones as an impulse excitation and the physical significance of a bone's vibration response and subsequently generated pressure waves, as it relates to the amplitude of an impulse excitation.

2.3 Excitations of the Lower Body During Locomotion Modeled as an Impulse

The impulsive nature of the GRF that excites the lower body during various common movements is an essential part of the approach considered in this study. It is important to note that the GRF is not the primary force of interest, as it is not the force transferred between bones. However, it is assumed that the GRF impulse is transmitted through rigid bone structures. Thus, the forces between bones are also assumed to be impulsive in nature, though these forces are attenuated as they are transferred through joints.

The characterization of the GRF as an impulse approximates the force-time curves of the GRF during mechanical loading of the lower body during various activities, such as walking,

running, and jumping (Veltink, 2005). An exemplar force-time curve of a GRF produced from jumping from a drop height is repeated from McKay (2005) in Figure 3.

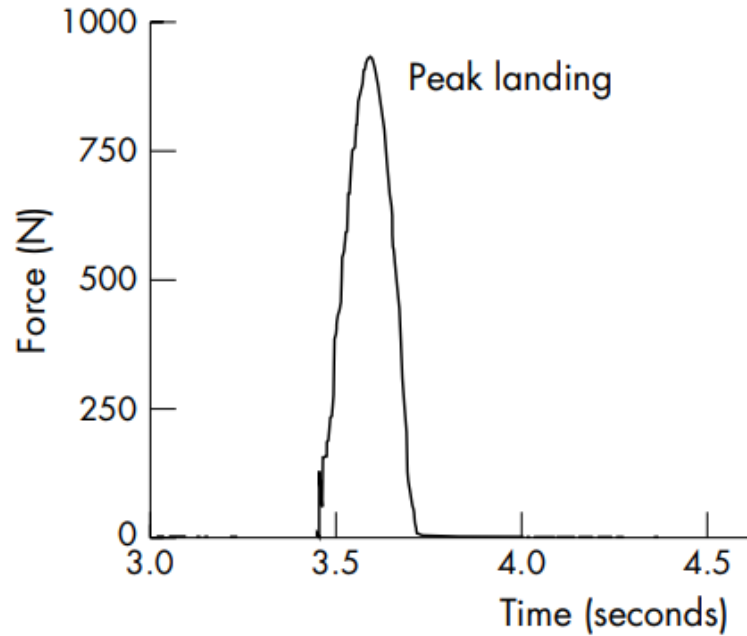


Figure 3. Sample force-time curve for a drop height jump (McKay, 2005)

The impulse (or Dirac delta) function, $\delta(t)$, is defined as a piecewise function such that

$$\delta(t) = \begin{cases} 0, & t < 0 \\ \text{undefined}, & t = 0 \\ 0, & t > 0 \end{cases} \quad (4)$$

and

$$\int_{-\infty}^{\infty} \delta(t) dt = 1. \quad (5)$$

Figure 4 shows the graphical representation of $\delta(t)$ as an arrow towards positive infinity.

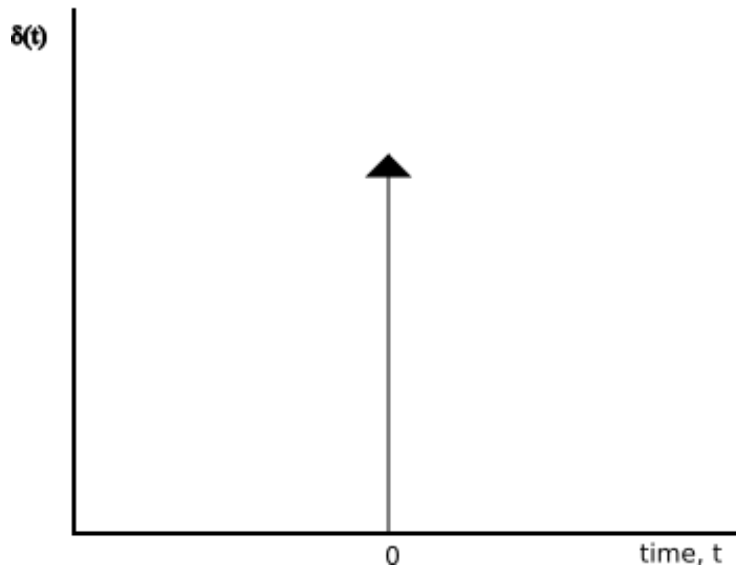


Figure 4. Graphical representation of the delta function, $\delta(t)$ (Control Systems, 2017)

The mathematical representation of the impulse function, while physically impossible to achieve, has a practical significance, expanded on in the next section. It is, however, important to note that the GRF's transient force-time curve shown in Figure 3 will be approximated as an impulse due to its large magnitude and the short time-span in which it occurs, although it may not actually be as such. Though less pronounced, similar GRF force-time curves result from heel strike during walking and running or could otherwise be modeled as a train of impulses. For this study, the case of motion for the drop height jump is most appropriate as an approximation as a single impulse.

The impulse generated by the GRF is transferred through the lower body via the skeletal frame, loading the bones compressively. The forces between bones at joints are impulsive in nature, similar to the GRF, but are attenuated. This impulsive force causes bones to vibrate. The vibrations from the bone then propagate through the soft tissue, toward the surface of the skin. By measuring these pressure waves on the surface of the skin using microphones, it is

hypothesized that the *in vivo* forces transferred between bones can be inferred. The next section discusses how the impulse force transferred between bones can be estimated from the measured vibratory response of a bone under ideal conditions in which the vibrations can be directly measured on the bone's surface. While this method cannot be realistically applied due to its invasiveness, it helps to better understand the nature of the waveforms of interest that propagate through soft tissues before being measured at the skin's surface.

2.4 Vibrations of Bone: Impulse and Frequency Response

In the most general sense, a system's vibratory response characterizes its dynamic properties. When the dynamic properties of a system are unknown, as is the case for the biomechanical system under consideration in the current work, the system can be better understood by analyzing the impulse and frequency responses of the system's input and output. This section focuses on how the impulse and frequency responses are relevant to the measurement method proposed in the current study and gives a high-level overview of how the measured signal can be used to infer information related to the input. The equations presented in this section are chosen from *Elements of Vibration Analysis* and are reproduced here as they relate to the current work (Meirovitch, 1975).

In the time domain, the impulse response is related to a system's input and output through the following relation:

$$h(t) = \frac{y(t)}{x(t)}, \quad (6)$$

where $x(t)$ denotes the input to the system, $y(t)$ is the output of the system, and $h(t)$ is the Impulse Response Function (IRF). In the case that the input and impulse response of a time-invariant

system are known, the output can be found through the convolution of the input and impulse response such that

$$y(t) = x(t) * h(t) = \int_{-\infty}^{\infty} x(\tau)h(t - \tau)d\tau, \quad (7)$$

where $*$ indicates the convolution operator and τ is a dummy variable used for integration.

Solving for the output of a system through convolution can be difficult to perform, or impossible when dealing with a system with an unknown impulse response. However, by analyzing a system in the frequency-domain instead of the time-domain, a less computationally involved method can be applied. The Convolution Theorem states that multiplication in the frequency-domain is equivalent to convolution in the time-domain, and vice versa. A signal can be transformed into the complex frequency-domain by applying the Fourier Transform, denoted by the linear operator \mathcal{F} . The Fourier Transform can be applied such that

$$X(f) = \mathcal{F}[x(t)] = \int_{-\infty}^{\infty} x(t)e^{-j2\pi ft} dt, \quad (8)$$

where f is the independent variable in the frequency domain and $X(f)$ is the frequency response of the time-domain signal $x(t)$. By applying the Fourier Transform to a signal, the Convolution Theorem can be applied to determine the output of a system through the relation

$$Y(f) = X(f)H(f), \quad (9)$$

where $H(f)$ is the Frequency Response Function (FRF) of the system. This gives the inverse relation which can be used to easily solve for the input when the output is known such that

$$X(f) = \frac{Y(f)}{H(f)}. \quad (10)$$

The relationship between the input and output in the time- and frequency-domains provides a framework for how an inverse method utilizing the impulse and frequency responses of an output of a system can be used to determine information about the input provided to the system. The system under consideration in the current work, a segment of a biomechanical system, is complex and has an unknown IRF and FRF such that these relationships cannot be directly applied in practice through an inverse method as presented in Equation 10. The development of an inverse method is left to future research after determining the feasibility of the measurement technique under consideration in the current work. However, the linear relationship between the input and output signals in the frequency-domain for a time-invariant linear system is apparent. Thus, one of the methods applied in the current work to show the feasibility of the measurement technique investigated fits least squares linear regression models to the input and output signals' frequency responses at discrete frequencies. The implication is that if the linear correlation between the input and output is strong, then the system can feasibly be analyzed in the frequency-domain. The discrete frequencies targeted in this study to establish a relationship between the input and output include the resonant frequencies of the system, which are commonly used to characterize a dynamic system through modal analysis.

The frequency response of a dynamic system given an excitation, such as an impact, is its modal response. The system's impulse response is dictated by its modal characteristics such that the superposition of all modes will give the impulse response. Therefore, the physical model representative of a biomechanical system developed in this work was based on known modal

characteristics of long bones in the human body. Experimentally determined modal frequencies have been identified for various long bones (bones with significantly large length-to-width ratios) under *in vivo* and *ex vivo* conditions. Within the forearm, the first two *in vivo* ulnar resonances were found to occur at about 250 Hz and 450 Hz by exciting the elbow with a sinusoidal loudspeaker input (Jurist, 1970). These findings agree with the same study's model-predicted fundamental resonant frequency of about 230 Hz based on the representation of the ulna as a vibrating bar. In a separate study by Perre, and Mulier (1983), bending modes of *in vivo* tibiae were estimated at 270 Hz and 340 Hz, corresponding to the first two principal directions of bending. It is likely that the ulnar resonances measured by Jurist et al. (1970) similarly correspond to the first two principal directions of bending. In the lower body, the first five natural frequencies of a femur in free-free boundary conditions were modeled using a Finite Element (FE) model and found to be between 238 and 782 Hz (Campoli, 2015). These FE model estimates of femoral natural frequencies are assumed to be lower in natural conditions due to added mass and damping from muscle tissue (Perre, 1983). The current research's experimental model, representative of a simplified femoral cross-section and surrounding soft tissues, was constructed such that its frequency response consisted primarily of frequencies below 500 Hz, reflecting the expected lowered natural frequencies during *in vivo* measurement. Details of the model constructed for the feasibility testing conducted in this research are given later in Section 3.1.

Some potential inverse methods for characterizing the impulse forces transferred between bones have been presented in order to show how quality measurements of the bone's vibration response might be applied. However, the challenge in properly characterizing the impulse forces lies in measuring the vibrations originating from internal bone structures with sensors on the

surface of the skin. Methods have been proposed that utilize accelerometers attached to the surface of the skin, but motion of the skin, along with accelerometer coupling issues, leads to viable measurements being limited to below the 100 Hz range (Kim, 1993), which does not allow for capture of the vibration response of long bones as described above. The current study instead investigates the utilization of electret microphones on the skin's surface to measure the sound waves originating from vibrating bone structures that propagate through the soft tissue. The use of body sound measurements in the field of biomechanics is discussed in Section 2.6. In order to determine the feasibility of measuring the acoustic signal that propagates through soft tissues, an experimental model was constructed with the intent of approximating the viscoelastic material properties of skin and muscular tissue. The next section discusses how these tissues' complex material properties were considered in development of the physical model.

2.5 Ballistics Gel as a Soft Tissue Analog

In general, a good experimental model exhibits the same dynamic characteristics as the original physical system, however, a physical model is a compromise between the true dynamic behavior of the original system and an achievable representation of that system. The model in the current work approximates a musculoskeletal system's mechanical properties. In the current work, the model's analog for soft tissues surrounding the femur consists of a water-gelatin mixture. This representation of soft tissues allows for the study to determine if the viscoelastic material properties of soft tissues are inhibitive of the ability to measure pressure waves on the skin's surface that originate from internal bone vibrations.

Soft tissues are viscoelastic materials with complex mechanical properties, leading to non-linear behavior and subsequent difficulties in material modeling (Pal, 2014 and Chen, 2013).

Furthermore, these mechanical properties are dependent on time and are constantly changing due to biological factors and environmental factors, such as temperature (Holzapfel, 2001).

Therefore, to initially evaluate the feasibility of measuring waves propagating through the viscoelastic medium consisting of soft tissues, a simplified model was constructed that eliminates as many environmental and biological factors as possible while maintaining similarity in dynamic response to a human structure. Gelatin's similarity to human skin in density, stiffness, and sound speed make it a common analog in physical experimentation (Dabrowska, 2015). In the current research, a homogeneous, isotropic gelatin is used to represent the soft tissue surrounding a femur, represented by a hollow aluminum bar. Specifics on the physical model, with respect to dimensions and how it was constructed, are provided in the next chapter. The chosen 250-bloom gelatin-water mixture consisting of 11.1% gelatin by weight has a speed of sound of about 1479 m/s and a Young's Modulus of approximately 17.8 kPa, as determined in other work (Farrer, 2015). These values are a good approximation of human soft tissue with an average wave speed of about 1540 m/s (Stern, 1983) and Young's Modulus (of muscle) in the range of 8-17kPa (Liu, 2015). The homogenous, isotropic structure allows the isolation of the effects that the nonlinear mechanical properties of soft tissue might have on acoustic waves propagating through it. Since the current study is an initial feasibility study, the use of this simplified soft tissue analog structure was considered as the best initial approach to investigating the ability of measuring the acoustic signal generated by vibrating bone structures on the skin's surface and inferring information about the exciting force. The next section shows how the acoustic measurement of body sounds on the skin's surface has been applied previously to analysis of *in vivo* biological systems.

2.6 Acoustic Measurement of Body Sounds

The acoustic measurement of body-sounds has increasingly been used as a non-invasive means to assess a few conditions of human biological systems. Various methods of measuring respiratory acoustic signals have been developed using digital stethoscopes (Miwa, 2009) and electret microphones (Wodicka, 1994). When measuring respiratory acoustic signals using electret microphones, the introduction of an air gap between the skin and microphone membrane was investigated as a means of improving sensitivity (Wodicka, 1994). A subsequent study investigated air cavity design parameters when measuring respiratory acoustic signals with electret microphones, focusing on air cavity shape, depth, width, and the presence of venting (Kraman, 1995). In that study, it was determined that the most effective cavity should be conical in shape, have a depth less than 5mm, and a diameter between 10 and 15 mm with no ventilation. These studies jointly determined that an increase in sensitivity of up to 10 dB could be achieved at frequencies below 500 Hz by using a cavity (Wodicka, 1994 and Kraman, 1995). As a result, the use of a cavity, the design of which is detailed in Section 3.2.3, was considered in the current research. However, an air cavity was ultimately not used in the final measurement method used to determine feasibility.

With respect to biomechanical loading, the sounds in knee joints have been investigated as methods to non-invasively determine knee health. In one such study, joint-sound-features were successfully detected in ambulatory subjects, even in uncontrolled settings, using microelectromechanical system (MEMS) microphones (Toreyin, 2016). MEMS and electret microphones are preferred to contact-based piezoelectric microphones due to the latter's associated sensor-skin interface noise that may compromise measurements taken at the skin's

surface (Teague, 2016). The current research does not utilize contact-based microphones in order to avoid issues related to sensor-skin interface noise. The electret model used in the current work (PUI Audio POW-1644L-LWC50-B-R) was chosen over similar-performance MEMS models due to being waterproof, which gives longevity when working with the ballistics gel in the current work, and low cost.

2.7 Background Summary

This chapter provided the relevant background for the current work. The motivation for the current work arises from limitations with respect to the conventional inverse dynamic method, which employs a link-segment model to determine internal bone forces from captured GRF and joint kinematic data. Such limitations include the need for a laboratory environment to capture data, error due to measurement methods of anthropometric structures, and error propagation when calculating internal forces due to the iterative process inherent in the method. It has been shown that measurements of a bone structure's vibration and subsequent acoustic response might be used in a novel inverse method to determine the forces transferred between bones during mechanical motion. In order to determine the feasibility of a measurement technique used as part of such an inverse dynamic method, a physical model consisting of an aluminum bar cast in a ballistics gel, representative of a femur and its surrounding soft tissues, was developed. The model's construction is such that its geometry is based on a simplified, extruded cross-section of a human femur and the gelatin's mechanical properties are similar to those of human soft tissues. The model's resonant frequencies are primarily below 500 Hz, as in human femurs and other long bones. This physical model is used in the current work to determine the feasibility of using electret microphones on the surface of the skin to measure

acoustic waves that originate from the vibration of internal bone structures during biomechanical motion. The next chapter provides details of this study's experimental setup, which includes details of the human structure model used in testing.

CHAPTER 3. EXPERIMENTAL SETUP

The previous chapter outlined the motivation for the investigation of a new inverse method to determine forces transferred between bones during human biomechanical motion as well as how such an inverse method might utilize measurement of pressure waves on the surface of the skin. The effect that the viscoelastic material properties of soft tissues have on the pressure waves as they travel from their origin, a vibrating long bone, is unknown. Due to the complexity of biomechanical systems, the current work utilizes a physical model during testing in order to determine the feasibility of measuring acoustic waves on the skin's surface after propagating through the viscoelastic medium of human soft tissues. The current model assumes a homogeneous gelatin structure as an analog for human soft tissues. This approach allows for exclusion of any effects due to heterogeneity or anisotropy of the medium present in living subjects on the travelling pressure waves within the soft tissues for this initial study. This section outlines the details of the experimental setup used during testing of the physical model as well as preliminary tests conducted, including calibration processes, noise measurements, and validation tests.

3.1 Physical Model

This section shows the process of how the model's physical characteristics were determined. The first subsection shows how model dimensions were determined based on other works. The second subsection shows how the model was constructed through a molding process

The final subsection explains the boundary conditions for the system and how they were achieved.

3.1.1 Physical Model Dimensions

The analog model constructed in this study consists of a hollow 6061 T6 aluminum bar cast inside of a homogeneous ballistic gelatin representing a simplified, extruded cross-section of a human femur and its surrounding soft tissues. The model’s length and circumference are scaled estimates based on mean lengths and circumferences of 63 adult male excised femurs (Black, 1978). Table 1 shows mean femoral length and mid-shaft mean circumference as found by Black (1978) and the respective scaled model dimensions. As one can see, the model geometry ratio is close to that of a real femur. Figure 5 shows a longitudinal side view of the model with dimensions, including bar length, bar outer diameter, and gel length (converted to standard units). Appropriate model dimensions were chosen to be an 8” bar length for a 0.5” outer diameter bar. The gel length does not entirely encompass the length of the bar due to constrictions associated with establishing the system’s boundary conditions, ensuring the ability to easily excite the bar structure, and sensor placement, discussed later in this chapter.

Table 1. Femoral mean dimensions (Black, 1978) and model dimensions

	Length (L)	Circumference (C)	Ratio (C/L)
Femoral Dimension (mm)	464.5	85.1	0.1832
Model Dimension (mm)	203.2	39.9	0.1964

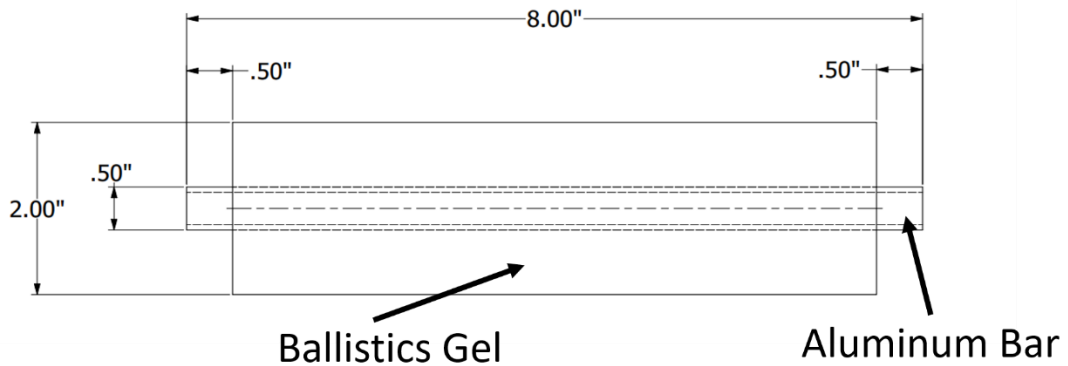


Figure 5. Model longitudinal cross section with associated dimensions

The model's respective bar and gel circumferential dimensions were determined by examining a chosen cross-section at the femur's midshaft from images produced by the Visible Human Project (Ackerman, 2019). The model's circumferential dimensions were estimated by taking the image's ratio of the femoral outer diameter and soft tissue outer diameter, found to be a factor of 0.19. Given a predetermined bar outer diameter of 0.5", a gel thickness of 2" was deemed appropriate. Figure 6 shows the location of the cross-section, A-A, located at mid-shaft of the femur, which was extruded in the simplified physical model. Figure 7 shows a cross-sectional view of section A-A with the labeled femoral outer diameter and the soft tissue outer diameter used to determine a reasonable gel thickness. Figure 8 shows a cross-sectional view of the physical model with corresponding dimensions in standard units.

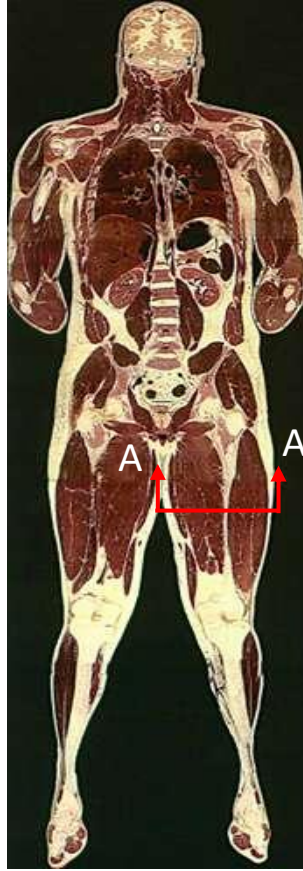


Figure 6. Visible Human Project cross-section A-A location (IMAIOS.com)

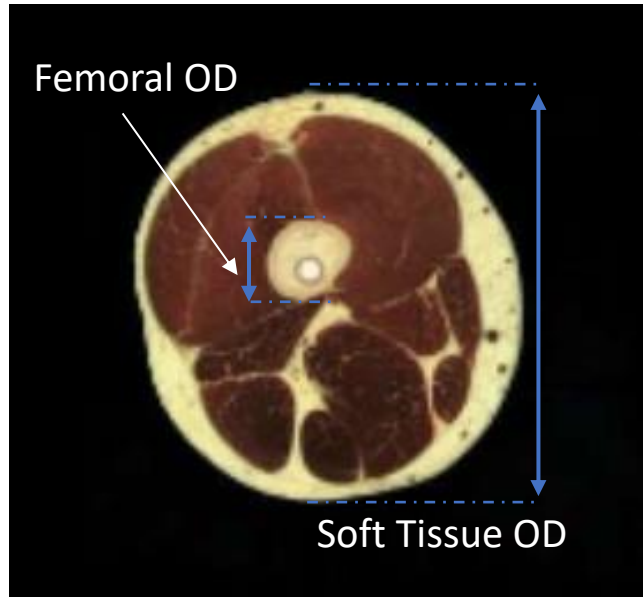


Figure 7. Visible Human cross-section A-A with labeled femoral and soft tissue outer diameters (IMAIOS.com)

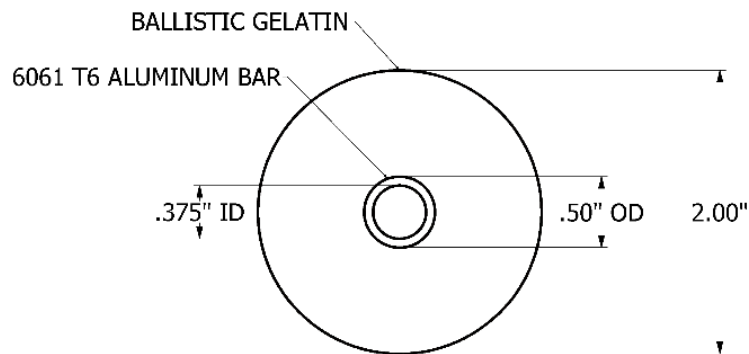


Figure 8. Physical model cross-sectional dimensions: Bar inner diameter (ID) and outer diameter (OD) and gel diameter

3.1.2 Physical Model Construction: Gelatin Mixing and Casting

The gelatin-water mixture used to represent the soft tissues surrounding the femur was cast around the aluminum bar described above. The casting process is detailed in Appendix A1.

After determining the dimensions of the model, as outlined in the previous section, a mold was 3D printed with ABS plastic, shown below in Figure 9. The mold was printed using a high density of material in order to make it watertight for the molding process.



Figure 9. 3D Printed mold used to construct experimental model

The gelatin-water mixture, in which the aluminum bar is cast, consists of 11.1%, 250-bloom gelatin by weight. Bloom is a measure of gelatin's strength once it solidifies. A higher Bloom value will lead to a greater strength and stiffness (Usta, 2003). The 250-bloom gelatin used in this study is considered a high Bloom value.

3.1.3 Physical Model Boundary Conditions

The physical model was set up such that the system boundary conditions were free-free. This setup was chosen for repeatability and its ability to eliminate the presence of stiffness that would otherwise be contributed to the ends of the system from clamping. The physical model

was suspended from a ceiling fixture by a small carabiner and a lightweight test line (SpiderWire EZ Braid, 30lb Test, 0.30mm Dia.), which was passed through the center of the aluminum bar. The suspended experimental model is shown in Figure 10 with the aluminum bar, ballistics gel, and test line labeled that are the base of the experimental setup for the measurements later described in Sections 3.2.2 and 3.2.3.

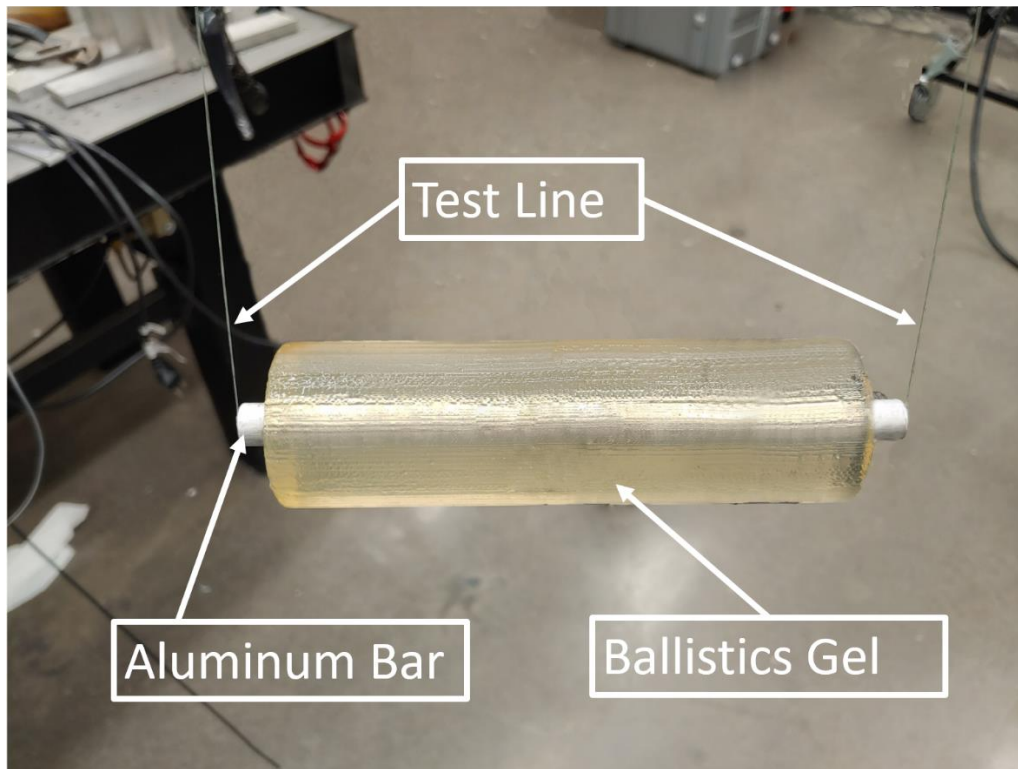


Figure 10. Experimental model suspended with test line

3.2 Testing Configurations and Instrumentation

This section shows sensor configurations and instrumentation for the various tests conducted. The first subsection shows the drive circuit for the electret microphones (POW-1644L-LWC50-B-R) utilized throughout the experiment as well as how the electret microphones were calibrated. Later subsections show the configurations for a test that focuses on

consideration of utilizing a device to create an air chamber between the electret microphone's diaphragm and the gel surface and the final configuration ultimately decided upon that would best determine the new measurement technique's feasibility. In all configurations, the impulse force hammer used was a Kistler Type 9722A2000 and the accelerometers are PCB Piezotronics Model 352C22. The Data Acquisition System (DAQ) used for all data collection was a Brüel & Kjær (BK) Type 3677-A-041. BK Connect™ was used to apply windowing, perform the Fast Fourier Transform (FFT), and determine the FRF functions while MATLAB® was used for other post-processing work, with the associated code given in the Appendix.

3.2.1 Electret Microphone Drive Circuit and Calibration

The electret microphones used throughout testing were powered by the circuit shown in Figure 11. The power supply for the circuit was an Agilent E3630A. The chosen capacitor value of 1 μ F resulted in a high-pass, first-order analog filter with cutoff frequency of about 72 Hz. It is important to reiterate that this filter is only of the first order and will therefore not greatly attenuate components of the measured signal just below the cutoff frequency. Since the absolute accuracy of the magnitude of the signal measured is not currently of great interest, but rather the relative values of the magnitude measured, frequencies attenuated near the cutoff frequency are still considered relevant later in the analysis of the measured quantities.

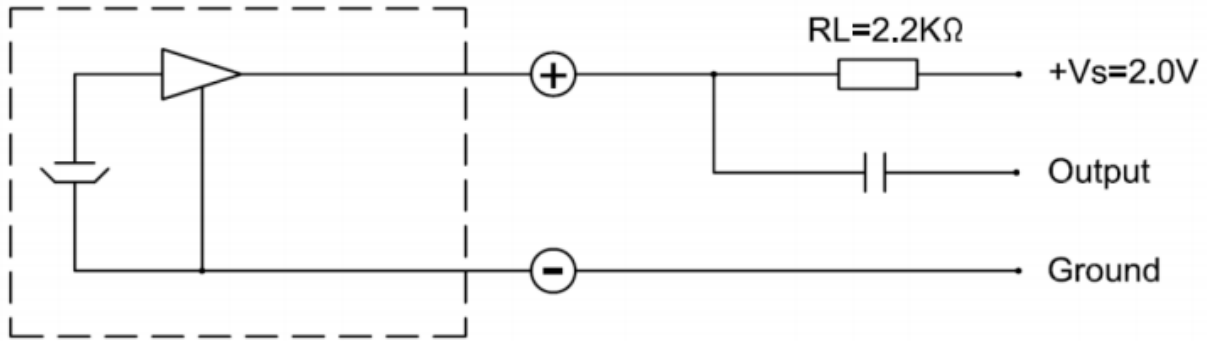


Figure 11. Electret microphone drive circuit repeated from its datasheet (Mouser, 2015)

The electret microphones were calibrated by placing them symmetrically (relative to a loudspeaker's diaphragm center) at a distance of 6 inches from a loudspeaker's driver (Sound Ordnance "Soundstream" BB8-35S) and generating a swept sinusoid signal through frequencies ranging from 50-1600 Hz. The setup used for calibration can be seen in Figure 12.

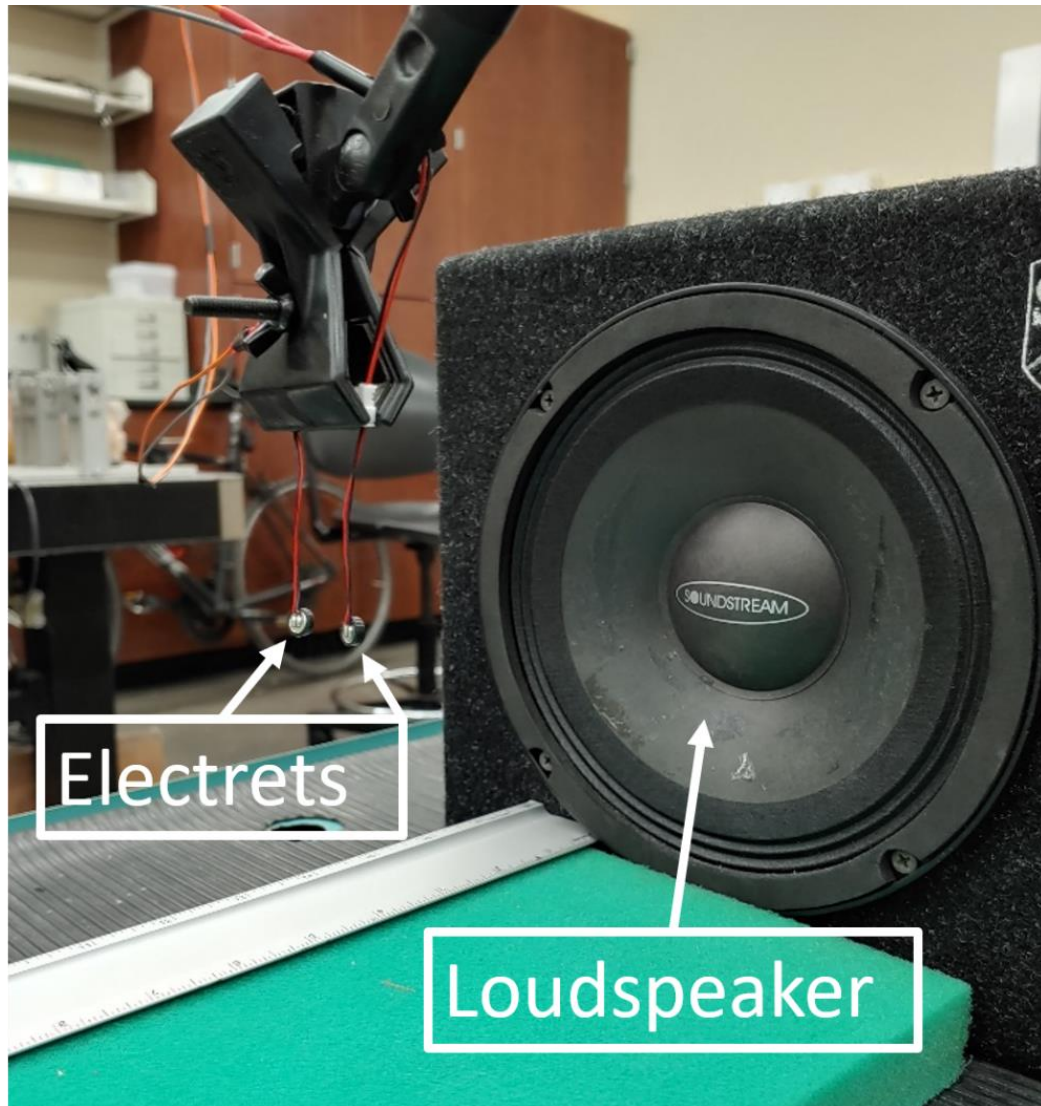


Figure 12. Electret calibration setup utilizing a loudspeaker

The microphones were calibrated such that one was considered nominal and the other's sensitivity was adjusted to closely match the nominal microphone's frequency response for the swept sinusoid. Figure 13 shows the resulting frequency response of the electret microphones used in testing after the calibration process was completed. Related Figure 14 shows the FRF between the two microphones, where Electret 1 was chosen as the reference sensor with nominal sensitivity. These figures show that the microphones agree with one another with a maximum

difference in magnitude of 6.2% and a maximum phase difference of 2.57 degrees for signals measured between 50 and 1200 Hz. This 50-1200 Hz bandwidth is considered the acceptable measurement range during this study. The microphones' agreement improves between 50 and 500 Hz, the primary range under consideration in this study due to the model's resonant frequencies within this range. Within this 50 to 500 Hz band, the microphones have a maximum difference in magnitude of 1.61% and are up to 1.31 degrees out of phase.

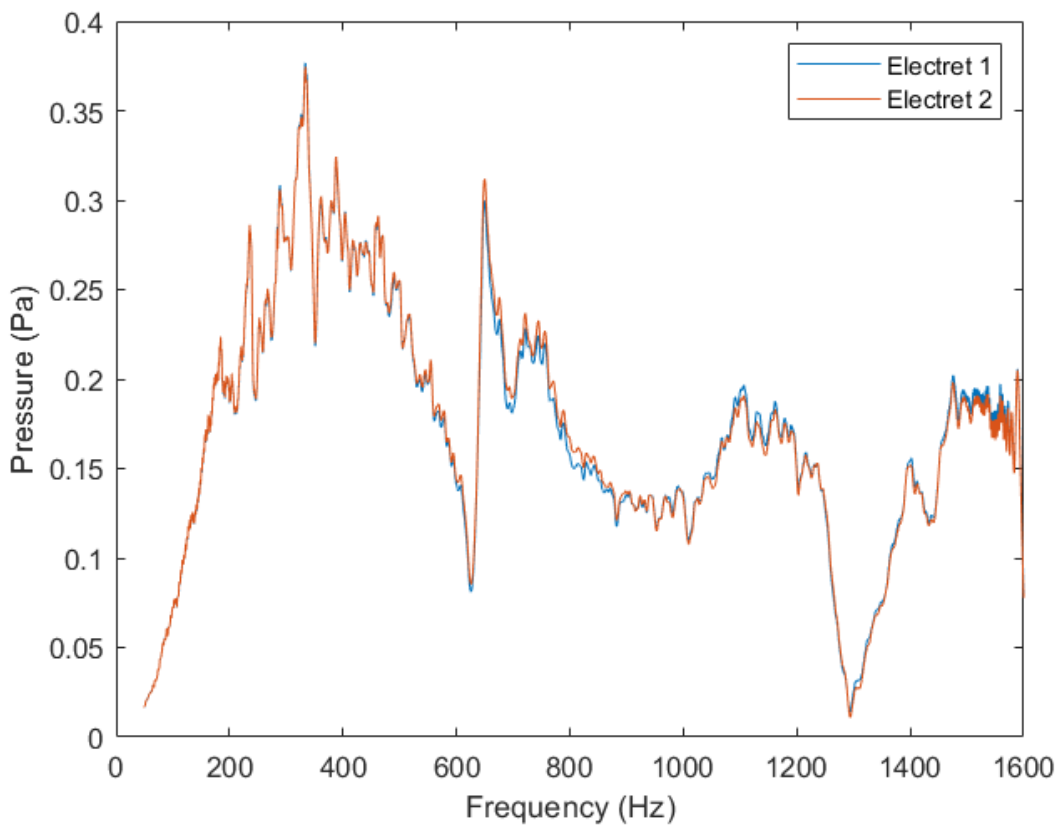


Figure 13. Autospectra of electret microphones during calibration

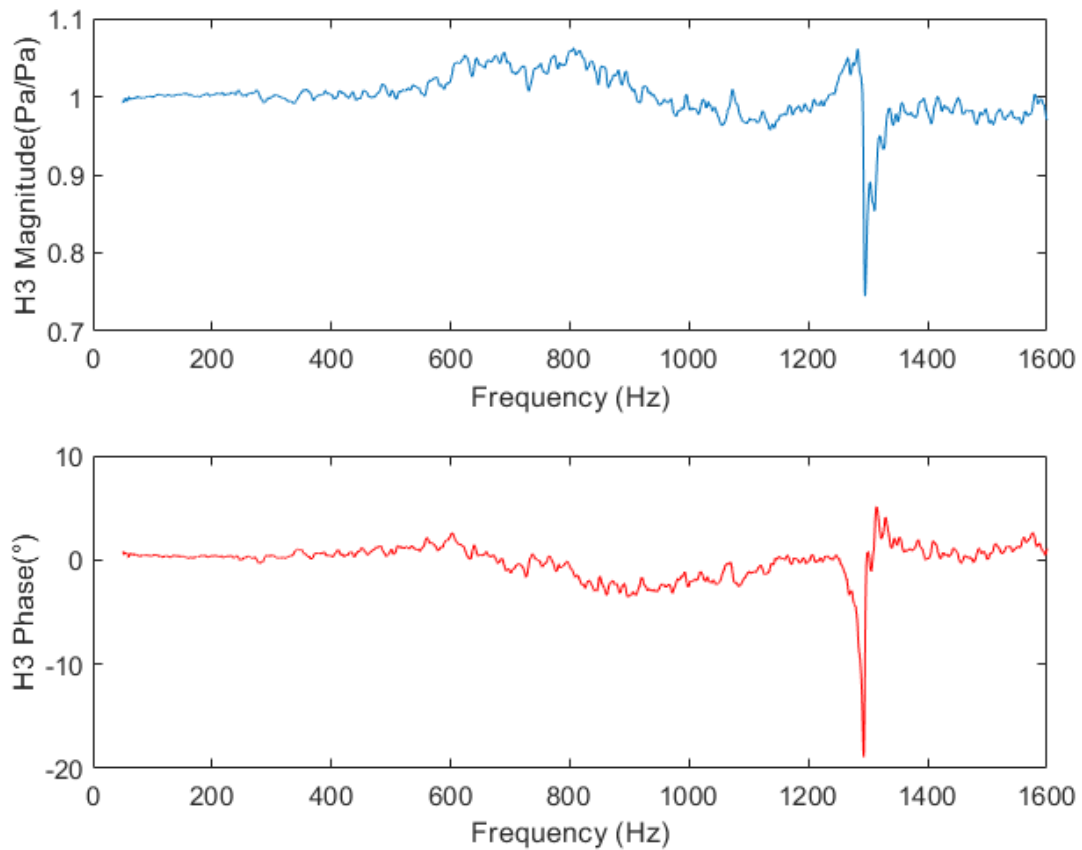


Figure 14. Electret calibration curves and FRF (H3) for electret microphones

3.2.2 Noise Threshold Measurements

Before presenting measurement data, it is necessary to show the level of noise present in measurements due to ambient and electrical noise. Noise level measurements were performed by setting up the microphones in the configuration described in Section 3.2.3 and manually triggering data collection with no excitation. Data was captured in the lab environment with no extraneous background noise for a period of 500 ms, matching the period of data collection during testing. Figure 15 and Figure 16 show a typical sample of the Sound Pressure Level (SPL) of ambient and electrical noise present in the lab and circuitry measured by each sensor for

frequencies up to 1600 Hz and 500 Hz, respectively. The SPL in dB was found according to the relation

$$SPL (dB) = 20 \log_{10} \left(\frac{P}{P_{ref}} \right), \quad (11)$$

where, P is the electret's measured pressure in Pascals (Pa) and P_{ref} is the reference pressure level of $20 \mu\text{Pa}$, the standard reference pressure representative of the lowest pressure typically registered in human hearing. Note that since the electret microphones were not calibrated to measure the absolute pressure level but were instead relatively calibrated as previously described in Section 3.2.1, the SPL shown in figures here is used for reference only and not indicative of absolute SPL.

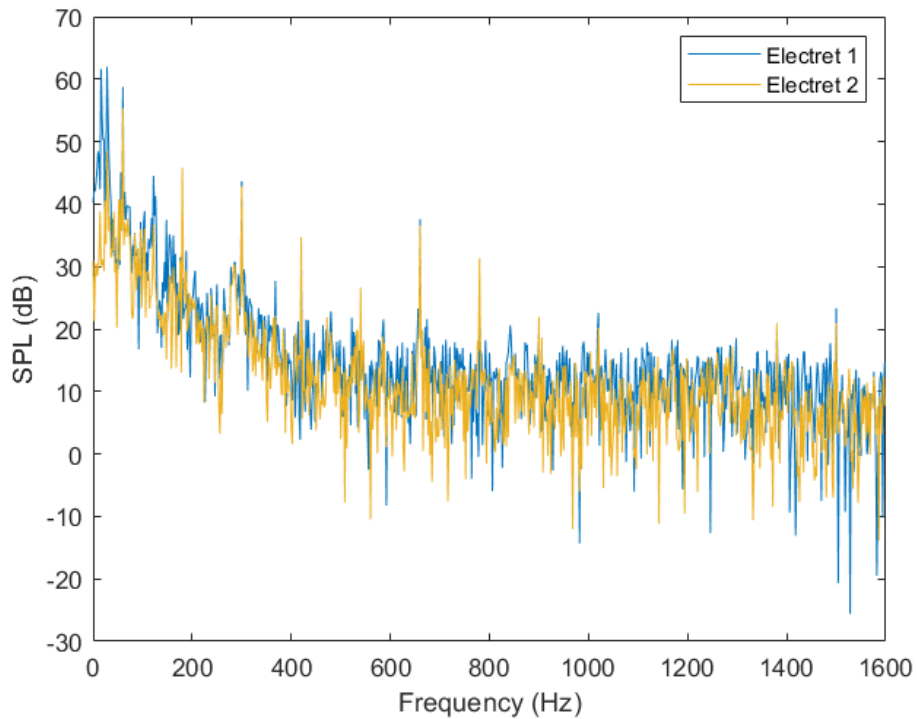


Figure 15. Ambient and electrical noise up to 1600 Hz

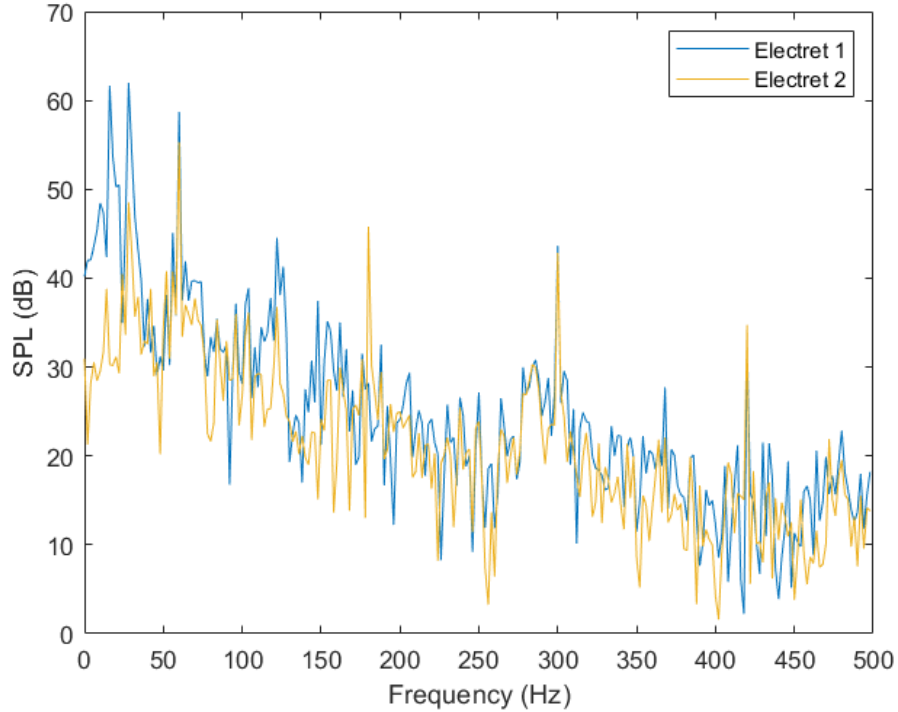


Figure 16. Ambient and electrical noise up to 500 Hz

Figure 15 and Figure 16 show that the maximum noise present in this sample due to electrical noise is about 58 dB at the fundamental frequency of Alternating Current (AC) power, 60 Hz. Other peaks at harmonic frequencies to the fundamental electrical noise frequency are also present, but at smaller amplitudes (e.g. 44 dB at 120Hz). With the exception of peaks due to electrical noise, the ambient noise within the laboratory environment in which samples were taken is below 40 dB for signals between 50 Hz and 200 Hz and below 20 dB for signals above 250 Hz. By comparing noise measurements shown in Figure 16 with data collected during testing shown later in Figure 21, it is seen that the signal levels of measurements are above noise levels at all frequencies within the 1600 Hz measurement range (except for 60Hz) by at least 30 dB. For this reason, noise filters were not applied since the measured signals are at significant enough levels above the noise threshold to be meaningfully affected. By not applying

unnecessary filters, useful signal elements present near the harmonic frequencies of electrical noise are not removed. Signals affected by the largest magnitude electrical noise at 60 Hz were not considered in analysis since this frequency was not found to be a resonant frequency of the physical model.

3.2.3 Air Gap Device Efficacy

The integration of an air-gap device into the measurement method in the current work was investigated. As previously mentioned in Section 2.6, it has been shown that the usage of such a device can effectively increase a surface microphone's sensitivity when used to measure lung sounds on the skin's surface (Kraman, 1995 and Wodicka, 1994). Thus, this study considered the usage of such a device for the measurement of the waves that propagate to the skin's surface during biomechanical excitation. The air gap device utilized in this study was 3D printed with ABS plastic, had no ventilation, and was conical in shape with an air gap of 0.25" between the skin's surface and the microphone's diaphragm. A detailed cross-sectional side-view is shown in Figure 17. The electret microphone was coupled to the air gap device through an interference fit with the microphone's outer rubber gasket covering. The air gap device was then coupled to the gel's surface by wrapping electrical tape over the flanges and around the gel's surface, providing tension in the tape and a relatively tight fit for the device.

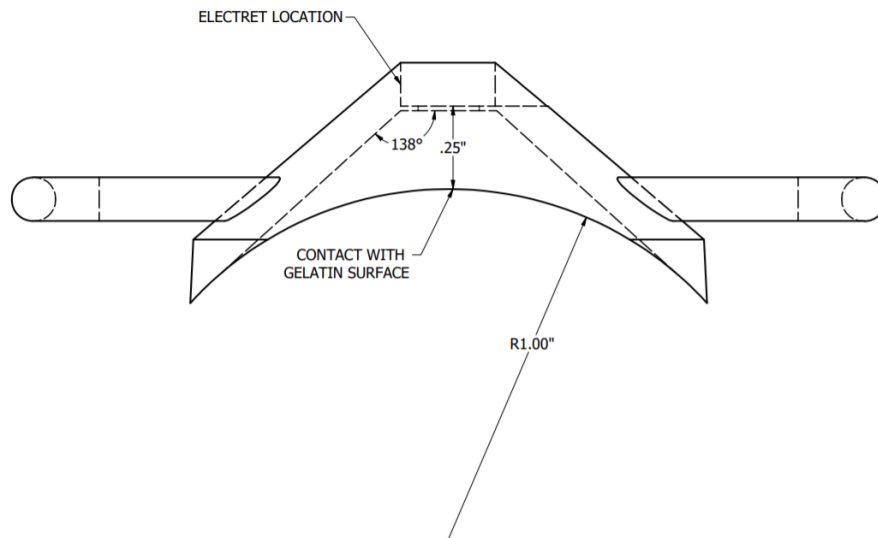


Figure 17. Air gap device cross-sectional view

This initial experiment to determine the efficacy of an air gap was conducted by exciting the aluminum bar with an axial impact and measuring the resulting time-domain signal for both the impact hammer and microphones. Then, frequency responses of the electret microphone utilizing the air gap device and the electret directly coupled to the gel's surface (not utilizing an air gap device) were compared. The microphones were placed at the same axial location along the bar on the gel's surface, but on opposite sides of the structure. An accelerometer (PCB 352C22) was also placed on the bar's surface on the opposite end of the impact for comparison between the bar's measured vibrations and the measured signal on the gel's surface after the generated pressure waves propagated through the gel. Note that this accelerometer was used to obtain information on the transverse vibrations of the bar for this study and would not be used in an actual implementation of the proposed approach. Figure 18 shows a drawing of this experimental setup with electret locations labeled and Figure 19 is a photo of this experimental setup.

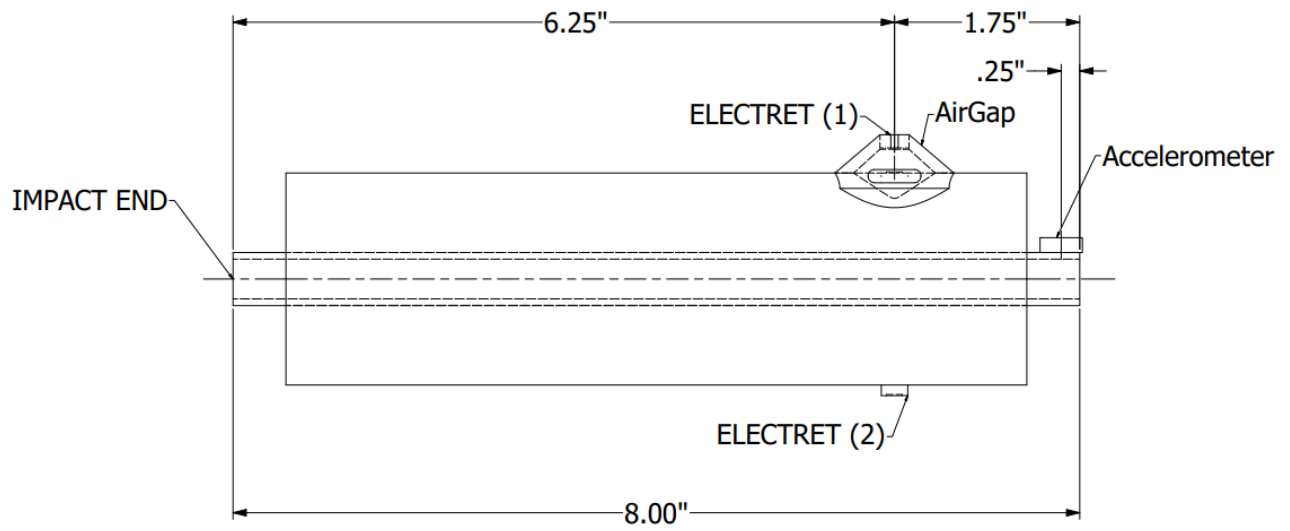


Figure 18. Drawing of air gap efficacy experimental setup

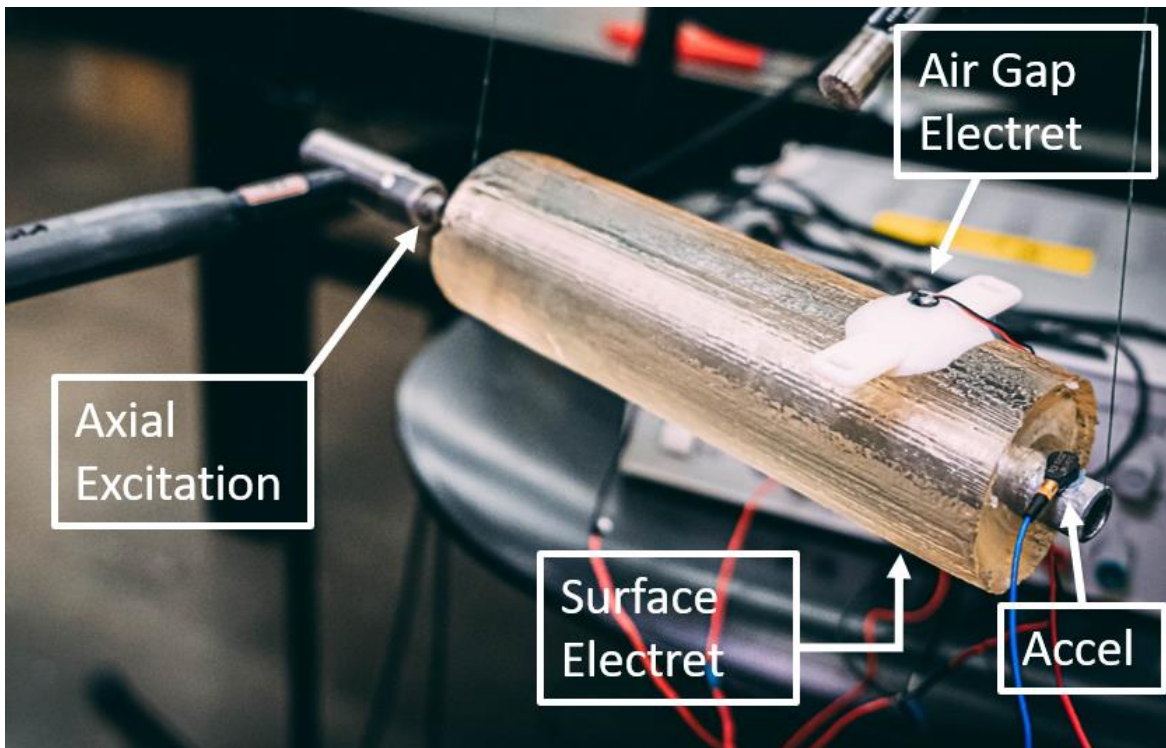


Figure 19. Experimental setup to determine an air gap cavity's effect on measurements

Figure 20 through Figure 23 are useful in comparing the performance of the electret microphone that utilizes an air gap with that of the microphone in direct contact with the gelatin's surface. Figure 20 shows the frequency response for all of the sensors used, plotted on a linear scale. From Figure 20 it is apparent that both electret microphones measure similar signals below 200 Hz with respect to the frequencies present, though the microphone that utilizes the air gap measures signals an order of magnitude higher than the electret coupled directly to the surface. While the resonant frequencies of the system are apparent, they are heavily damped, as indicated by the broad peaks associated with each. Figure 21 and Figure 22 show the frequency response of the electret microphones, plotted on a logarithmic (dB) scale, superimposed with the accelerometer's measured vibration response for frequencies below 1200 Hz and 500 Hz, respectively. These two figures show that while the air gap does in fact significantly increase the microphone's sensitivity by about 20 dB for signals below 200 Hz, the air gap electret does not seem to measure a meaningful signal at frequencies above 200 Hz. When compared to a sample of ambient noise shown in Figure 15 and Figure 16, it is apparent that the electret placed directly on the gel's surface is measuring at a sufficient level above the noise threshold (by at least 30 dB) such that the increased sensitivity from using the air gap device is not necessary.

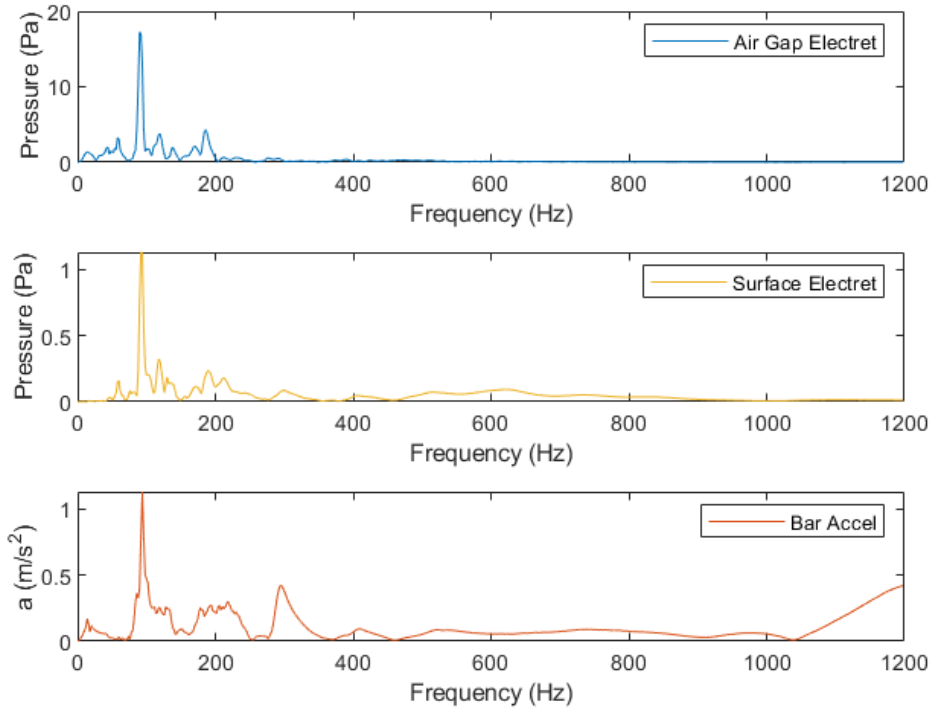


Figure 20. Frequency response (linear) of both electrets and accelerometer below 1200 Hz.

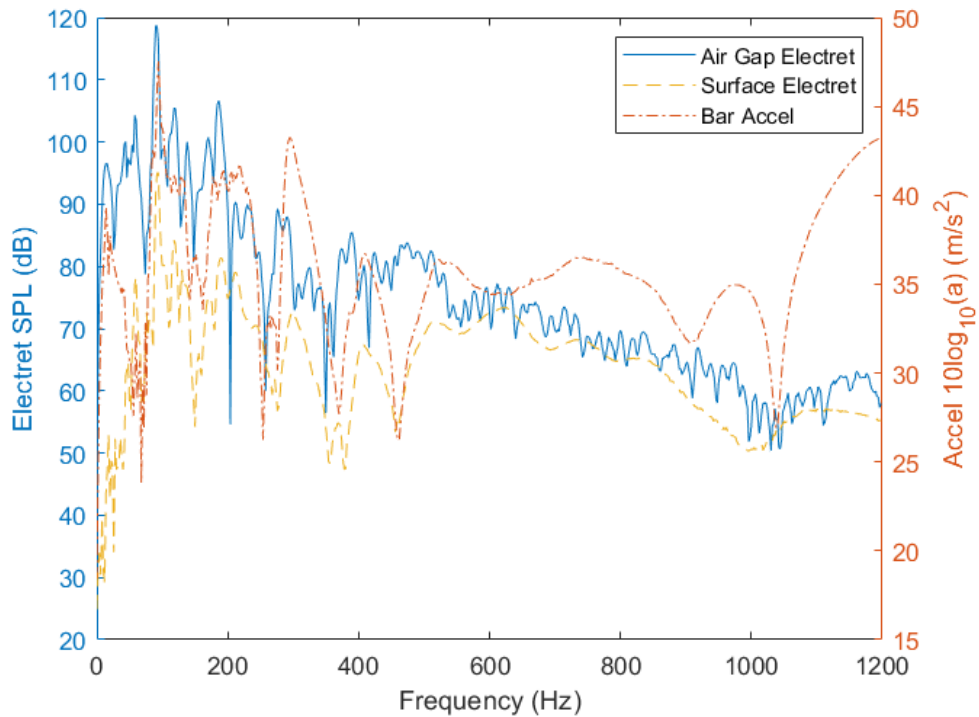


Figure 21. Frequency response (dB) below 1200 Hz for all sensors

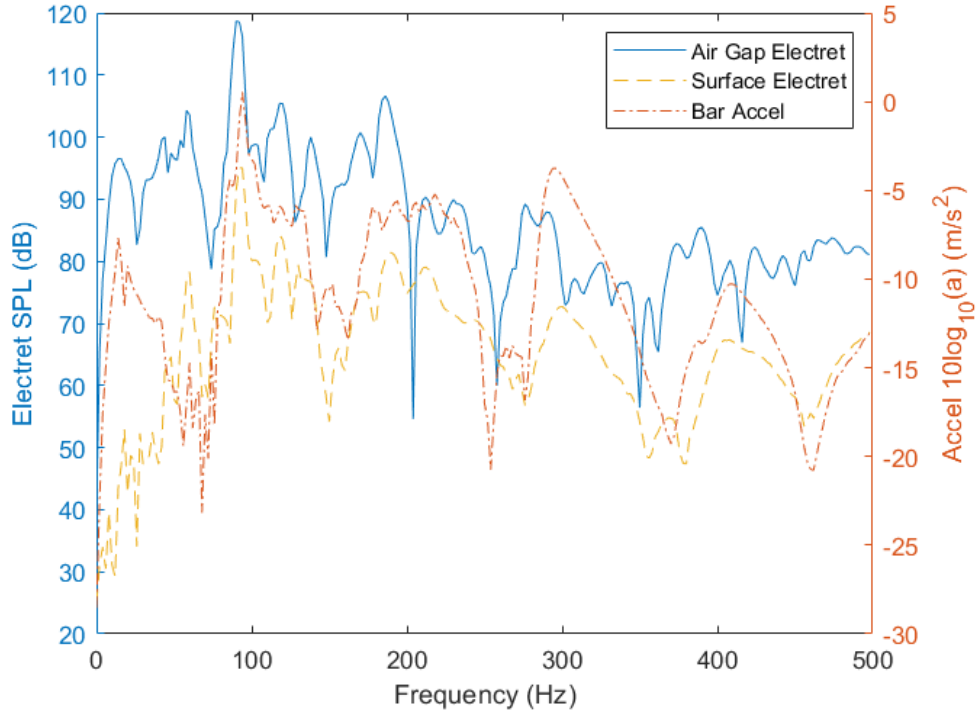


Figure 22. Frequency response (dB) below 500 Hz for all sensors

While the electrets' frequency responses are expected to slightly differ from the accelerometer's, due to the accelerometer's inability to measure axial modes in its current configuration, the frequency responses of the electrets are expected to be more similar to each other since the directly-coupled surface electret is measuring a signal significantly above the noise threshold. The anomalous frequency content is apparent in Figure 22, where the frequency response for each sensor is superimposed. While the origin of these anomalous frequencies is unknown, it is hypothesized that they may be due to contact noise between the air gap device and the gel's surface. Figure 23 shows the normalized curves for each sensor with respect to their maximum measured amplitude and highlights how the spectral energy density is distributed for each sensor's measured signal for a sample axial impact test.

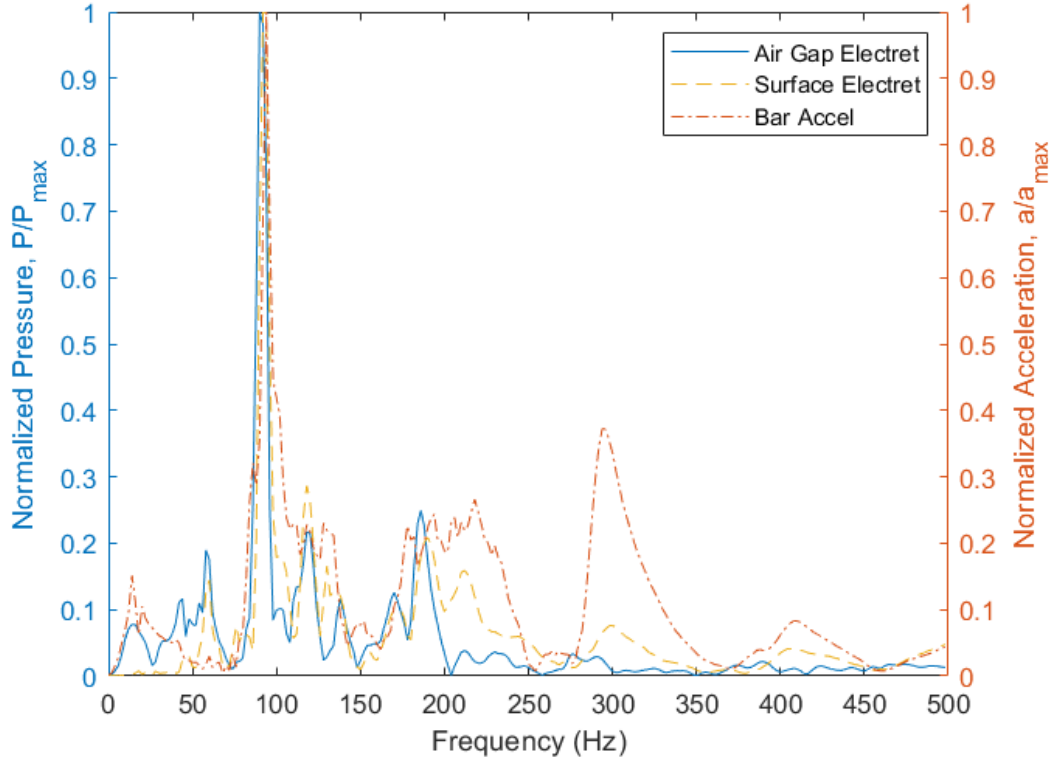


Figure 23. Normalized frequency response below 500 Hz for all sensors

Figure 23 shows that when compared to the accelerometer’s frequency response, the energy is more similarly distributed for the directly coupled surface electret than the one that utilizes the air gap device. Given all these factors, it was decided that the final experimental setup used in this study would not utilize an air gap adapter as a part of the measurement technique considered, and instead the electret microphone would be mounted to the gelatin’s surface directly.

3.2.4 Feasibility Study Setup

The feasibility study at the center of this research aims to correlate the magnitude of the impact delivered by an instrumented hammer to the model’s internal aluminum bar with acoustic

measurement data from electret microphones on the model's gel surface. The experimental model previously described, consisting of an aluminum bar and ballistics gel, was suspended to establish free-free boundary conditions during impact testing. The two electret microphones on the gel's surface measured the acoustic waves propagating through the gel and an accelerometer mounted to the bar's surface measured the vibratory response of the internal bar structure, which was used only for reference purposes. Figure 24 shows the location where each of these three sensors was placed on the experimental model and Figure 25 is an image of the experimental setup with system component labels.

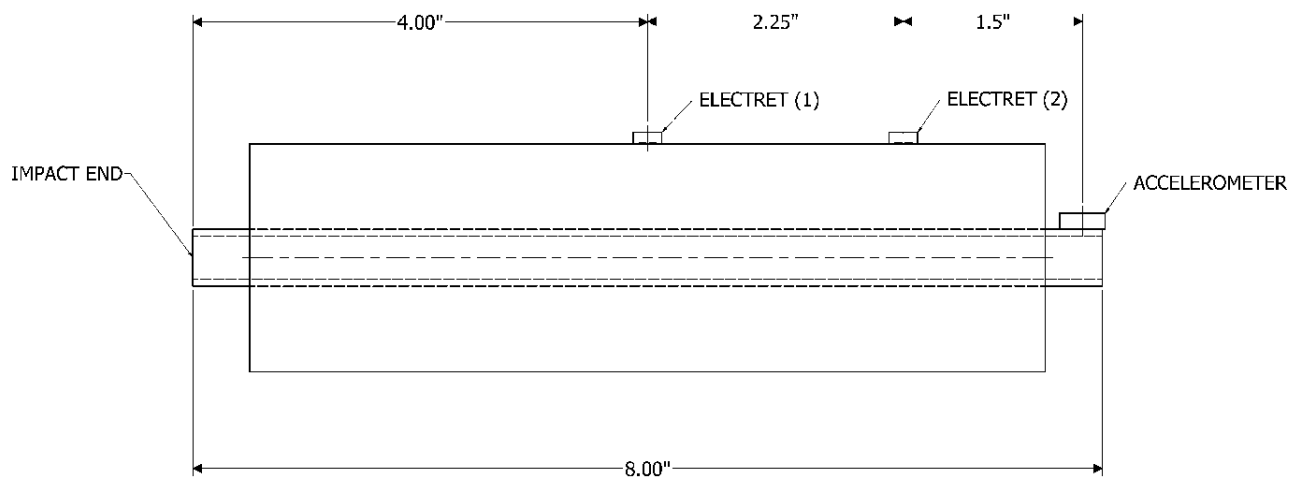


Figure 24. Sensor dimensional locations for analog experimental setup

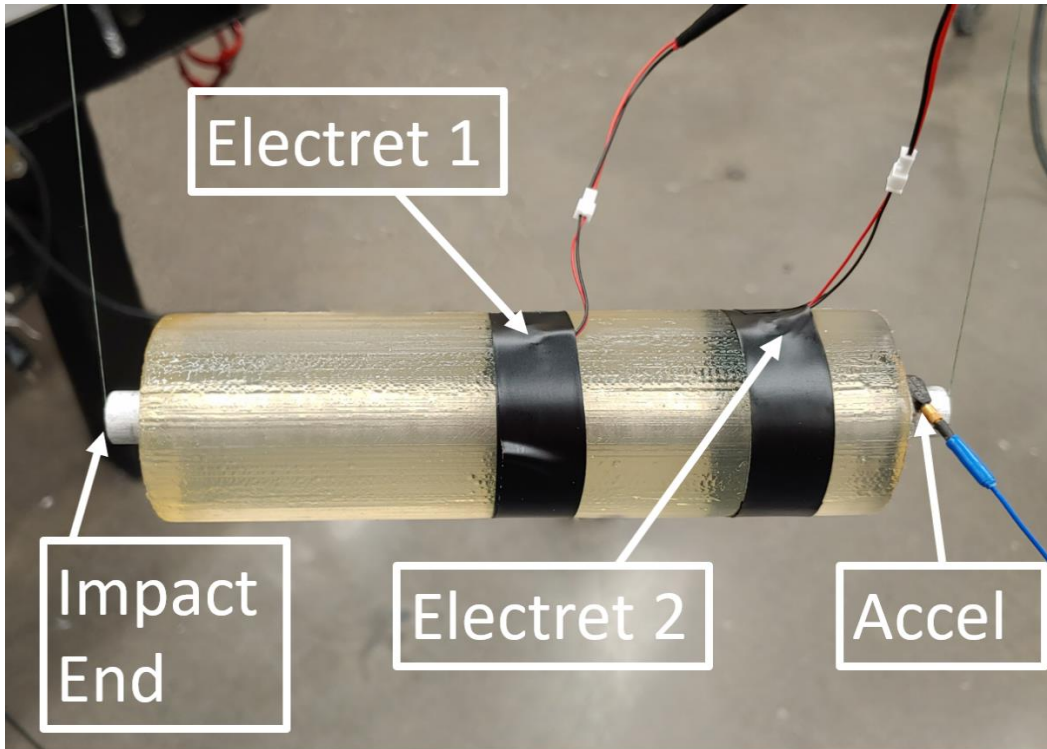


Figure 25. Feasibility study setup with electrets and accelerometer labeled

Placement location of the electret microphones was chosen based on the first 6 mode shapes of the aluminum bar as determined by FE modelling in Solidworks, illustrated in Figure 26. Note that the first six modes shown in Figure 26 are rigid body modes and not representative of the bar's modal response, so the illustrated modes begin with the seventh mode. Also, the frequencies for each mode shape are only representative of the bar's response without the presence of the gel surrounding it. These modal frequencies are lowered after adding the gel due to effects from the added mass and damping.

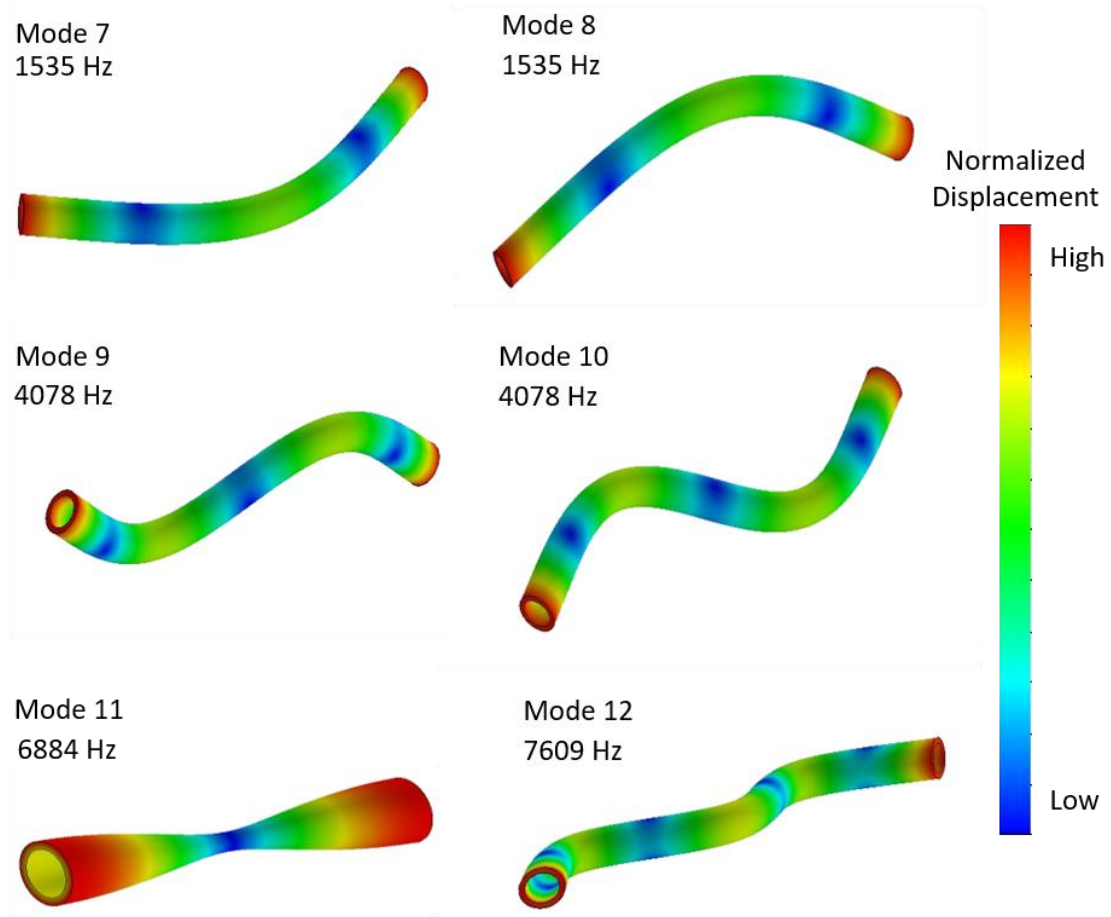


Figure 26. Solidworks modal analysis: first 6 modal shapes frequencies of aluminum bar

Again, the frequencies for the aluminum bar are shown here for reference purposes only in order to show the relative frequencies at which the modes might still occur after adding the gel. Some higher order modes may be present in the bar-gel model, but lower modes are typically more prominent in a dynamic system's frequency response (Meirovitch, 1975). Higher frequency modes will likely be unmeasurable due to the system's high damping. Electret 1 was placed at the axial center of the bar and Electret 2 was placed at a separate axial position on the same side of the bar 1.5" from the bar's end, as previously shown in Figure 24. Electret 1's position corresponds to a node present in the 2nd and 4th bending modes, while Electret 2 was

placed at a position that does not correspond to any of the first few bending modes' associated nodal locations. Although the sensors were not actually located at the nodal locations due to the presence of the gel and the resulting wave propagation, this layout allowed for comparison between the frequency response captured by each microphone based on its position on the gel's surface and allows for inference as to which modes are present in each electret microphone's signal, based on those measured by the accelerometer on the bar's surface.

Data was collected for impact testing in three different configurations. In each configuration, either an axial or transverse impact was applied to the internal bar's end with an impulse force hammer. Figure 27 shows these three configurations with the corresponding orientation of the axial and transverse impacts labeled along with the respective sensor array. The transverse impacts were applied to the structure based on their relative position to the sensor array, such that they were either in-plane (IP) or orthogonally out-of-plane (OOP).

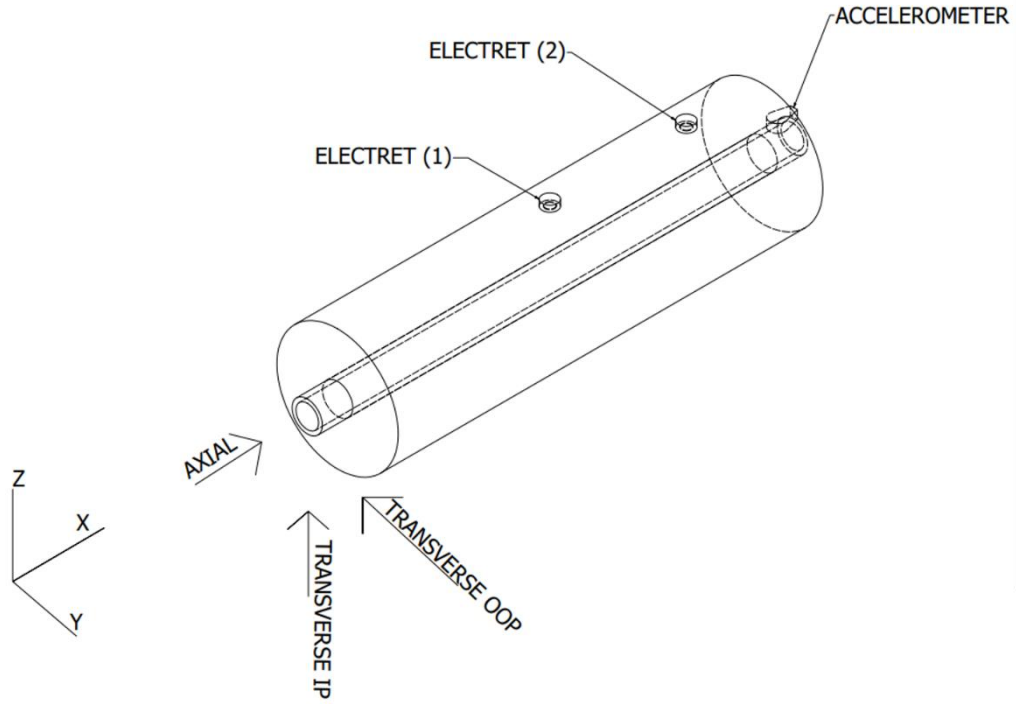


Figure 27. Impact orientation for axial, IP transverse, and OOP transverse impacts and relative sensor array placement

In each configuration, data was sampled at 65,536 samples per second for 500ms. Due to the signal's transient nature, a Rectangular Window was applied before performing FFT analysis within the BK Connect software. This time window and sampling rate correspond to a measured bandwidth of 25.6 kHz with a 2 Hz resolution for the spectral data. The frequencies of interest largely lie below 500 Hz, but it was necessary to sample at a higher rate in order to capture the peak of the hammer's impulse as accurately as possible, as that peak force level is used in analysis of feasibility. Finally, test conditions are described in Appendix A1, including details on ambient temperature and how the test sample was monitored to ensure it maintained a constant internal temperature so as not to have variance in its mechanical properties during testing.

3.3 Experimental Setup Summary

This section presented the experimental setup used to determine the feasibility of the novel measurement technique under consideration: a technique in which a microphone array is placed on the skin's surface to measure acoustic waves which have propagated through soft tissue, originally generated by a vibrating bone structure during biomechanical motion. The physical model tested was a simplified representation of a femur's extruded cross-section, where an aluminum bar was used to represent the femur and a homogeneous ballistics gel was used to represent the surrounding soft tissues.

Two tests were conducted, the first of which considered the efficacy of utilizing an air gap adapter as a part of the measurement technique, and the second of which was the feasibility study which is the focus of this research. In each of the two tests, the physical model was excited by an instrumented hammer, representative of bone-on-bone forces transferred through joints during biomechanical motion, while the electret microphones were placed in an array on the gel's surface. An accelerometer was placed directly on the aluminum bar's surface for reference.

An air gap adapter's usage was considered as a part of the measurement technique due to its demonstrated ability to effectively increase microphone sensitivity at lower frequencies when measuring body sounds. While the inclusion of the air gap device was confirmed to increase microphone sensitivity at lower frequencies ($f \leq 200\text{Hz}$) for the current application, the ability to reliably measure signals at frequencies greater than 200 Hz was compromised when compared to the directly-coupled electret. Thus, an air gap adapter was not used in the final measurement technique used to determine the measurement technique's feasibility.

In order to determine the feasibility of the novel measurement technique, two electret microphones were coupled directly to the gel's surface at different axial locations with the same radial placement. The system was excited by the instrumented hammer in three configurations, consisting of an axial impact, a transverse impact with in-plane measurements, and a transverse impact with out-of-plane measurements. The feasibility of the measurement technique was decided based on analysis of the sensor measurements, discussed in the next section.

CHAPTER 4. EXPERIMENTAL RESULTS

The data collected from the experiments previously described in Section 3.2.4 were post-processed in order to determine the efficacy of utilizing surface microphones to measure acoustic waves on the skin's surface. Since the ultimate goal of this study is to determine if electret microphones are able to measure acoustic signals which have propagated through soft tissue as a means of inferring information about bone forces, the focus of post-processing was on establishing the level of correlation between the electrets' measured signals and the quantitative characteristics of the impact for each configuration.

The electret signals were analyzed by developing least squares regression models to correlate acoustic signal characteristics in the frequency domain and the hammer's force characteristics in the time domain. For all models, the y-intercept was forced to zero. Two quantities were chosen in both the electrets' frequency domain and the hammer's time domain, for a total of four regression models. In the frequency domain, the chosen characteristics were the autospectral magnitude of the electret microphones' acoustic signal at targeted frequencies as well as the energy present in a few selected frequency bands. These frequency domain characteristics were correlated to the impact's peak force value in the time-domain as well as the impulse of the first impact, which is described in detail below.

In the first regression frequency domain method, frequencies that showed a prominent response in the autospectrum of the surface microphones were targeted. The chosen peaks in the frequency response of the electrets likely occur at resonant frequencies of the bar-gel structure

and are expected to increase with higher magnitude impact forces. It is important to note that, since the input signal is not known *a-priori* in an actual application of the proposed approach, the FRF will not be utilized in the analysis presented here. Rather, the cross-correlation between the magnitude response at each of these selected frequencies and the impact force peak value was used to examine the feasibility. In the second frequency domain method, the total energy in selected frequency bands was similarly examined for a correlation to the hammer's time-domain characteristics. The bands were selected based on key transition points determined in the electrets' autospectra.

Sample results for the electrets and accelerometer (reference only) are shown below for each setup along with a discussion of any correlation provided at the end of each section. The results of the axial impact trials in Section 4.1 are more detailed than those for the transverse impact trials in subsequent sections, allowing for a clear representation of the post-processing methods and brevity where the same methods were applied in later tests. The code utilized to post-process the measured data in MATLAB and subsequently generate the plots is provided in Appendix A4.

4.1 Axial Impact Results

The first test examined a possible correlation between some features of the acoustic signal measured at the surface of the gel and the impact for a force that is applied axially to the bar (see Figure 27). Figure 28 and Figure 29 show sample plots of time data collected from three different axial impacts for the hammer and Electret 1, respectively. As shown in Figure 28, each impact results in a series of force peaks that occur at near constant intervals and that decrease in amplitude with each appearance. This is expected during experimentation as impacts must

realistically occur for a non-zero amount of time and the hammer will usually strike the system multiple times due to rebound. The first peak for each impact occurs within a 0.2 ms timespan, and the remaining impacts occur at intervals of about 2 ms, corresponding to fundamental frequencies of about 5000 Hz and 500 Hz, respectively. Both of these frequencies are above the frequency range that is primarily analyzed, as discussed later in this section, indicating that the frequency content below 500 Hz present in the measured output signal is not an artifact of the impact nature. Furthermore, frequencies above 500 Hz were shown to be heavily attenuated during preliminary trials when determining the efficacy of an air gap device, as previously discussed in Section 3.2.3, and are therefore unlikely to be measurable by the electret microphones. The first and most prominent peak in Figure 28, labeled for each sample signal, corresponds to the first time-domain quantity examined as a parameter in the regression models that follow. Labeled times t_0 and t_1 in Figure 28 are the parameters that define the impulse associated with the first peak, henceforth referred to as the primary impulse, which is the second time-domain quantity examined in the regression models. An impulse is defined as the integration of a force over time,

$$J = \int_{t_0}^{t_1} F dt, \quad (12)$$

where J is the impulse and F is the applied force, which is a function of time (Dourmashkin, 2014). The integration limits of t_0 and t_1 correspond to the time in seconds of the beginning and end of the primary impulse, annotated in Figure 28. The difference between these values gives the value Δt .

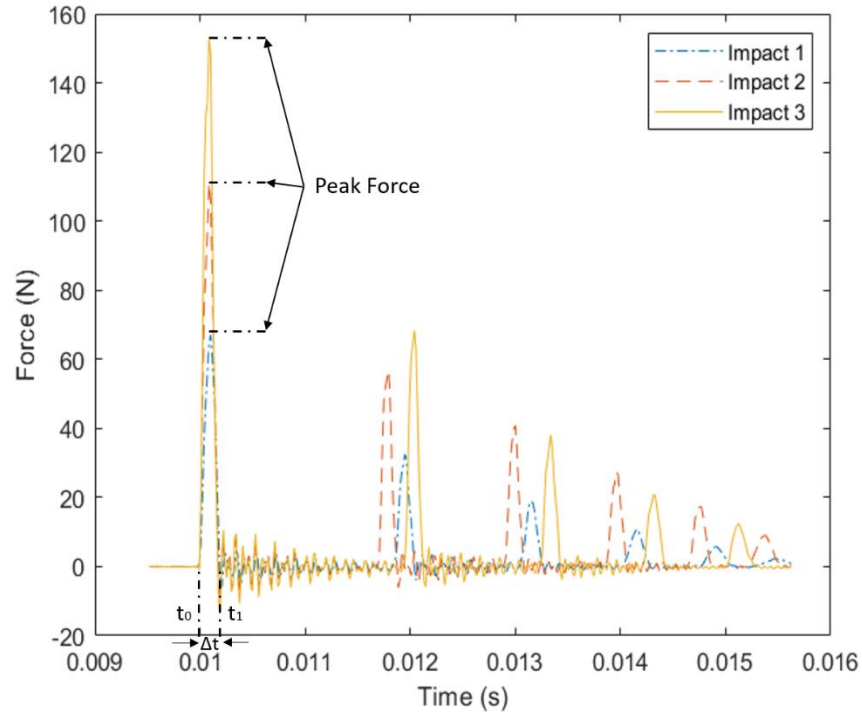


Figure 28. Sample time data of impact hammer for three axial impacts with labeled peaks and impulse times

Figure 29 shows the measured acoustic signal of Electret 1 (located near the center of the gel as previously shown in Figure 27) as a function of time. A transient response occurs within the first 0.02 s before the acoustic response settles to a typical free response. It is apparent from comparing Figure 28 and Figure 29 that a higher magnitude impact results in a larger magnitude measured response, as expected. The measured response, however, does not decay at a constant rate, and even experiences periods of increase before decreasing. This behavior seems to indicate that the gelatin is behaving as an acoustic chamber of sorts, reflecting signals off its flexible walls. The gelatin behaving as an acoustic chamber affects the measured frequencies, as discussed later in this section.

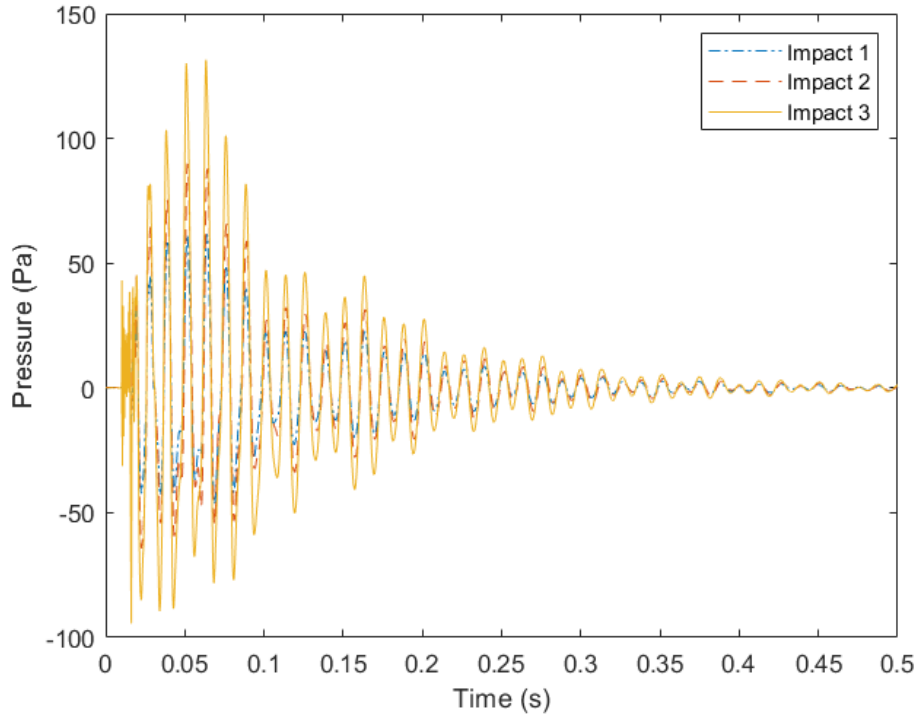


Figure 29. Sample time data of Electret 1 for three axial impacts

The autospectrum of the measured signals for each impact was determined by using the FFT function in BK Connect software after applying a rectangular window to the measured signals. A rectangular window was used since the signal naturally attenuated to a near-zero value by the end of the sampling period. Sample plots of the autospectrum for the same impacts shown in Figure 28 and Figure 29 are given in Figure 30 and Figure 31, where the autospectra of Electret 1 up to 1,200 Hz is plotted on linear and logarithmic (dB) scales, respectively. Again, the SPL of the electret microphones was computed here with respect to P_{ref} of $20 \mu\text{Pa}$ for consistency with earlier figures.

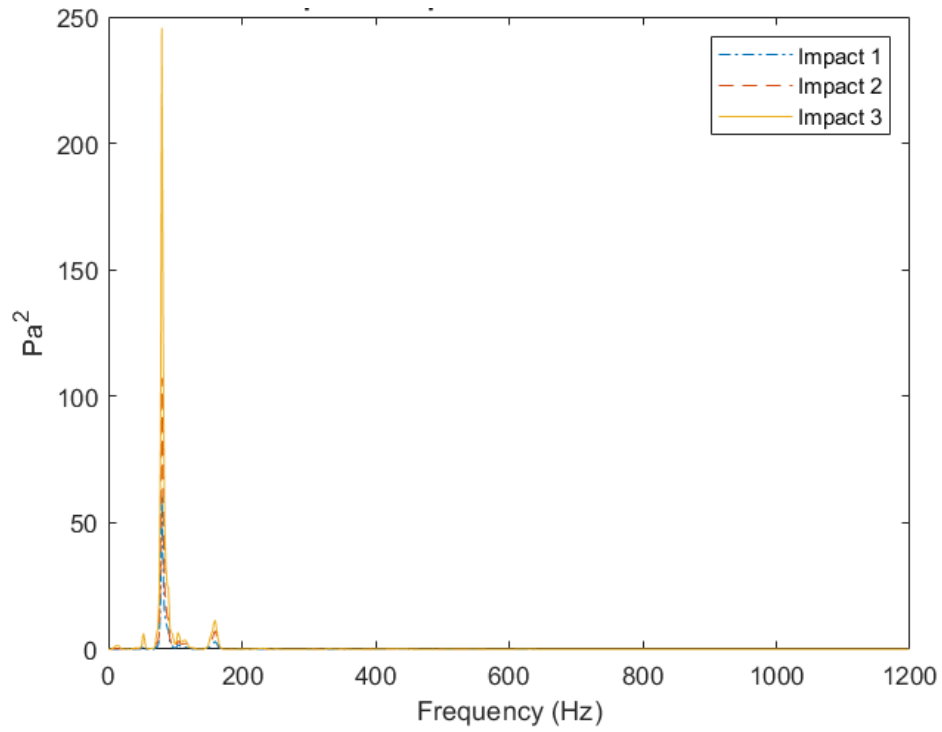


Figure 30. Autospectrum of Electret 1 signal for three axial impacts ($f \leq 1200$ Hz)

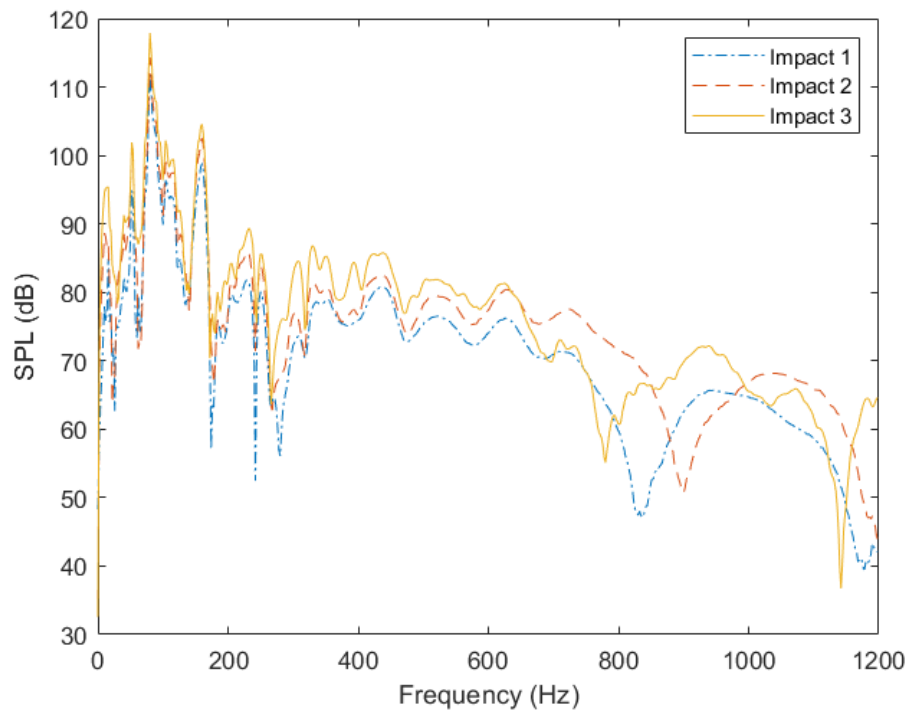


Figure 31. Autospectrum (dB) of Electret 1 signal for three axial impacts ($f \leq 1200$ Hz)

While Figure 30 shows that there are two dominant frequencies seen at 80 Hz and 160 Hz, data are better visualized with the logarithmic scaling in Figure 31. As shown in Figure 31, the SPL drops significantly for frequencies above 500 Hz. This behavior is likely due to the damping within the gel at these higher frequencies, though a definitive conclusion would need further study. The signal for each impact is therefore best represented by the signal's frequency content below 500 Hz. The same autospectra for Electret 1 shown in Figure 31 are repeated in Figure 32 with the frequency content truncated at 500 Hz. The same 500 Hz bandwidth is shown for Electret 2 in Figure 33.

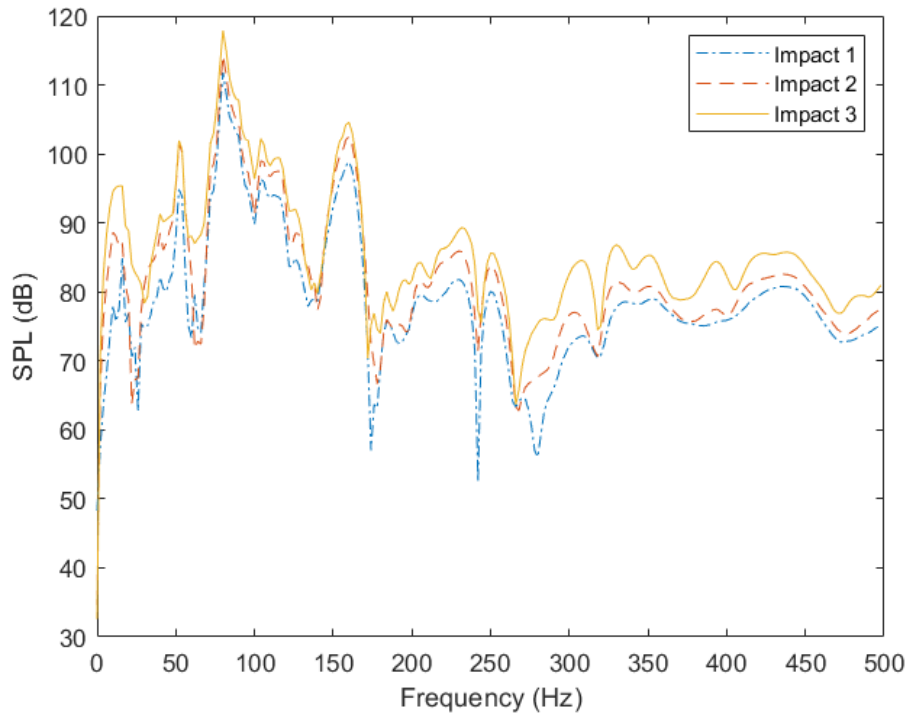


Figure 32. Autospectrum (dB) of Electret 1 signal for three axial impacts ($f \leq 500\text{Hz}$)

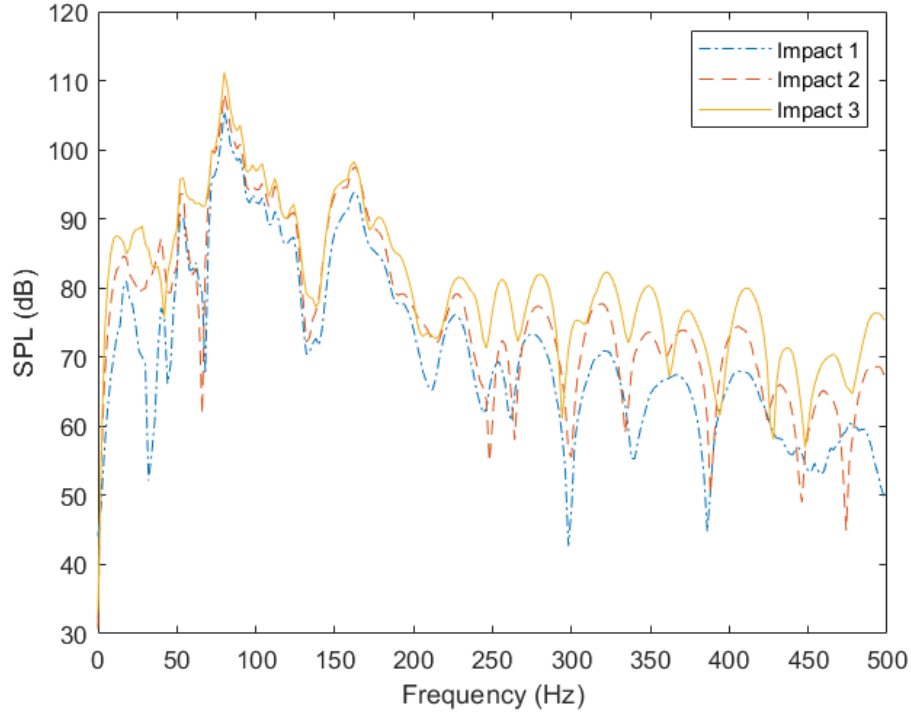


Figure 33. Autospectrum (dB) of Electret 2 signal for three axial impacts ($f \leq 500\text{Hz}$)

While Electret 1 and Electret 2 have similar frequency responses, there are a few key differences, such as high amplitude frequencies for Electret 1 between 200 and 250 Hz that were not prominent for Electret 2. Furthermore, the response at Electret 1 was consistently higher. The difference between the two electrets' autospectral content is likely due, in part, to the acoustic modes present from the gelatin acting as a cylindrical chamber with free walls. Similar to how a vibration sensor's measurement is affected by its location on a bar with vibrational modes, an acoustic chamber produces different measured signals based on the sensor location. These acoustic modes are likely complex in nature and not easily modeled since the gelatin's walls are not rigid. Furthermore, the gelatin's material properties are complex (*i.e.* viscoelastic) and possibly nonlinear and frequency dependent. In conjunction with the impact of different acoustic modes, the damping appears to be significant, as the measured signal at Electret 2 is

consistently lower in amplitude than at Electret 1, which is located closer to the source of impact. Further indication of greater damping in Electret 2's signal can be seen in the flattening of resonant peaks in the frequency-domain response, most clearly seen around 160 Hz, as well as in the loss of signals above 200 Hz. In order to distinguish between these two factors and better understand them, it would be necessary to have a larger array of microphones. At a minimum, a third electret placed at an axially symmetric position with Electret 2 near to the source of impact should allow for better differentiation of these two effects. A potential experimental setup for future work is discussed in Section 5.2.

The significance of the resonant peaks measured by the electret microphones is better understood when compared to the accelerometer's vibration response. Before directly comparing the autospectrum of the accelerometer with those of the acoustic sensors, which have been shown to be capable of measuring frequencies up to 500 Hz, it is worth briefly discussing the accelerometer's frequency response up to 10 kHz, as shown in Figure 34.

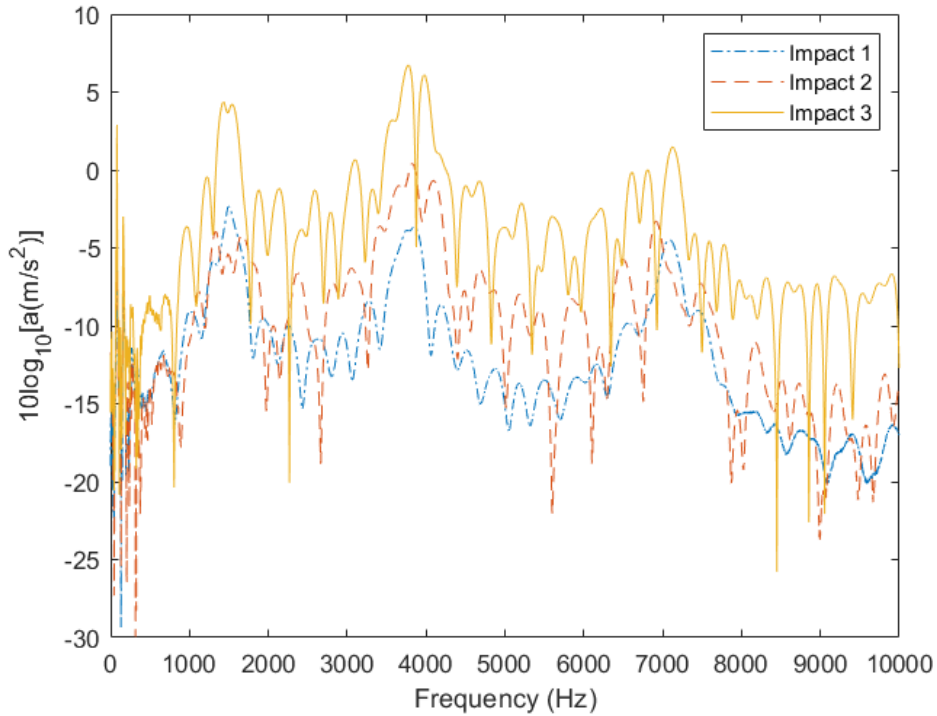


Figure 34. Vibration response of accelerometer signal for three axial impacts ($f \leq 10,000\text{Hz}$)

The bar's modal frequencies, previously shown in *Figure 26* for a bare bar (no gel), are present in the accelerometer's measurements, though, the frequencies of individual modes cannot be identified based on the single measurement location. This shows that, to some extent, the bar vibrates as a non-coupled system. While high frequencies above 500 Hz might be measured by the accelerometer, they do not transmit through the gelatin due to the material's high damping, and thus cannot be measured by the electret microphones on the gelatin's surface. However, the microphones are capable of picking up lower frequencies, including what appear to be the modal frequencies of the coupled bar-gel system, below 500 Hz, shown in *Figure 35*.

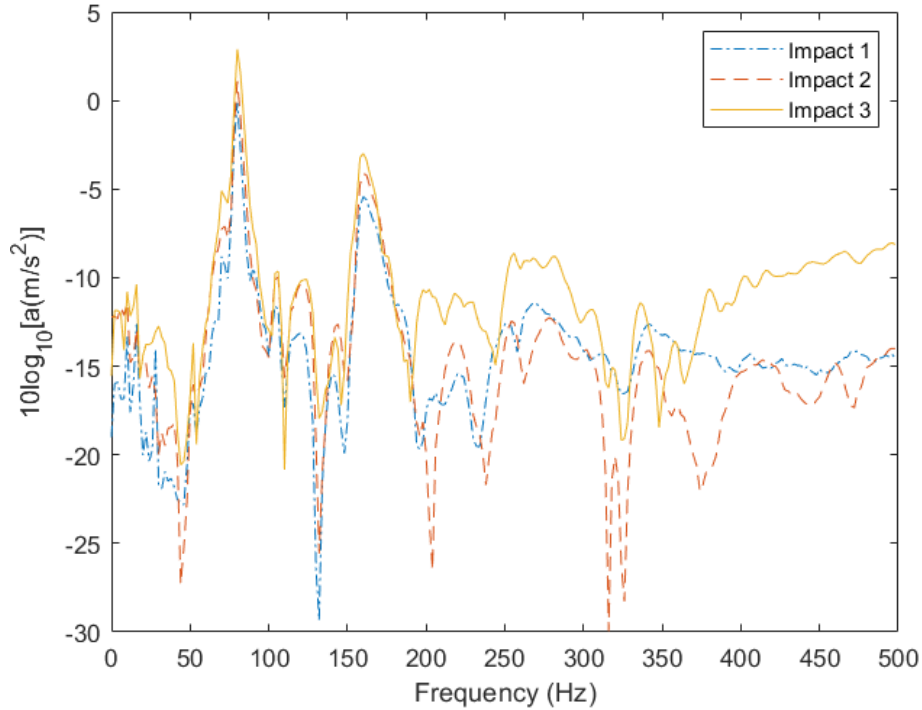


Figure 35. Vibration response of accelerometer signal for three axial impacts ($f \leq 500\text{Hz}$)

Again, in an actual implementation of the proposed approach, a measured acceleration would not be accessible. Nevertheless, those data are shown here to provide more insight into some of the characteristics measured by the microphones. The 80 and 160 Hz frequencies measured by both electrets, for example, may initially appear to be harmonic modes, as they are integer multiples of each other. While these integer ratio frequencies are expected of axial modes, these frequencies are present in the accelerometer's vibration response. Since the unidirectional accelerometer is not able to measure axial modes in its current orientation, these frequencies are instead likely due to bending modes of the coupled bar-gel structure. While bending modes of a free-free beam do not occur sequentially, non-sequential modes can occur at values near to integer multiples of one another in the first few modes (Caresta, 2009). The presence of these modes at integer multiples of one another may possibly be explained by the

viscoelastic properties of the gelatin. Specifically, the damping of the gel is frequency dependent and possibly nonlinear, lowering resonant frequencies by different factors. Frequencies present in the acoustic autospectra that are not measured by the accelerometer, such as at 54 Hz, are assumed to be either axial modes or acoustic modes of the gel, acting as a cylindrical chamber. While it is difficult to know the precise reason for the presence of resonant frequencies, they are clearly identifiable in the measured signal for an axial impact.

4.1.1 Axial Impact Regression Models

After identifying some of the trends in the acoustic autospectral data through the methods discussed here, their correlation with impact characteristics in the time-domain were considered as a means of determining the feasibility of the measurement technique. The previous figures showed the intermediate post-processed data before attempting to correlate the frequency-based acoustic data to the hammer's time-domain data. Regression models were created for $n = 59$ axial impacts relating acoustic autospectral amplitudes at discrete frequencies, and the acoustic energy within chosen frequency bands, to the hammer's peak impact and primary impulse. This set of chosen characteristics results in four pairs of regressions performed for each case, with each pair consisting of a linear and quadratic model. While one might assume that a linear fit would naturally be better, it is suspected there are some non-linearities present in the system due to the gel. Therefore, linear and quadratic models were both examined as a means to relate the acoustic autospectrum data to the impact in the time-domain, for a total of eight models for axial impacts. For each model, outliers with residuals greater than three standard deviations from the initial model fit were removed before re-fitting the model and generating the final models shown here. These outliers are likely "mis-hits" during experimentation, where poor contact was made

between the force transducer on the impulse hammer's tip and the square end of the metal bar, but the structure was obviously still excited.

4.1.2 Autospectral Amplitudes as a Function of Peak Force

First, least squares regression models were fit to the data to determine the level of correlation between acoustic resonant frequency amplitudes and the peak magnitude of the force. Exemplar linear regressions for Electret 1 and Electret 2 autospectral data at 160 Hz can be seen in Figure 36 and Figure 37, respectively. In these figures, the peak of the magnitude of the autospectra measured by the electret microphones is shown as a function of the peak of the force impact from the time domain (see Figure 28). Similarly, Figure 38 and Figure 39 show 2nd order polynomial model fits for autospectral amplitudes at 160 Hz for Electret 1 and Electret 2, respectively. The 160 Hz frequency was chosen as it was previously identified as being one of the most prominent frequencies present for both acoustic sensors, while exhibiting different levels of model strength between them. The R^2_{adj} value shown in the following figures is a modification of the R^2 value, which indicates the variance present in the dependent variable that is predictable from the independent variable, where a higher value indicates a better fit of the data. The modification of the R^2 value penalizes models with more parameters to avoid overfitting.

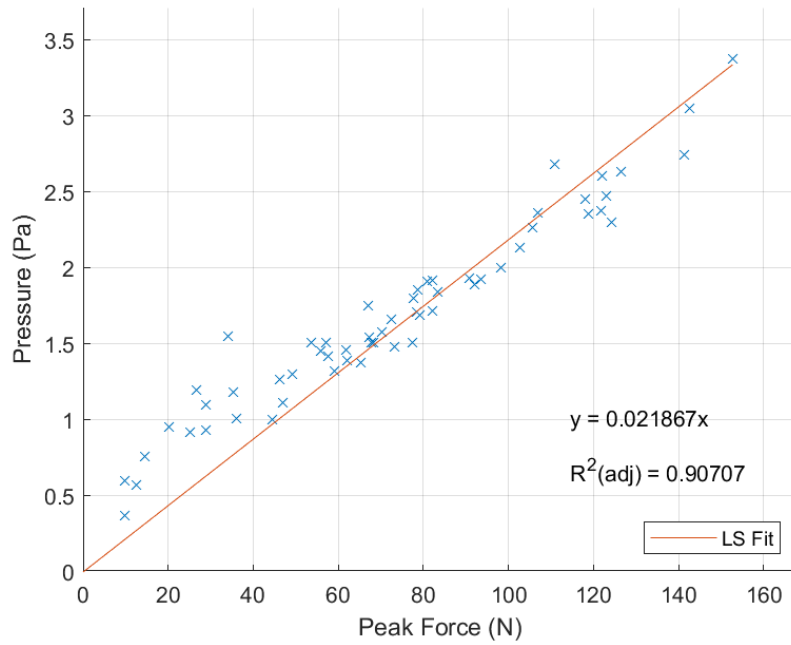


Figure 36. Linear model of Electret 1 autospectrum magnitude at 160 Hz as a function of peak impact force

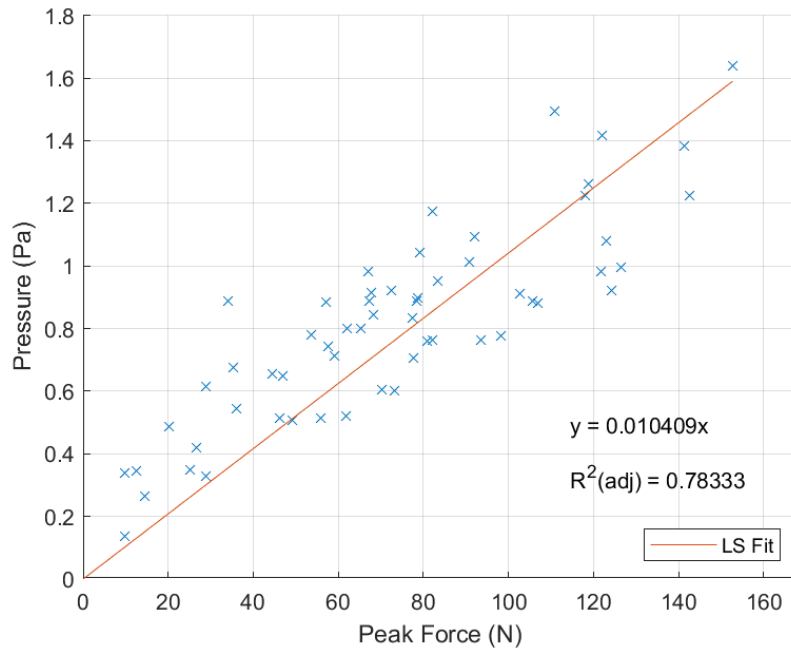


Figure 37. Linear model of Electret 2 autospectrum magnitude at 160 Hz as a function of peak impact force

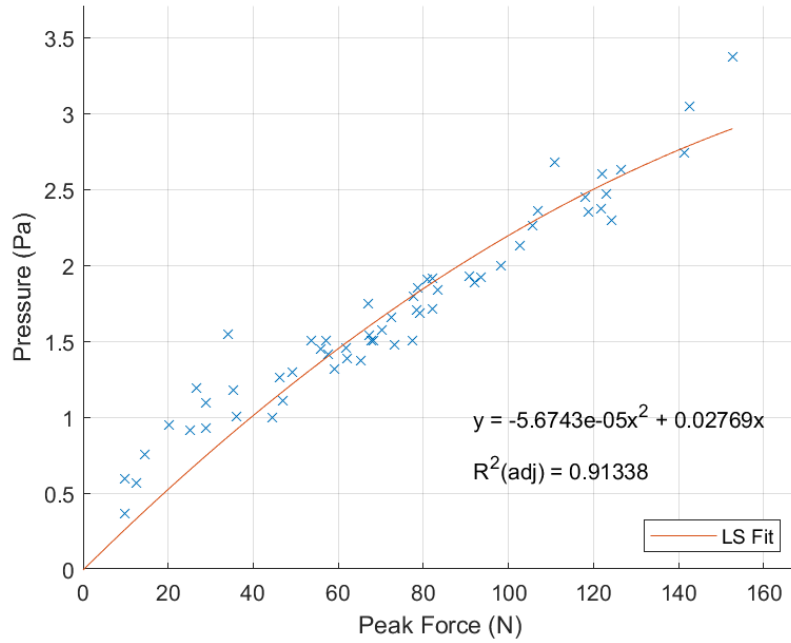


Figure 38. Quadratic model of Electret 1 autospectrum magnitude at 160 Hz as a function of peak impact force

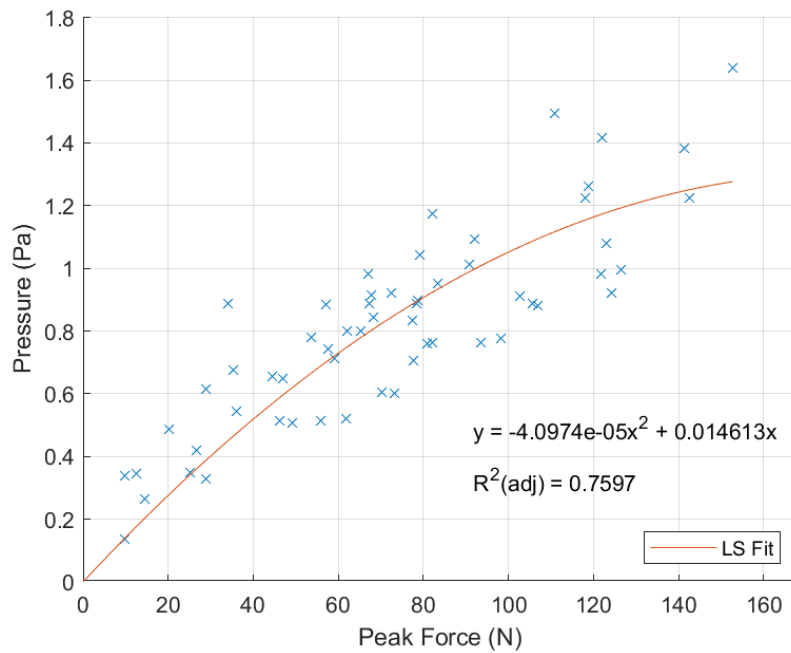


Figure 39. Quadratic model of Electret 2 autospectrum magnitude at 160 Hz as a function of peak impact force

In order to determine the efficacy of each regression model, the adjusted coefficient of determination (R^2_{adj}), Akaike Information Criterion (AIC), and Bayesian Information Criterion (BIC) were calculated. All three model criteria compare goodness of fit and penalize for overfitting, where higher R^2_{adj} and more negative AIC and BIC values indicate a better regression fit (Hastie, 2017). The R^2_{adj} value can be used to evaluate both the predictability of the peak force based on frequency-domain characteristics and the efficacy of increasing model complexity, while AIC and BIC values are used to evaluate the benefit of increasing model complexity. Table 2 through Table 5 summarize the model criteria for regressions where the autospectral amplitude at specified resonant frequencies was examined as a function of the impact peak force for all sensors. A peak-picking method performed in MATLAB accounts for slight variation in the experimentally determined frequencies to ensure that the resonant amplitudes are appropriately chosen. The hammer's self-correlation was determined by treating the chosen discrete frequency amplitudes, rather than of peaks near these frequencies, as a function of the peak force. This was necessary due to the relatively flat frequency response of the hammer, making peak-picking ineffective.

Table 2. Axial Impact Model Criteria for Electret 1: Acoustic Autospectral Amplitude vs. Peak Impact

Frequency (Hz)	Linear Model			Quadratic Model		
	R^2_{adj}	AIC	BIC	R^2_{adj}	AIC	BIC
54	0.9051	-10.024	-7.963	0.8998	-8.723	-4.602
80	0.8887	183.7	185.7	0.8803	179.7	183.8
104	0.8575	0.171	2.232	0.8463	-8.810	-4.689
160	0.9071	6.970	9.030	0.9134	-12.32	-8.198
250	0.9281	-244.5	-242.4	0.9466	-278.6	-274.5
306	0.9011	-307.6	-305.5	0.8966	-305.9	-301.8
440	0.9259	-234.7	-232.7	0.9672	-294.2	-290.2

Table 3. Axial Impact Model Criteria for Electret 2: Acoustic Autospectral Amplitude vs. Peak Impact

Frequency (Hz)	Linear Model			Quadratic Model		
	R^2_{adj}	AIC	BIC	R^2_{adj}	AIC	BIC
54	0.4616	1.898	3.941	0.3547	-1.022	3.064
80	0.8870	100.4	102.4	0.8818	91.05	95.17
104	0.8245	-41.89	-39.83	0.8125	-57.47	-53.35
160	0.7833	-21.12	-19.06	0.7597	-36.59	-32.47
250	0.6154	-264.1	-262.0	0.6499	-263.2	-259.1
306	0.8321	-259.0	-257.0	0.8692	-263.3	-259.2
440	0.4738	-270.2	-268.2	0.5079	-268.9	-264.8

Table 4. Axial Impact Model Criteria for Accelerometer: Acoustic Autospectral Amplitude vs. Peak Impact

Frequency (Hz)	Linear Model			Quadratic Model		
	R^2_{adj}	AIC	BIC	R^2_{adj}	AIC	BIC
54	0.2415	-265.5	-263.5	0.1431	-266.2	-262.1
80	0.8641	-52.76	-50.70	0.8657	-77.50	-73.41
104	0.6378	-298.9	-296.9	0.5564	-311.7	-307.6
160	0.8162	-174.6	-172.6	0.8062	-193.5	-189.4
250	0.3994	-258.4	-256.4	0.3709	-256.5	-252.4
306	0.5305	-304.5	-302.5	0.4458	-306.3	-302.2
440	0.4087	-255.3	-253.2	0.3529	-254.0	-249.9

Table 5. Axial Impact Model Criteria for Impact Hammer: Acoustic Autospectral Amplitude vs. Peak Impact

Frequency (Hz)	Linear Model			Quadratic Model		
	R^2_{adj}	AIC	BIC	R^2_{adj}	AIC	BIC
54	0.9129	-444.5	-263.5	0.9086	-449.4	-445.3
80	0.8956	-488.4	-50.70	0.8886	-493.2	-489.1
104	0.8861	-521.8	-296.9	0.8795	-529.7	-525.6
160	0.9286	-563.5	-172.6	0.9318	-577.3	-573.2
250	0.9559	-579.8	-256.4	0.9696	-613.8	-609.7
306	0.9510	-555.0	-302.5	0.9650	-587.5	-583.4
440	0.9695	-542.6	-253.2	0.9749	-561.8	-557.6

Overall, the model criteria shown in Table 2 show that, for Electret 1, a quadratic model is best when correlating frequency amplitudes with the peak force, as indicated by higher R^2_{adj} values and lower AIC and BIC values when compared to the linear models. Correlations moderately improve for Electret 1 for higher frequencies that approach 500 Hz, which is not necessarily expected since the resonant frequencies in this range are not very prominent (see Figure 32). The regression models for Electret 2, as summarized in Table 3, show that the acoustic autospectra are not as highly correlated to the peak force as for Electret 1. Furthermore, there is disagreement between the different model criteria on preference towards a linear or quadratic fit. For example, at 104 Hz, the R^2_{adj} value suggests a linear model is better, while AIC and BIC values suggest a quadratic model is better. In general, the most highly correlated models for Electret 2 are those based on the most prominent frequencies, found at 80, 104, and 160 Hz. The accelerometer model criteria summarized in Table 4 show that the regression models are only useful for the two frequencies at 80 and 160 Hz, which were previously inferred to be bending modes.

The model criteria shown in Table 5 summarize results for regression models in which the impact hammer frequency amplitude was treated as a function of the time-domain peak value. This self-correlation result is interesting in that it points to higher frequencies being more correlated to impact magnitude than lower frequencies. Given the short time duration of the hammer's force curve, this result is not too surprising. In the ideal case, the hammer's self-correlation would be perfect since all frequencies would be excited equally. However, in the time-domain response of the hammer, as shown Figure 28, it is apparent that the hammer impact is not ideal. Instead of exciting all frequencies equally, the hammer is exciting higher frequencies

more than lower ones, leading to lower correlations of its autospectral magnitude at lower frequencies to its peak magnitude in the time domain.

As previously mentioned, frequencies that appear in the acoustic signals, but not in the accelerometer, are either axial modes of the bar-gel system or acoustic modes of the gel acting as an acoustic chamber. However, with the present data, it is not possible to reasonably distinguish between the two causes of these frequencies by comparing the frequency content of the acoustic sensors. The suppression of a frequency's amplitude in the acoustic autospectra could indicate either an acoustic node at the point of measurement, or that axial modes are damped as waves travel along the structure. Again, while it may not be possible to categorize all the measured frequencies, the current work aims to show that the measured acoustic signal and the peak force of the applied impact are correlated. In future work, a sensor array with more measurement locations would allow for further investigation of the cause of these frequencies, discussed later in Section 5.2. Overall, while it looks like the peak-picking method may provide a means with which to develop a reasonable model, there is an obvious disparity in regression model quality between Electret 1 and Electret 2, such that Electret 1 is more capable of predicting the peak force.

4.1.3 Energy in a Frequency Band as a Function of Peak Force

In an attempt to create a better model that could apply to both acoustic sensors, it was decided to compare the total acoustic energy in a specified frequency band to the peak of the impact force in the time domain. This band energy method was chosen to account for difficulty in selecting flattened peaks due to heavy damping and in an attempt to extrapolate more information from both acoustic sensors that could be used to determine the peak impact force.

The three chosen bands all begin at 50 Hz and encompass an increasing bandwidth up to 200, 500, and 1200 Hz, respectively. These upper band limits were chosen as they each mark significant changes in the acoustic autospectra. Specifically, resonant frequencies occur in both acoustic sensors up to 200 Hz, and autospectral amplitudes are low after 500 Hz. The upper limit of the electrets' calibrated range was previously determined in Section 3.2.1 to be 1200 Hz, thus the selection of 1200 Hz as the uppermost band limit. The Root Mean Square (RMS) value of the autospectrum for each chosen band was calculated to represent the energy content in that band. Table 6 through Table 9 summarize the model criteria for all sensors in which a correlation between the band energy and the peak impact force is examined. While each sensor is not discussed in depth, the results are shown here for continuity and comparison with earlier results in this section.

Table 6. Axial Impact Model Criteria for Electret 1: Acoustic Band Energy vs. Peak Impact

Frequency Band (Hz)	Linear Model			Quadratic Model		
	R^2_{adj}	AIC	BIC	R^2_{adj}	AIC	BIC
50 - 200	0.8949	-1.4053	0.6552	0.8892	-8.5279	-4.4070
50 - 500	0.8973	-64.88	-62.82	0.8923	-72.417	-68.296
50 - 1200	0.8981	-119.2	-117.1	0.8934	-126.91	-122.78

Table 7. Axial Impact Model Criteria for Electret 2: Acoustic Band Energy vs. Peak Impact

Frequency Band (Hz)	Linear Model			Quadratic Model		
	R^2_{adj}	AIC	BIC	R^2_{adj}	AIC	BIC
50 - 200	0.8811	-56.73	-54.67	0.8828	-73.94	-69.82
50 - 500	0.8826	-119.9	-117.9	0.8842	-136.9	-132.8
50 - 1200	0.8829	-174.0	-171.9	0.8841	-190.6	-186.5

Table 8. Axial Impact Model Criteria for Accelerometer: Acoustic Bandwidth Energy vs. Peak Impact

Frequency Band (Hz)	Linear Model			Quadratic Model		
	R^2_{adj}	AIC	BIC	R^2_{adj}	AIC	BIC
50 - 200	0.8595	-243.5	-241.4	0.8486	-252.4	-248.3
50 - 500	0.8338	-286.8	-284.7	0.8167	-295.1	-291.0
50 - 1200	0.5681	-205.8	-203.8	0.5391	-204.1	-200.0

Table 9. Axial Impact Model Criteria for Impact Hammer: Acoustic Bandwidth Energy vs. Peak Impact

Frequency Band (Hz)	Linear Model			Quadratic Model		
	R^2_{adj}	AIC	BIC	R^2_{adj}	AIC	BIC
50 - 200	0.9351	-533.0	-531.0	0.9394	-547.9	-543.8
50 - 500	0.9732	-577.5	-575.4	0.9852	-622.2	-618.1
50 - 1200	0.9742	-565.9	-563.8	0.9790	-584.8	-580.7

Notably, the correlation between the band energy and the peak impact is very similar for both electret microphones. For Electret 1, while the correlation is not necessarily higher for the band energy of the measured signal than the autospectral amplitude shown previously, these results further solidify the measurements' strong correlation to the peak impact. For Electret 2, the band energy models are more correlated to the peak force than the results from the peak-picking method. In Electret 2, there is a decrease in model correlation when including frequencies above 200 Hz, which is the frequency previously identified to be the point at which resonant frequencies stopped being observed in the response. For both electrets, there are diminishing returns to including energy contributions by signals with frequencies above 500 Hz, which is not an unexpected result based on previous conclusions. The accelerometer is the only case in which the R^2_{adj} value decreases when including higher frequencies in the analyzed band.

This decrease is due to the damping of high frequencies almost immediately after the impact, and thus does not represent the structure's free response.

Before drawing conclusions on the feasibility of the measurement technique based on correlations of the acoustic autospectral characteristics to peak force, another model was considered which takes into account a different metric of the applied force. Since the hammer impact occurs over a finite amount of time, it is reasonable to assume that the timespan over which it occurs varies between tests. Thus, the system response may not be solely dependent on the magnitude of the impact, but also on the amount of time over which the force is applied.

4.1.4 Autospectral Amplitude as a Function of the Primary Impulse

The primary impulse, previously defined earlier in Section 4.1, is the second characteristic of the impact force considered in this study. Table 10 through Table 13 show the model criteria for when acoustic autospectral amplitude is examined as a function of the primary impulse. For axial impacts, the primary impulse occurs in $\Delta t \approx 0.76$ ms.

Table 10. Axial Impact Model Criteria for Electret 1: Acoustic Autospectral Amplitude vs. Primary Impulse

Frequency (Hz)	Linear Model			Quadratic Model		
	R^2_{adj}	AIC	BIC	R^2_{adj}	AIC	BIC
54	0.9093	-25.60	-23.54	0.9238	-28.13	-24.01
80	0.9046	160.9	163.0	0.9023	162.9	167.0
104	0.8758	-21.90	-19.84	0.8645	-22.35	-18.22
160	0.9486	-42.85	-40.79	0.9482	-49.33	-45.21
250	0.9536	-284.4	-282.3	0.9566	-297.1	-293.0
306	0.8722	-304.5	-302.4	0.8920	-306.2	-302.1
440	0.9285	-246.8	-244.8	0.9182	-255.9	-251.7

Table 11. Axial Impact Model Criteria for Electret 2: Acoustic Autospectral Amplitude vs. Primary Impulse

Frequency (Hz)	Linear Model			Quadratic Model		
	R^2_{adj}	AIC	BIC	R^2_{adj}	AIC	BIC
54	0.4508	-7.423	-5.3796	0.3755	-6.918	-2.8317
80	0.9078	74.46	76.52	0.9014	74.96	79.08
104	0.8496	-65.40	-63.34	0.8324	-71.27	-67.15
160	0.7978	-39.04	-36.98	0.7673	-45.49	-41.37
250	0.5646	-264.8	-262.8	0.6538	-266.8	-262.7
306	0.7500	-244.0	-242.0	0.8481	-256.3	-252.2
440	0.4107	-268.5	-266.5	0.4919	-268.6	-264.5

Table 12. Axial Impact Model Criteria for Accelerometer: Autospectral Amplitude vs. Primary Impulse

Frequency (Hz)	Linear Model			Quadratic Model		
	R^2_{adj}	AIC	BIC	R^2_{adj}	AIC	BIC
54	0.2140	-268.6	-266.5	0.1386	-267.7	-263.5
80	0.8896	-79.18	-77.12	0.8885	-94.18	-90.09
104	0.6353	-310.9	-308.9	0.5465	-318.4	-314.3
160	0.8494	-201.3	-199.3	0.8342	-211.0	-206.9
250	0.3601	-261.3	-259.3	0.3833	-259.6	-255.5
306	0.4996	-310.2	-308.1	0.4344	-309.5	-305.4
440	0.3774	-260.0	-258.0	0.3631	-258.0	-253.9

Table 13. Axial Impact Model Criteria for Impact Hammer: Autospectral Amplitude vs. Primary Impulse

Frequency (Hz)	Linear Model			Quadratic Model		
	R^2_{adj}	AIC	BIC	R^2_{adj}	AIC	BIC
54	0.9093	-25.60	-23.54	0.9238	-28.13	-24.01
80	0.9046	160.9	162.98	0.9023	162.9	167.0
104	0.8758	-21.90	-19.84	0.8645	-22.35	-18.22
160	0.9486	-42.85	-40.79	0.9482	-49.33	-45.21
250	0.9536	-284.4	-282.3	0.9566	-297.1	-293.0
306	0.8722	-304.5	-302.4	0.8920	-306.2	-302.1
440	0.9285	-246.8	-244.8	0.9182	-255.9	-251.7

For both acoustic sensors, there is modest improvement in R^2_{adj} values when correlating the acoustic autospectral amplitudes with the primary impulse instead of peak force, with the exception of the single 306 Hz autospectral amplitude. The increase in R^2_{adj} values suggests that there is better predictability of the primary impulse than of the peak force. Still, the linear regression models utilizing either peak force or the primary impulse as the independent variable result in reasonably good fits with the peak-picking method. The frequencies that provide the highest model correlation occur at 80, 104, and 160 Hz for the current physical model, though, Electret 1's position allows for predictive models to be developed for more frequencies. For both acoustic sensors at these same three frequencies, AIC and BIC values generally indicate an improvement from choosing a quadratic model over a linear one. This decrease in AIC and BIC values appears to contradict the lower R^2_{adj} values obtained for the quadratic model relative to the linear model. However, this decrease in AIC and BIC values can be attributed to the AIC and BIC values accounting for the biased residuals found in the linear models, which tend to be larger at lower frequencies. In some cases, the AIC and BIC values do not indicate an improvement in choosing a higher order model. Since there is no decisively superior model when using the peak-picking method, both models will continue to be shown for comparison.

4.1.5 Energy in a Frequency Band as a Function of the Primary Impulse

The final set of regression models are for when band energy is treated as a function of the primary impulse. Table 14 through Table 17 summarize the model criteria for this case for all sensors as well as for the hammer's self-correlation.

Table 14. Axial Impact Model Criteria for Electret 1: Bandwidth Energy vs. Primary Impulse

Frequency Band (Hz)	Linear Model			Quadratic Model		
	R^2_{adj}	AIC	BIC	R^2_{adj}	AIC	BIC
50 – 200	0.9167	-29.07	-27.01	0.9123	-27.62	-23.50
50 - 500	0.9193	-93.03	-90.97	0.9150	-91.7	-87.5
50 - 1200	0.9204	-147.7	-145.6	0.9161	-146.4	-142.2

Table 15. Axial Impact Model Criteria for Electret 2: Bandwidth Energy vs. Primary Impulse

Frequency Band (Hz)	Linear Model			Quadratic Model		
	R^2_{adj}	AIC	BIC	R^2_{adj}	AIC	BIC
50 - 200	0.9109	-88.17	-86.11	0.9051	-92.68	-88.56
50 - 500	0.9121	-151.4	-149.3	0.9063	-155.6	-151.5
50 - 1200	0.9122	-205.4	-203.3	0.9064	-209.4	-205.3

Table 16. Axial Impact Model Criteria for Accelerometer: Bandwidth Energy vs. Primary Impulse

Frequency Band (Hz)	Linear Model			Quadratic Model		
	R^2_{adj}	AIC	BIC	R^2_{adj}	AIC	BIC
50 - 200	0.8916	-273.4	-271.3	0.8827	-273.6	-269.5
50 - 500	0.8651	-313.7	-311.6	0.8521	-314.2	-310.1
50 - 1200	0.5503	-213.8	-211.7	0.5740	-212.2	-208.1

Table 17. Axial Impact Model Criteria for Hammer Impact: Bandwidth Energy vs. Primary Impulse

Frequency Band (Hz)	Linear Model			Quadratic Model		
	R^2_{adj}	AIC	BIC	R^2_{adj}	AIC	BIC
50 - 200	0.9735	-600.0	-598.0	0.9726	-599.6	-595.5
50 - 500	0.9828	-616.9	-614.8	0.9826	-617.7	-613.6
50 - 1200	0.9937	-661.3	-659.3	0.9941	-663.0	-658.9

When changing the bandwidth energy model's independent variable from peak force to the primary impulse, the models improve slightly for both electrets. There is no clear benefit to

choosing a quadratic model over a linear one for either microphone as there is not a unanimous agreement among model criteria and any improvements in model criteria from choosing the quadratic model are marginal. Regardless of whether a linear or quadratic model is chosen, the best performing model type of all four considered in this section is when band energy is treated as a function of the primary impulse.

4.1.6 Axial Impact Results Summary

Overall, for axial impacts, there is a significant correlation between the electret microphones' acoustic autospectra and the impact applied. The best performing models for Electret 1 were those that treated acoustic autospectral amplitudes as a function of the primary impulse, and the best performing models for Electret 2 were those that treated bandwidth energy estimates as a function of the primary impulse. The difference in the microphones' correlations of autospectral amplitude to impact force characteristics highlights the importance of microphone placement on the gel's surface due to resonances being more apparent near the source of impact. Furthermore, overall energy was shown to be more useful further from the impact due to damping decreasing the resonance amplitudes. Both discrete frequencies based on peak-picking methods and band energies that encompass the resonant frequencies appear to be good predictors of impact characteristics for the test cases and model approaches considered here. While the usage of discrete frequencies has the potential to provide a higher level of correlation than band energies, the autospectral amplitudes' correlation to impact characteristics is clearly dependent on sensor placement. More highly correlated models were resulted when the primary impulse, rather than the peak force, was assumed to be the independent variable, but both seem to be reasonably predictable for axial impacts. This ability to correlate acoustic

autospectra with force characteristics for axial impacts is very promising when it comes to determining the feasibility of the measurement technique under consideration since biomechanical forces are largely axial in nature. While this allows for characterization of purely axial forces, there are also shear forces transferred between bones during biomechanical motion. Shear forces are considered in the next sections by experimenting with transverse impacts with the sensors in different planes relative to the impact direction. Furthermore, transverse excitations may also allow for better understanding of the nature of the resonances seen in axial impacts since it is expected that the bending modes would be more easily excited.

4.2 Transverse Impact with In-Plane Measurements

The second set of experiments consisted of applying transverse impacts to the bar's end with in-plane sensors, as illustrated back in Figure 27. As was done for the axial impacts, some sample data from three IP transverse impacts is shown below, followed by regression models which summarize the correlation between acoustic autospectral characteristics and time-domain impact characteristics. Sample time data for three IP transverse impacts are shown below in Figure 40.

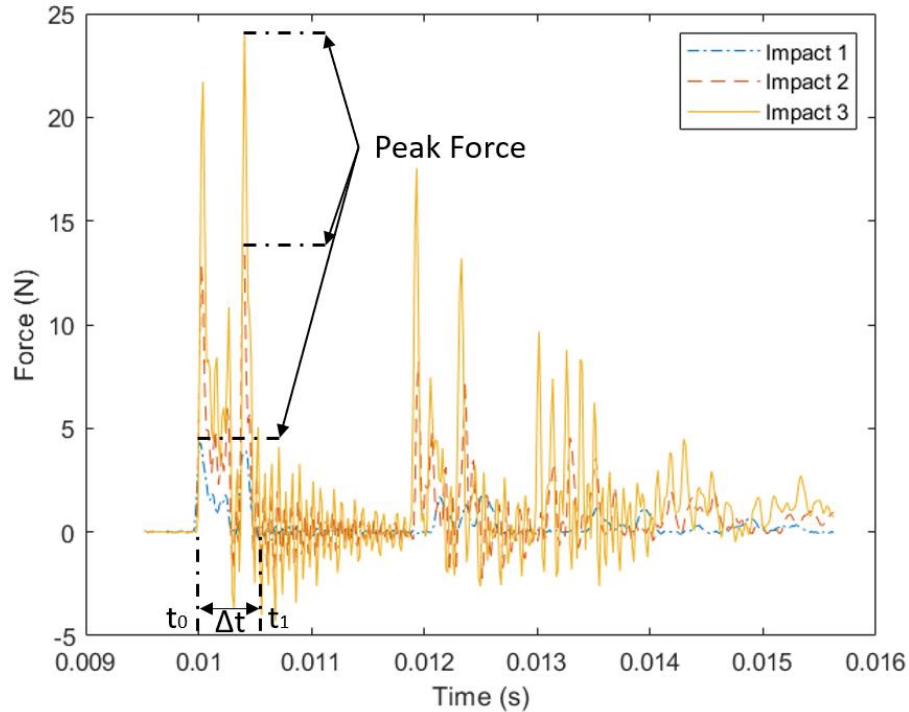


Figure 40. Sample time data of impact hammer for three transverse IP impacts with labeled peaks and impulse times

When compared to the hammer signal for the axial impacts discussed in Section 4.1, the force signal is not as easily characterized by a single peak force level. Similar to how axial impacts present as a series of impacts, transverse impacts also create more than one single force peak in the time domain. Impacts occur in pairs initially, with the peak force occurring in either of the first pair of impacts. Clearly in this configuration it is more difficult to introduce a single impact force. However, since the transverse impacts still develop very similar force time-domain responses from impact to impact, the peak force was still considered as a metric of the impact in regression models. In the same way that previous regression models were created for axial impacts in which acoustic autospectral characteristics were correlated with impact force characteristics, regression models were also created for $n = 65$ transverse impacts with in-plane sensors. The force in the time-domain for three in-plane impacts is shown in Figure 40. The time

values of t_0 and t_1 mark the beginning and end, respectively, of the primary impulse. The difference between time t_1 and t_0 gives a $\Delta t \approx 1.6$ ms for transverse impacts. Force levels are generally lower for transverse impacts than axial ones as a result of the boundary conditions imposed on the structure and the resultant lack of structural mass to oppose rotational and transverse rigid body motion when impacted.

The corresponding acoustic data recorded by Electret 1 for each transverse impact shown in Figure 40 is shown in Figure 41. Compared to the time-domain response for Electret 1 for axial impacts, the peak magnitude of the response for transverse impacts is lower, as expected from the smaller applied force. The acoustic autospectra for Electret 1 and Electret 2 are shown for the same three transverse impacts with in-plane measurements in Figure 42 and Figure 43, respectively.

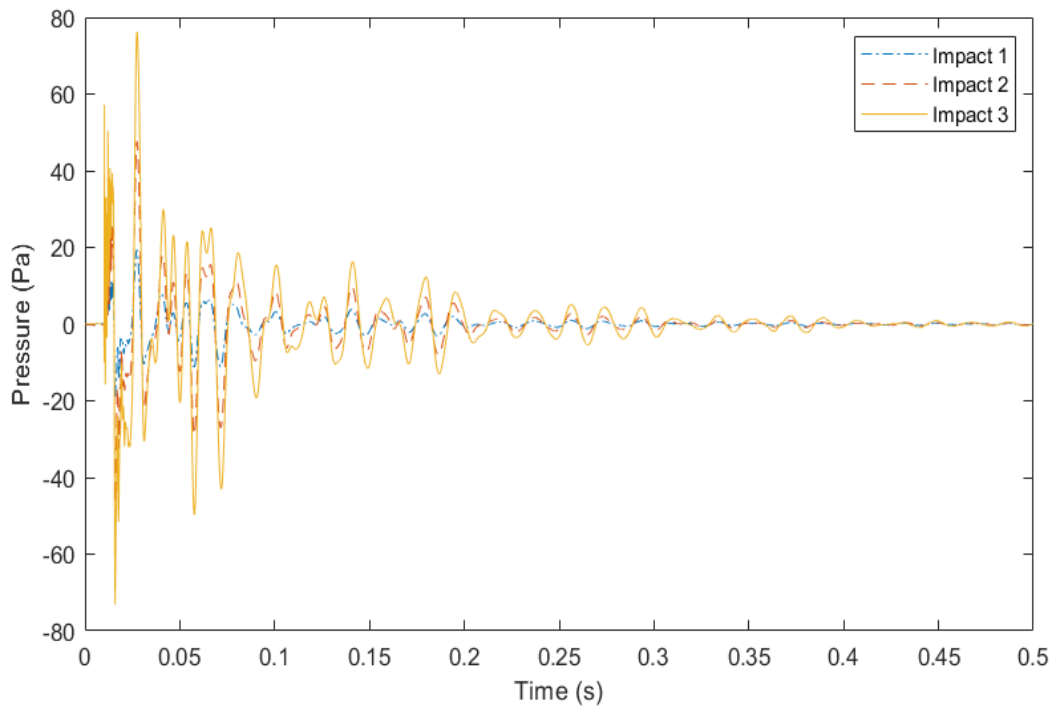


Figure 41. Sample time data of Electret 1 for three IP transverse impacts

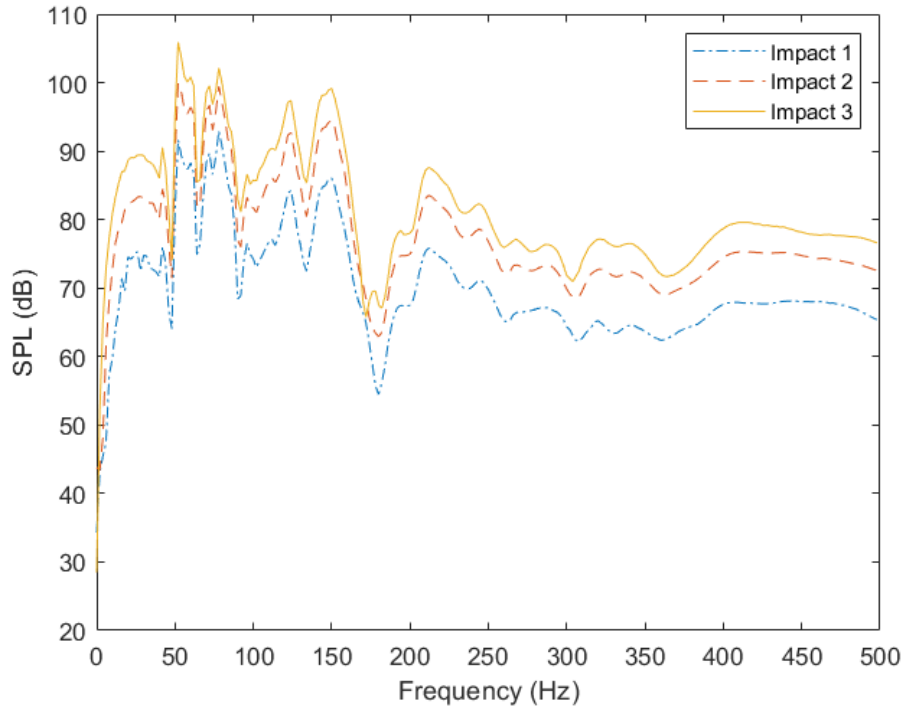


Figure 42. Autospectrum (dB) of Electret 1 signal for three IP transverse impacts ($f \leq 500\text{Hz}$)

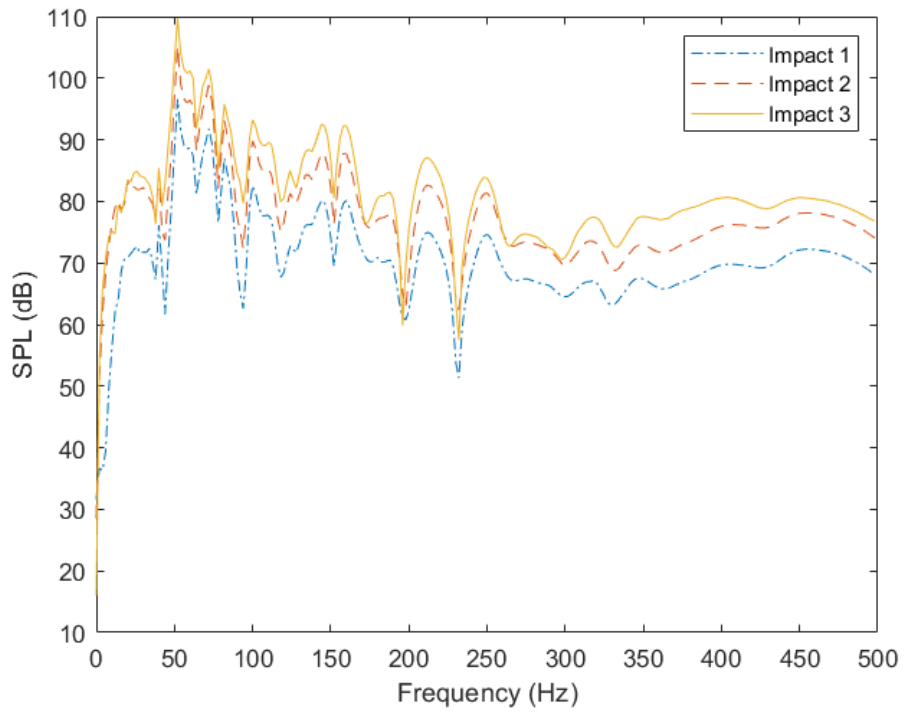


Figure 43. Autospectrum (dB) of Electret 2 signal for three IP transverse impacts ($f \leq 500\text{Hz}$)

As expected, the microphones' different axial positions result in different autospectral content for IP transverse impacts. The acoustic autospectral content for transverse impacts is clearly much more reliant on microphone axial location than for axial impacts, as evidenced by the different autospectral amplitudes at multiple frequencies. One such difference in autospectral magnitude can be seen near 150 Hz, where there is a clear peak in Electret 1 and a local minimum in Electret 2. Despite different frequency content in each microphone, they both show clear separation in autospectral amplitude for different impacts. Importantly, there are some distinct differences between the axial and transverse impacts when comparing the same sensor. For example, for Electret 1, transverse impacts result in resonances at 124 Hz that is not very prominent for axial impacts. Conversely, the resonance seen at 160 Hz for axial impacts is not prominent for transverse impacts. This difference in response is important as the acoustic autospectral magnitude at these frequencies could potentially be used to indicate the orientation of the impact. An approach is discussed later in Section 5.2 that could potentially allow for determination of an impact's orientation in which both axial and transverse force components are present, which would be better representative of true conditions for biomechanical loading. The accelerometer's vibration response is shown in Figure 44 for comparison to the acoustic autospectra in the above figures.

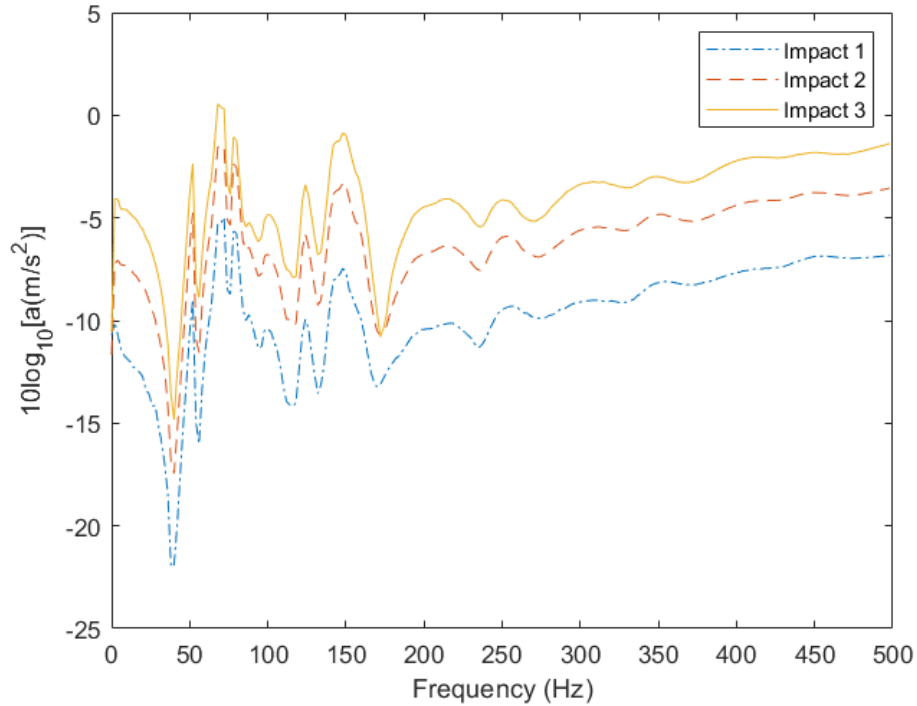


Figure 44. Vibration response of accelerometer signal for three IP transverse impacts ($f \leq 500\text{Hz}$)

The accelerometer's frequency content most closely resembles that of Electret 1, even though the accelerometer is located at the bar's end nearer to Electret 2. As previously mentioned, this is due to different modal content based on sensor location. Due to the similarity in frequency content of Electret 1 and the accelerometer, it is likely that these resonances are due to bending modes. The resonances in Electret 2 are not as easily categorized by comparison to the accelerometer. Again, the categorization of these modes is not a focus of the current study, but future work could aim to do so with a larger microphone array.

4.2.1 IP Transverse Impact Regression Models

Least squares regression models were fit for transverse impacts through the same methods outlined for axial impacts in Section 4.1.1. The acoustic frequency-domain

characteristics were correlated to impact force time-domain characteristics through least squares regressions with linear and quadratic models. The model criteria for the regression models associated with the microphones and accelerometers are presented below. Model criteria for the hammer’s self-correlation can be found in Appendix A2 and are not shown here since they are similar to results previously discussed in Section 4.1.

4.2.2 Autospectral Amplitude as a Function of Peak Force

The model criteria for models where autospectral amplitude is treated as a function of peak impact force are shown below in Table 18 through Table 20 for the microphones and accelerometer. Similar to the methodology outlined for axial impacts, discrete frequencies were targeted as resonances seen in the microphones’ and accelerometer’s frequency responses shown earlier in Figure 42 through Figure 44. Except for the 150 and 160 Hz frequencies, each of the frequencies listed in the following tables was present in all sensors, with variations in magnitude. The 150 Hz signal was not prominent for Electret 1 or the Accelerometer and the 160 Hz signal was not prominent in Electret 2 due to differences in sensor axial location. This behavior is reflected in the frequencies chosen for each of the sensors.

Table 18. Transverse IP Impact Model Criteria for Electret 1: Acoustic Autospectral Amplitude vs. Peak Force

Frequency (Hz)	Linear Model			Quadratic Model		
	R ² _{adj}	AIC	BIC	R ² _{adj}	AIC	BIC
54	0.9370	75.80	77.94	0.9340	64.80	69.06
72	0.8747	51.34	53.52	0.9140	-2.945	1.373
80	0.8696	98.72	100.9	0.8777	74.07	78.39
100	0.8846	-157.1	-154.9	0.8611	-163.4	-159.1
124	0.9220	-38.66	-36.52	0.9368	-68.00	-63.72
150	0.9298	-17.14	-15.00	0.9191	-32.83	-28.55
212	0.8945	-156.5	-154.3	0.9023	-201.3	-197.0

Table 19. Transverse IP Impact Model Criteria for Electret 2: Acoustic Autospectral Amplitude vs. Peak Impact

Frequency (Hz)	Linear Model			Quadratic Model		
	R^2_{adj}	AIC	BIC	R^2_{adj}	AIC	BIC
54	0.9097	156.1	158.2	0.9120	140.8	145.1
72	0.8720	79.74	81.90	0.9205	20.17	24.51
80	0.8590	18.19	20.36	0.8943	-23.24	-18.95
100	0.8549	-40.89	-38.73	0.9159	-112.4	-108.1
124	0.9057	-176.7	-174.6	0.8999	-177.1	-172.8
160	0.8848	-84.99	-82.85	0.9254	-151.4	-147.0
212	0.7338	-113.1	-111.0	0.8617	-211.0	-206.7

Table 20. Transverse IP Impact Model Criteria for Accelerometer: Acoustic Autospectral Amplitude vs. Peak Impact

Frequency (Hz)	Linear Model			Quadratic Model		
	R^2_{adj}	AIC	BIC	R^2_{adj}	AIC	BIC
54	0.9409	-170.5	-168.4	0.9217	-173.6	-169.3
72	0.9295	-65.28	-63.12	0.9368	-88.72	-84.40
80	0.8793	-57.44	-55.27	0.8896	-81.27	-76.95
100	0.9378	-231.0	-228.9	0.9356	-243.7	-239.4
124	0.9394	-202.6	-200.4	0.9280	-214.0	-209.7
150	0.9399	-129.2	-127.1	0.9274	-139.2	-134.9
212	0.9290	-208.4	-206.2	0.9215	-226.7	-222.5

Treating autospectral amplitude as a function of the peak force yields a high correlation, with R^2_{adj} values for linear models near 0.9. For both sensors, quadratic models generally appear to be superior to linear ones based on all model criteria when treating acoustic autospectral amplitude as a function of the peak force. Electret 1 consistently has higher correlations at resonant frequencies to the peak force than Electret 2, again showing the importance of sensor placement. Notably, Electret 2's response is much more correlated with peak force for transverse impacts than for axial ones. This is expected since the bending modes are more easily excited and would not be attenuated in the same manner that axial modes are, where damping would

cause a smaller response at a further distance from the source of impact. The lack of damping of bending modes due to larger measurement distance from the impact is supported by high correlations in vibration autospectral magnitude of the accelerometer to the peak force, which is the furthest sensor from the impact.

4.2.3 Energy in a Frequency Band as a Function of Peak Force

The correlation between energy in a band with peak impact force was considered for transverse impacts through the same methods previously discussed in Section 4.1 for axial impacts. The same three energy bands were targeted in which all bands begin at 50 Hz and increase in bandwidth, with upper band frequencies of 200, 500, and 1200 Hz, corresponding to a 150, 450, and 1150 Hz bandwidth, respectively. Table 21 through Table 23 summarize the model criteria for band energy as a function of peak force for the microphones and accelerometer.

Table 21. Transverse IP Impact Model Criteria for Electret 1: Acoustic Frequency Band Energy vs. Peak Impact Force

Frequency Band (Hz)	Linear Model			Quadratic Model		
	R^2_{adj}	AIC	BIC	R^2_{adj}	AIC	BIC
50 - 200	0.9343	-67.98	-65.83	0.9226	-72.90	-68.55
50 - 500	0.9327	-132.1	-130.0	0.9214	-140.2	-135.8
50 - 1200	0.9327	-190.5	-188.3	0.9214	-200.3	-196.0

Table 22. Transverse IP Impact Model Criteria for Electret 2: Acoustic Frequency Band Energy vs. Peak Impact Force

Frequency Band (Hz)	Linear Model			Quadratic Model		
	R ² _{adj}	AIC	BIC	R ² _{adj}	AIC	BIC
50 - 200	0.8988	-39.39	-37.24	0.9390	-98.18	-93.83
50 - 500	0.8960	-104.3	-102.1	0.9385	-166.2	-161.9
50 - 1200	0.8957	-161.8	-159.7	0.9391	-225.7	-221.4

Table 23. Transverse IP Impact Model Criteria for Accelerometer: Frequency Band Energy vs. Peak Impact Force

Frequency Band (Hz)	Linear Model			Quadratic Model		
	R ² _{adj}	AIC	BIC	R ² _{adj}	AIC	BIC
50 - 200	0.9355	-191.6	-189.5	0.9434	-212.5	-208.2
50 - 500	0.9113	-159.6	-157.4	0.9120	-180.0	-175.6
50 - 1200	0.9451	-143.5	-141.4	0.9393	-158.4	-154.1

Overall, for IP transverse impacts, the energy in a band is similarly correlated to the peak force when compared to the case where autospectral amplitude is the independent variable. For both microphones, the energy in the targeted bandwidths appears to be a reliable metric for predicting the peak force of the impact. One key difference between the microphones' model criteria is that a quadratic fit appears to be better for Electret 2, but not necessarily for Electret 1. For both Electret 1 and the accelerometer, the R²_{adj} values do not indicate that a quadratic model would be better than a linear one. It is not surprising that the model criteria for Electret 1 and the accelerometer would lead to similar conclusions based on comparison of their frequency response (Figure 42 and Figure 44), as previously discussed. As was the case with axial impacts, for all frequency bands considered, there is no benefit to increasing the bandwidth beyond the lowest bandwidth considered of 150 Hz. This is not surprising since most of the measurable resonances appear in the 50–200 Hz frequency band. Though it appears that the peak force can

be reasonably predicted based on acoustic measurements for transverse impacts, the next section considers how the acoustic measurements correlate to the primary impulse.

4.2.4 Autospectral Amplitude as a Function of Primary Impulse

The correlation of autospectral amplitude as a function of the primary impulse, previously defined for transverse impacts in Figure 40, is considered in this section in order to determine how well the primary impulse can be characterized based on acoustic measurements. Table 24 through Table 26 summarize the model criteria for the microphones and accelerometer for regression models where autospectral amplitude is treated as a function of the primary impulse.

Table 24. Transverse IP Impact Model Criteria for Electret 1: Acoustic Autospectral Amplitude vs. Primary Impulse

Frequency (Hz)	Linear Model			Quadratic Model		
	R^2_{adj}	AIC	BIC	R^2_{adj}	AIC	BIC
54	0.9396	43.33	45.49	0.9803	-1.653	2.665
72	0.9619	-58.40	-56.26	0.9488	-40.91	-36.59
80	0.8897	62.02	64.17	0.8728	75.77	80.12
100	0.8748	-173.3	-171.2	0.8789	-192.8	-188.5
124	0.9835	-164.2	-162.1	0.9835	-165.9	-161.6
150	0.9856	-143.5	-141.3	0.9872	-149.9	-145.6
212	0.9843	-307.4	-305.2	0.9878	-339.7	-335.4

Table 25. Transverse IP Impact Model Criteria for Electret 2: Acoustic Autospectral Amplitude vs. Primary Impulse

Frequency (Hz)	Linear Model			Quadratic Model		
	R^2_{adj}	AIC	BIC	R^2_{adj}	AIC	BIC
54	0.9770	45.96	48.12	0.9747	51.22	55.57
72	0.9210	21.68	23.84	0.9260	-0.282	4.036
80	0.8629	-5.243	-3.069	0.8529	-4.516	-0.167
100	0.9538	-152.0	-149.8	0.9770	-204.5	-200.2
124	0.9374	-232.2	-230.1	0.9586	-233.2	-228.9
160	0.9761	-212.3	-210.2	0.9708	-212.4	-208.1
212	0.8774	-197.8	-195.7	0.8932	-242.1	-237.8

Table 26. Transverse IP Impact Model Criteria for Accelerometer: Autospectral Amplitude vs. Primary Impulse

Frequency (Hz)	Linear Model			Quadratic Model		
	R^2_{adj}	AIC	BIC	R^2_{adj}	AIC	BIC
54	0.9807	-267.2	-265.0	0.9861	-281.6	-277.3
72	0.9777	-160.3	-158.2	0.9777	-158.5	-154.2
80	0.8912	-86.20	-84.02	0.8872	-84.35	-80.00
100	0.9803	-331.2	-329.1	0.9798	-329.8	-325.5
124	0.9850	-318.5	-316.4	0.9870	-323.2	-318.8
160	0.9848	-243.2	-241.1	0.9881	-253.2	-248.8
212	0.9835	-237.7	-235.5	0.9871	-247.7	-243.4

Overall, there appears to be a high level of correlation between the targeted acoustic autospectral amplitudes and the primary impulse of IP transverse impacts. There is minimal advantage to choosing a quadratic model over a linear one based on R^2_{adj} values, though AIC and BIC values indicate a preference toward quadratic modelling. Despite this disagreement among model criteria, it is clear that the correlation between autospectral amplitude and the primary impulse is strong.

4.2.5 Energy in a Frequency Band as a Function of Primary Impulse

The final set of regression models considers acoustic energy in a frequency band treated as a function of the primary impulse when the impact occurs in-plane with the microphones.

Table 27 through Table 29 summarize the model criteria for this case for the microphones and accelerometer.

Table 27. Transverse IP Impact Model Criteria for Electret 1: Acoustic Frequency Band Energy vs. Primary Impulse

Frequency Band (Hz)	Linear Model			Quadratic Model		
	R^2_{adj}	AIC	BIC	R^2_{adj}	AIC	BIC
50 - 200	0.9927	-229.4	-227.3	0.9925	-227.4	-223.1
50 - 500	0.9931	-300.3	-298.1	0.9930	-298.6	-294.3
50 - 1200	0.9932	-360.2	-358.0	0.9930	-358.5	-354.1

Table 28. Transverse IP Impact Model Criteria for Electret 2: Acoustic Frequency Band Energy vs. Primary Impulse

Frequency Band (Hz)	Linear Model			Quadratic Model		
	R^2_{adj}	AIC	BIC	R^2_{adj}	AIC	BIC
50 - 200	0.9802	-177.8	-175.6	0.9858	-200.9	-196.6
50 - 500	0.9799	-242.6	-240.5	0.9865	-272.3	-268.0
50 - 1200	0.9796	-298.4	-296.3	0.9864	-329.6	-325.3

Table 29. Transverse IP Impact Model Criteria for Accelerometer: Frequency Band Energy vs. Primary Impulse

Frequency Band (Hz)	Linear Model			Quadratic Model		
	R^2_{adj}	AIC	BIC	R^2_{adj}	AIC	BIC
50 - 200	0.9873	-316.9	-314.7	0.9870	-315.0	-310.7
50 - 500	0.9863	-307.2	-305.0	0.9879	-318.9	-314.5
50 - 1200	0.9939	-304.6	-302.5	0.9956	-321.0	-316.8

Clearly there is a strong correlation between acoustic autospectral amplitudes and the primary impulse. Only Electret 2 benefits from utilizing quadratic modelling, reflecting similar results from Section 4.2.3, where energy in a frequency band was treated as a function of the peak impact. Electret 1's model criteria shown in Table 27 are the first to indicate that acoustic measurements may be as good of a predictor of an impact characteristic as acceleration measurements of the internal bar. As was the case for previous regression models that utilized energy in a frequency band as the dependent variable, there is no benefit to increasing the bandwidth considered for either microphone.

4.2.6 Transverse IP Impact Results Summary

The measured acoustic frequencies are generally more correlated to impact characteristics for transverse impacts (with IP sensors) than for axial impacts. When compared to results for axial impacts, the ability to characterize transverse impact force in the time-domain is less dependent on sensor location, though it is still preferable to have the microphone placed at a central axial position (Electret 1) than at one distal from the point of impact (Electret 2). Furthermore, there are still differences in which modes are prominent in the measured signal based on each microphone's axial position. The peak impact force appears to be just as predictable for IP transverse impacts in these tests as for axial impacts despite the transverse impact's time-domain being less easily approximated by a single peak value and occurring over a longer amount of time ($\Delta t \approx 0.76$ ms for axial impacts compared to $\Delta t \approx 1.6$ ms for transverse impacts). Though the peak force may be correlated to the acoustic measurements, there are issues with knowing when the force occurred during the impact due to the more unpredictable nature of a transverse impact's signal in the time-domain and unpredictability in this behavior. Despite

these potential issues with estimating the peak force from acoustic measurements, the primary impulse appears to be highly predictable. This is especially true when considering the acoustic energy in a band, where the microphone located at the central axial position (Electret 1) performed as well as the accelerometer placed directly on the bar.

It is worth mentioning that these results are for the ideal case in which the microphones are in-plane with the impact direction. This configuration was expected to yield the largest system response, so it is not unexpected that measurements were able to be highly correlated to impact characteristics. The next section investigates how a change in radial location of the microphones might affect the acoustic autospectral correlations to the impact characteristics for transverse impacts

4.3 Transverse Impact with Out-of-plane Measurements

The third and final set of studies is very similar to the previous one discussed in Section 4.2, where the bar is excited by a transverse impact. The difference here is that the acoustic sensors are placed out-of-plane (OOP) with respect to the direction of the applied transverse impact (see Figure 27). Again, before discussing the regression models where acoustic autospectral characteristics are correlated with impact time-domain characteristics, some sample data are shown. Time-domain data for the impact hammer is shown below in Figure 45. While the impact's time-domain looks very similar to that shown previously for IP transverse impacts, it is shown here for context with sensor data for each sample impact. Electret 1's acoustic time-domain response to these impacts is shown in Figure 46.

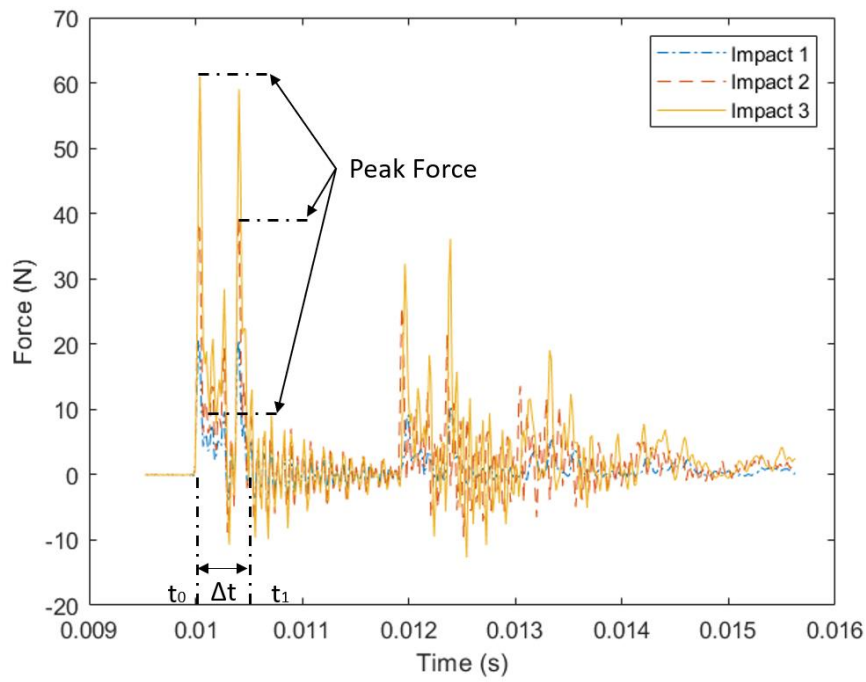


Figure 45. Sample time data of impact hammer for three transverse impacts with OOP measurements with labeled peaks and impulse times

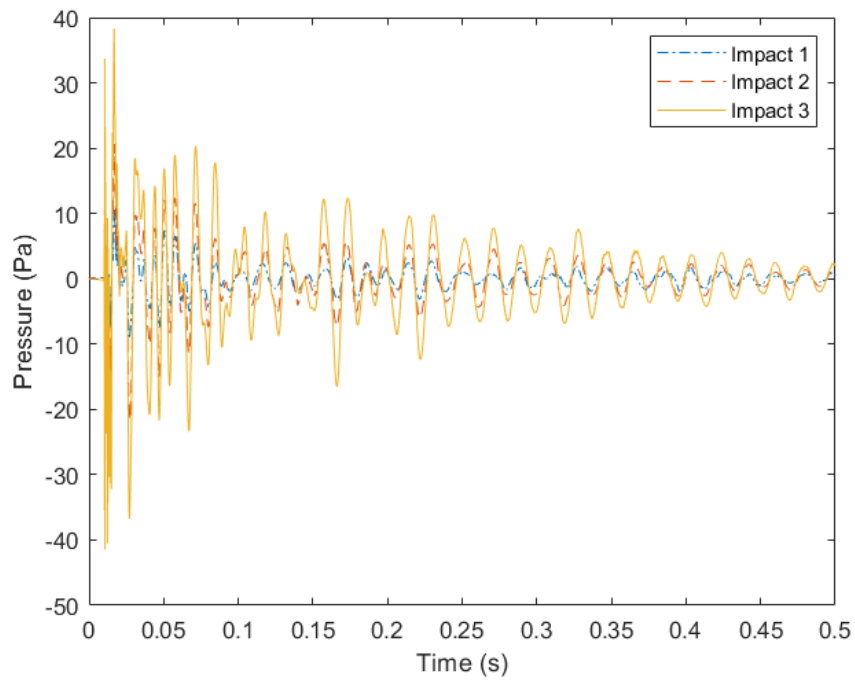


Figure 46. Sample time data of Electret 1 for three OOP transverse impacts

As previously mentioned, the hammer's time-domain characteristics are essentially unchanged from the previously discussed IP transverse impacts; the peak force occurs at one of the first coupled peaks and the primary impulse occurs during time $\Delta t \approx 1.6$ ms. While the time-domain response for Electret 1 is similar for both cases of transverse impacts, the response magnitude is clearly lower for OOP impacts. The autospectra for the microphones confirm this, shown below in Figure 47 and Figure 48.

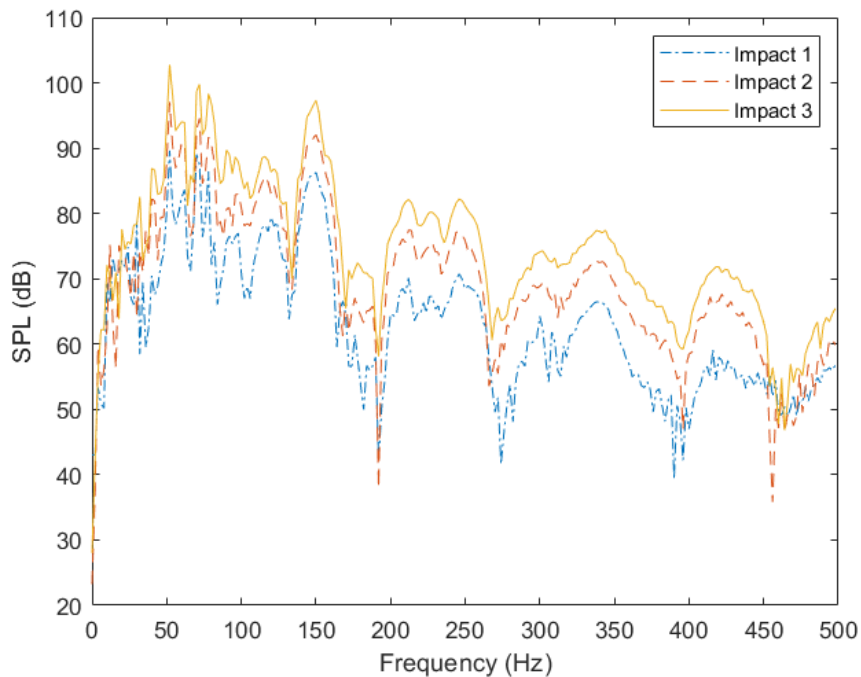


Figure 47. Autospectrum (dB) of Electret 1 signal for three OOP transverse impacts ($f \leq 500\text{Hz}$)

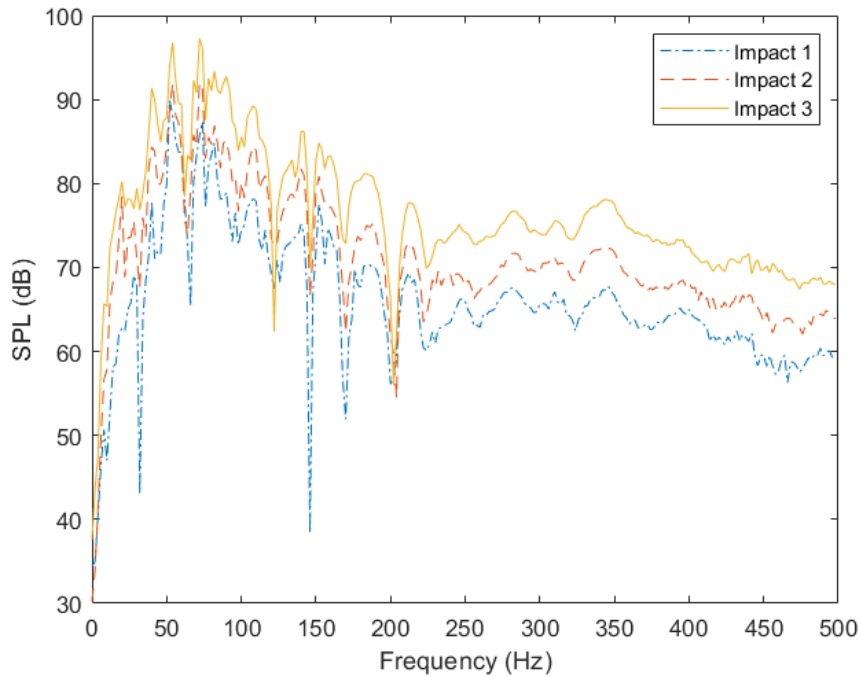


Figure 48. Autospectrum (dB) of Electret 2 signal for three OOP transverse impacts ($f \leq 500\text{Hz}$)

Prior to considering the correlations, it is useful to compare the acoustic autospectra for Electret 1 and 2 for OOP transverse impacts shown in Figure 47 and Figure 48 with the corresponding autospectra shown previously in Figure 42 and Figure 43 for IP transverse impacts. While the frequency-domain of the microphones looks similar for both OOP and IP transverse impacts, the measured resonances are less prominent for OOP impacts. Nevertheless, it is still possible to distinguish the resonant peaks from surrounding frequencies. This is not unexpected as bending modes occur in orthogonal pairs, as shown previously in Figure 26, for the bare aluminum bar (without the surrounding gel). The performance of the microphones relative to the accelerometer for OOP impacts is also worth considering. The accelerometer's vibration response is shown below in Figure 49.

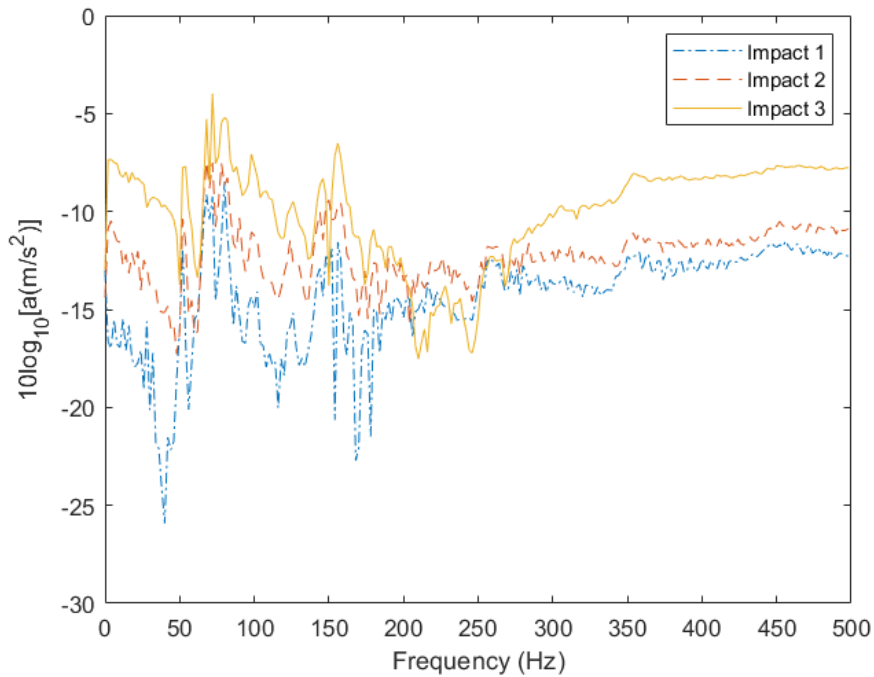


Figure 49. Vibration response of accelerometer signal for three OOP transverse impacts ($f \leq 500\text{Hz}$)

The accelerometer's frequency response to OOP impacts is much lower in magnitude at all frequencies than that of IP impacts. Again, resonant peaks are less prominent in relation to surrounding frequencies. Furthermore, when compared to the acoustic autospectra, there is not very good separation between the vibration responses for each impact. For example, there is overlap between the vibration autospectra around 200 Hz, but there is still clear separation in the acoustic autospectra for both microphones. The implications of this are that it may be beneficial to utilize acoustic measurements for the case at hand, but it may be difficult to apply the method when the impact direction is unknown *a priori*. This is discussed later in Section 5.2 when considering future work. Regression models for the sensors are now discussed in a manner consistent with the previous tests.

4.3.1 OOP Transverse Impact Regression Models

Regression models were fit for transverse impacts through the same methods as previous impacts. These regression models use the same dependent variables as for the IP transverse impacts, which allows for a direct comparison with the results given back in Section 4.3. Because the same processing is used here, the reader is referred back to previous sections for more details on the processing methods and modeling approaches. Model criteria for the hammer's self-correlation is given in Appendix A3.

4.3.2 Autospectral Amplitude as a Function of Peak Force

The model criteria for regression models in which acoustic autospectral amplitude is treated as a function of peak force for a transverse impact with OOP measurements are shown in Table 30 through Table 32.

Table 30. Transverse OOP Impact Model Criteria for Electret 1: Acoustic Autospectral Amplitude vs. Peak Force

Frequency (Hz)	Linear Model			Quadratic Model		
	R^2_{adj}	AIC	BIC	R^2_{adj}	AIC	BIC
54	0.8785	-42.05	-39.97	0.8849	-41.04	-36.89
72	0.9046	-89.59	-87.51	0.8988	-90.05	-85.90
80	0.7335	-41.94	-39.86	0.7104	-40.98	-36.82
100	0.8014	-190.95	-188.87	0.7956	-189.0	-184.8
124	0.7556	-149.39	-147.31	0.7547	-175.2	-171.0
150	0.8987	-112.08	-110.02	0.8792	-106.9	-102.7
212	0.5544	-195.41	-193.32	0.4821	-198.2	-194.0

Table 31. Transverse OOP Impact Model Criteria for Electret 2: Acoustic Autospectral Amplitude vs. Peak Impact

Frequency (Hz)	Linear Model			Quadratic Model		
	R^2_{adj}	AIC	BIC	R^2_{adj}	AIC	BIC
54	0.6085	5.624	7.718	0.5477	3.626	7.815
72	0.7743	-65.81	-63.73	0.7536	-65.37	-61.21
80	0.6140	-87.66	-85.56	0.5904	-85.95	-81.76
100	0.6288	-156.6	-154.5	0.5845	-165.9	-161.8
124	0.7686	-237.7	-235.6	0.7741	-236.0	-231.8
160	0.7349	-229.8	-227.7	0.7308	-227.8	-223.7
212	0.4868	-236.1	-234.0	0.4828	-234.1	-229.9

Table 32. Transverse OOP Impact Model Criteria for Accelerometer: Acoustic Autospectral Amplitude vs. Peak Impact Force

Frequency (Hz)	Linear Model			Quadratic Model		
	R^2_{adj}	AIC	BIC	R^2_{adj}	AIC	BIC
54	0.6662	-278.3	-276.3	0.6669	-276.4	-272.2
72	0.6514	-229.0	-226.9	0.7033	-220.5	-216.3
80	0.6918	-231.9	-229.8	0.6682	-230.6	-226.4
100	0.7329	-342.1	-340.0	0.7771	-324.9	-320.7
124	0.5890	-332.2	-330.1	0.6421	-334.4	-330.2
150	0.7720	-295.1	-293.0	0.7485	-295.3	-291.2
212	0.3356	-272.5	-270.4	0.2008	-285.2	-281.0

Clearly there is reduced capability of characterizing transverse impact forces when the acoustic sensors are out-of-plane with respect to the impact direction. Comparing the current model criteria tables associated with OOP impacts with those for IP impacts (see Section 4.2.3), R^2_{adj} values are much lower at all frequencies for OOP impacts. Few of the targeted frequencies provide high enough R^2_{adj} values for Electret 1's regression models to be very useful in characterizing the peak impact force. None of the frequencies show strong correlations for Electret 2 or the accelerometer. Again, the central axial location of Electret 1 provides better correlations to the peak impact force.

4.3.3 Energy in a Frequency Band as a Function of Peak Force

The model criteria for regression models in which the energy in a frequency band is treated as a function of the peak OOP transverse impact force are shown below in Table 33 through Table 35.

Table 33. Transverse OOP Impact Model Criteria for Electret 1: Acoustic Frequency Band Energy vs. Peak Impact Force

Frequency Band (Hz)	Linear Model			Quadratic Model		
	R^2_{adj}	AIC	BIC	R^2_{adj}	AIC	BIC
50 - 200	0.8943	-186.9	-184.8	0.8874	-188.7	-184.6
50 - 500	0.8888	-245.3	-243.3	0.8814	-247.4	-243.3
50 - 1200	0.8888	-299.9	-297.8	0.8814	-302.1	-298.0

Table 34. Transverse OOP Impact Model Criteria for Electret 2: Acoustic Frequency Band Energy vs. Peak Impact Force

Frequency Band (Hz)	Linear Model			Quadratic Model		
	R^2_{adj}	AIC	BIC	R^2_{adj}	AIC	BIC
50 - 200	0.7933	-187.7	-185.6	0.7734	-187.8	-183.7
50 - 500	0.7962	-249.7	-247.6	0.7764	-249.9	-245.8
50 - 1200	0.8061	-307.2	-305.1	0.7868	-307.9	-303.7

Table 35. Transverse OOP Impact Model Criteria for Accelerometer: Frequency Band Energy vs. Peak Impact Force

Frequency Band (Hz)	Linear Model			Quadratic Model		
	R^2_{adj}	AIC	BIC	R^2_{adj}	AIC	BIC
50 - 200	0.7929	-356.1	-354.0	0.7833	-354.2	-350.1
50 - 500	0.5304	-282.8	-280.7	0.4903	-281.4	-277.3
50 - 1200	0.4272	-231.0	-228.9	0.3839	-229.4	-225.3

Again, the correlation between band energy and peak impact forces is lower for OOP impacts than for IP ones. Electret 1 still shows a reasonably good correlation, with an R^2_{adj} value

of about 0.89 for linear regression models. Electret 2 and the accelerometer do not seem to be able to reliably characterize the peak impact force by using the chosen bands. These results are not unexpected based on those shown for autospectral amplitudes as a function of peak impact force.

4.3.4 Autospectral Amplitude as a Function of Primary Impulse

Though the peak force was not necessarily characterized well by acoustic measurements for OOP impacts, this section and the following one consider how correlated acoustic measurements are with the primary impulse. Table 36 through Table 38 contain the model criteria for the microphones and accelerometer in which autospectral amplitude is considered as a function of the primary impulse.

Table 36. Transverse OOP Impact Model Criteria for Electret 1: Acoustic Autospectral Amplitude vs. Primary Impulse

Frequency (Hz)	Linear Model			Quadratic Model		
	R ² _{adj}	AIC	BIC	R ² _{adj}	AIC	BIC
54	0.8798	-75.47	-73.39	0.9405	-86.55	-82.36
72	0.9231	-120.5	-118.4	0.9570	-142.8	-138.7
80	0.7437	-62.06	-60.00	0.7766	-62.38	-58.26
100	0.8011	-208.2	-206.1	0.8484	-213.2	-209.0
124	0.8159	-186.0	-183.9	0.7963	-193.3	-189.1
150	0.9200	-145.3	-143.2	0.9285	-146.2	-142.0
212	0.5980	-219.8	-217.8	0.6047	-218.0	-213.8

Table 37. Transverse OOP Impact Model Criteria for Electret 2: Acoustic Autospectral Amplitude vs. Primary Impulse

Frequency (Hz)	Linear Model			Quadratic Model		
	R^2_{adj}	AIC	BIC	R^2_{adj}	AIC	BIC
54	0.5704	-3.468	-1.373	0.5200	-2.855	1.333
72	0.7577	-77.53	-75.43	0.8174	-86.96	-82.80
80	0.5737	-95.34	-93.24	0.6023	-94.08	-89.90
100	0.6665	-187.9	-185.8	0.6487	-186.1	-181.9
124	0.6845	-230.8	-228.7	0.7528	-234.1	-229.9
160	0.6811	-236.6	-234.5	0.6940	-229.8	-225.7
212	0.4211	-244.1	-242.0	0.3927	-242.2	-238.0

Table 38. Transverse OOP Impact Model Criteria for Accelerometer: Autospectral Amplitude vs. Primary Impulse

Frequency (Hz)	Linear Model			Quadratic Model		
	R^2_{adj}	AIC	BIC	R^2_{adj}	AIC	BIC
54	0.5615	-274.0	-271.9	0.5766	-267.6	-263.4
72	0.5829	-232.1	-230.1	0.6908	-223.9	-219.7
80	0.6864	-247.6	-245.5	0.7099	-246.5	-242.3
100	0.7114	-354.9	-352.8	0.8273	-344.5	-340.4
124	0.5366	-337.5	-335.4	0.6406	-341.7	-337.5
160	0.6225	-274.3	-272.2	0.5739	-274.3	-270.1
212	0.7457	-305.0	-302.9	0.7559	-303.4	-299.2

The model criteria for regression models that relate autospectral amplitude with the primary impulse indicate that the primary impulse is not characterized as well as for OOP impacts as those shown previously for IP impacts in Section 4.2.3. The acoustic autospectral amplitudes are still more correlated to the primary impulse than to the peak force, but only measurements from Electret 1 are well correlated.

4.3.5 Energy in a Frequency Band as a Function of Primary Impulse

The final set of regression models for OOP impacts treat the energy in a frequency band as a function of the primary impulse and are shown in Table 39 through Table 41 for the microphones and accelerometer.

Table 39. Transverse OOP Impact Model Criteria for Electret 1: Acoustic Frequency Band Energy vs. Primary Impulse

Frequency Band (Hz)	Linear Model			Quadratic Model		
	R ² _{adj}	AIC	BIC	R ² _{adj}	AIC	BIC
50 - 200	0.9378	-233.6	-231.6	0.9544	-243.0	-238.9
50 - 500	0.9347	-291.4	-289.3	0.9509	-299.4	-295.3
50 - 1200	0.9358	-346.1	-344.1	0.9515	-354.0	-349.9

Table 40. Transverse OOP Impact Model Criteria for Electret 2: Acoustic Frequency Band Energy vs. Primary Impulse

Frequency Band (Hz)	Linear Model			Quadratic Model		
	R ² _{adj}	AIC	BIC	R ² _{adj}	AIC	BIC
50 - 200	0.7905	-205.0	-202.9	0.7935	-203.2	-199.0
50 - 500	0.7954	-267.7	-265.6	0.7979	-265.8	-261.6
50 - 1200	0.8140	-328.5	-326.4	0.8155	-326.6	-322.4

Table 41. Transverse OOP Impact Model Criteria for Accelerometer Acoustic Frequency Band Energy vs. Primary Impulse

Frequency Band (Hz)	Linear Model			Quadratic Model		
	R ² _{adj}	AIC	BIC	R ² _{adj}	AIC	BIC
50 - 200	0.7791	-369.4	-367.3	0.8078	-370.0	-365.8
50 - 500	0.4843	-290.0	-287.9	0.4685	-288.0	-283.8
50 - 1200	0.3649	-234.0	-231.9	0.3289	-232.2	-228.0

Electret 1 appears to be able to reasonably characterize the primary impulse by considering the energy present in the chosen frequency bands. For Electret 1, all model criteria

indicate that quadratic models are preferable to linear ones. There is a moderate correlation between Electret 2's band energy and the primary impulse, though still not high enough to be able to reasonably infer the impulse. The accelerometer's model criteria show that higher frequencies ($f > 200$ Hz) are not correlated with the primary impulse for OOP transverse impacts, suggesting that higher frequency bending modes in the orthogonal direction to the impact are not easily excited or are otherwise heavily damped. Considering this and the frequency components discussed back in Section 4.2, this damping may help provide additional information that is useful for inferring the direction of the force.

4.3.6 Transverse OOP Impact Results Summary

Overall, transverse impacts with OOP measurements are not as well characterized by the acoustic autospectra as for IP impacts. Only Electret 1 was able to be reasonably correlated with either the peak impact force or the primary impulse, but the R^2_{adj} values for Electret 1 were much lower for OOP than for IP impacts. As was the case for IP impacts, the primary impulse was better characterized by the acoustic autospectra than was the peak force.

CHAPTER 5. CONCLUSIONS AND RECOMMENDATIONS

The measurement technique investigated in this study is motivated by the desire to develop a new non-invasive method of inferring internal forces transferred between bones during biomechanical motion. The traditional method of inferring forces is cumbersome due to the number of sensors required and is typically limited to being performed in a laboratory environment. Furthermore, the inverse-dynamic method is prone to error for various reasons, including unavoidable ones associated with the mathematical approach. The proposed method of utilizing microphones on the skin's surface as part of a novel inverse method of inferring internal forces could potentially alleviate both of these issues, allowing for measurements to be taken during regular activity (outside of a lab) and not being necessarily reliant on an iterative solving process to infer information about internal forces. The current work investigates the feasibility of utilizing microphones to infer information about internal forces through experimentation on a physical model of an aluminum bar coupled with a surrounding gelatin, approximating a femur and the surrounding soft tissues. The determination of feasibility is based on analysis of three sets of impact tests on the test structure where least squares regression models are used to determine the correlation between acoustic autospectral characteristics and time-domain impact characteristics. The types of impacts tested in the current work were representative of the elementary components of bone-on-bone forces that occur during biomechanical motion: axial and transverse. Real biomechanical forces are largely compressive in nature between bones,

represented by axial impacts in the current work. Other forces between bones, shear forces, were represented by transverse impacts during experimentation. For the case of transverse impacts, two microphone radial positions were considered: in-plane and orthogonally out-of-plane relative to the impact force direction.

Conclusions on the feasibility of the measurement technique are based on the previous results shown in Chapter 4. Results were previously summarized for each experimental setup (axial impact, IP transverse impact, and OOP transverse impacts) and some conclusions have been stated for each individual test. However, the conclusions provided here inter-relate the different tests' results and consider them as they apply to the measurement technique more holistically. Recommendations for future work follow the conclusions section.

5.1 Conclusions

Overall, acoustic measurements have been shown here to be feasible as a basis for inferring information about internal forces. However, current results are only directly applicable to inferring information for purely axial and transverse impacts. A large part of future work, discussed below in Section 5.2, will be to determine to what extent impact characteristics can still be inferred when the impact has both axial and transverse components.

Axial and Transverse impact characteristics which were able to be correlated with acoustic autospectra were the peak force magnitude and the primary impulse, as previously defined in Chapter 4. The acoustic frequency-domain characteristics considered were the autospectral magnitude of resonant frequencies and the acoustic energy in frequency bands. In general, the primary impulse was more highly correlated with acoustic autospectra than was the

peak force of the impact. The level of correlation of autospectral magnitude varied with which resonant frequency was chosen as the regression model's dependent variable. Some of the targeted frequencies were good indicators of either peak magnitude or the primary impulse, but the energy in a band was always a better indicator of the primary impulse. There was no benefit to increasing the bandwidth of the smallest frequency band considered, which was the 50 – 200 Hz band. This 150 Hz bandwidth was the narrowest considered and encompassed most of the region in which the resonant frequencies were observed. Although this band might seem narrow, it is actually a relatively wide band when considering the desire to distinguish between impact directions for real applications. Narrower frequency bands could be considered as a metric to distinguish between axial and transverse impacts in future work, if considering the same bar-gel structure or similar. The regression models in the current work do not consistently show that the frequency response of the system is as non-linear as was expected, with some models showing clear preference towards quadratic modelling while others show a preference toward linear modelling. With respect to future work, discussed below, it would be best to still consider both model types and determine their applicability to larger datasets through similar methods of analysis.

Differences in not only the modes present in the signal, but the degree to which frequency-domain acoustic data could be correlated to experimental impacts were highly dependent on acoustic sensor position. For both axial and transverse impacts, the microphone placed at the central axial location performed much better than the microphone placed distally from the impact location. The highest correlated autospectral information was measured by the microphone placed at a central axial location. It is indeterminate from the current work how much of this preference in microphone position is due to the difference in modal content of each

sensor or due to the increased effect that damping has on sensors which are distal from the point of impact. It is likely that both factors contribute, however, damping likely plays a larger factor in the importance of sensor proximity to the point of impact for axial impacts than for transverse ones. For transverse impacts, the level of autospectral correlation to impact characteristics was not dependent on the microphone's axial location, other than the difference in which resonant frequencies were prominent due to modal factors. However, the correlation of the acoustic autospectra for transverse impacts did vary based on sensor radial position relative to the impact. For IP transverse impacts, the acoustic autospectra were a strong predictor of impact characteristics in the time-domain, performing as well as the autospectra of the accelerometer. In general, IP transverse impacts were much more correlated with impact characteristics than were OOP transverse impacts. However, differences in autospectral content between IP and OOP transverse impacts may allow for inference of the direction of impact. Similarly, there were more significant differences in frequency content between axial and transverse impacts. A potential approach to using this information to infer impact direction is discussed in Section 5.2.

While this measurement technique has been shown to be feasible based on the ability to correlate autospectral characteristics with time-domain impact characteristics, the next section focuses on next steps that should be taken to improve and extend the current work.

5.2 Future Direction Recommendations

With the conclusions from the previous section, this section focuses on how future work can best apply and improve upon the measurement technique. Recommendations cover changes to the experimental setup, other metrics that may help to characterize the impact, and potential post-processing methods.

The most direct improvement to the testing methodology would be to automate impacts to reduce variance in the direction in which they are applied. The impacts applied in the current work are assumed to be purely axial or purely transverse, but there are possibly other force components present. Automation of impacts could be implemented by attaching a force transducer to an actuator. Impact automation would obviously allow for more consistency in impact direction, but it would also allow for better regression modelling by allowing for a broader distribution of impact magnitudes and increased sample size. With automation, the response for the system could be compared for the same magnitude impact applied in different orientations, allowing for more direct comparison of autospectral content when the direction of the impact is varied. Furthermore, impact automation would allow for multiple bar-gel samples to be tested since the dynamic behavior of each test sample could be verified by applying the same set of impacts under identical test conditions. Impact automation may also allow for more ideal transverse impacts where the paired peaks are no longer present. While it was shown in the current work that the peak force of transverse impacts could be inferred, there are still limitations to being able to characterize the impact when the resultant paired peaks' relative magnitudes vary.

The post-processing methods employed in the current work focused on the correlation of autospectral magnitudes and their sum across frequency bands to impact characteristics in the time-domain. As previously mentioned, a slight variation to the approach here may be to consider narrower frequency bands as a means of determining the nature of an impact's direction. Another metric not considered in the current work which may allow for better characterization of the impact is the kurtosis of resonant peaks. Kurtosis is a unitless parameter which describes the peakedness of a curve relative to a Gaussian normal distribution (Keller, J.

A.). While kurtosis is defined from the perspective of statistical analysis, it can characterize spectral data in digital signal processing. In the current application, it may be useful in distinguishing between axial and transverse impacts. For example, the resonant peaks in the axial tests in Section 4.1 are more sharply peaked than those seen for transverse impacts in Sections 4.2 and 4.3, and thus would be expected to have higher kurtosis values. Another method that was not considered in the current work is time-domain characterization of acoustic signals. Frequency-domain analysis was the focus of current work in order to identify potential nonlinearities in the system. The more non-linear a system is, the more necessary it will be to introduce time-domain techniques into post-processing.

As previously mentioned, the two types of impacts tested were representative of the basic constituents of bone-on-bone forces. A large part of future work will be to determine if the direction of an impact with both axial and transverse components can be determined from acoustic measurements. Without being able to infer the direction of an impact, its component magnitudes are indeterminate. Characterizing impacts with both axial and transverse components will require a larger microphone array than that of the current work. While it is uncertain what the minimum number of sensors required might be to allow for separation of impact components, it is suggested that the microphone array consist of no fewer than 9 microphones in a 3 by 3 array, as illustrated in Figure 50.

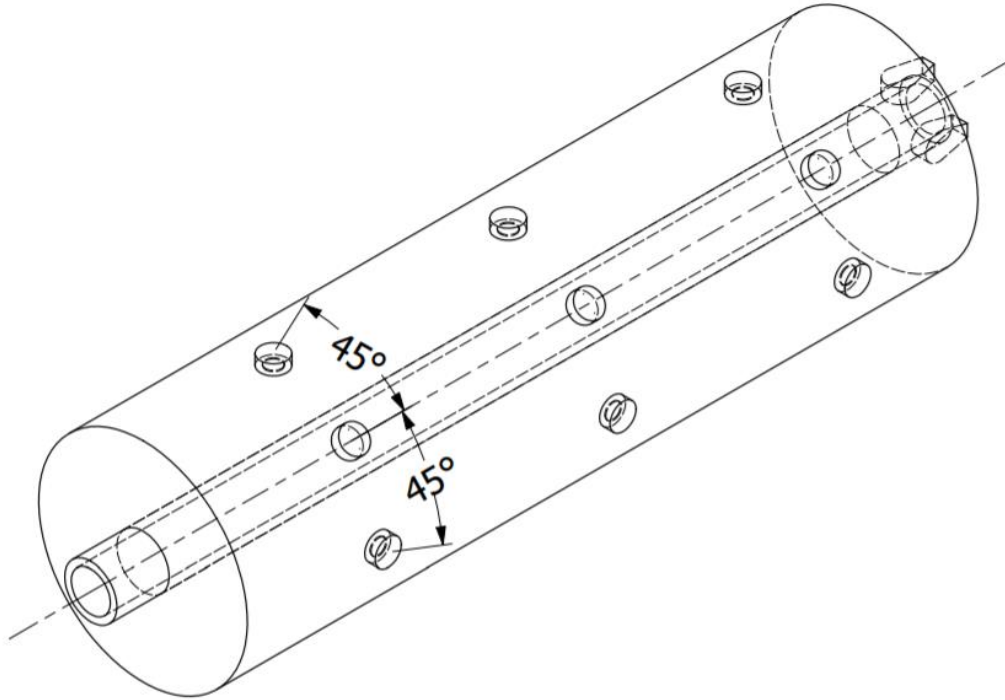


Figure 50. A 3 x 3 microphone array with would symmetrical axial placements and 45-degree radial offsets

The placement of the sensors would be such that three microphones would be placed symmetrically with respect to the central axial location and each set of three microphones would be at 45-degree radial offsets. The extension of the axial array from 2 microphones (in the current setup) to 3 will allow for better understanding of how the microphone's proximity to the impact effects the quality of measurements. The current work shows that placing a microphone at a central axial location is preferable to placing it at a location distal to the impact, but this is only a relative comparison and does not show that the central location is the most optimal one. It is likely that nearer proximity to the impact will provide for better correlation to axial impact time-domain characteristics due to less damping of the signal. Similarly, the difference in radial location will potentially allow for inference of transverse impact characteristics when the impact does not occur in-plane or orthogonally out-of-plane to sensors. The determination of axial and

transverse impact magnitude will likely rely on determining the greatest difference in autospectral content between axial and transverse components and targeting those discrete frequencies. In an ideal scenario, there would be an acoustic autospectral component which is unique to each impact type. However, there is overlap between frequencies present in each type of impact. This overlap is exacerbated by the flattened resonant peaks caused by high damping in the soft tissue/gelatin. This overlapping behavior may be able to be accounted for through more complex multivariable regression models in which frequency content could be weighted for its expected contribution to each impact type. Apart from inferring information about the magnitude of the impact, the primary impulse of the impact would also be desirable to characterize, as was done in the current work. If the impulses associated with individual axial and transverse components of any impact can be determined, then convolution techniques in the time-domain may allow for inference of the impact's total impulse.

Suggestions for future work up to this point include a larger number of impacts for each impact type, testing of many more impact directions, a larger sensor array, and multivariable modelling. Any of these suggestions leads to a much larger dataset, though the complexity of post-processing would also be greatly increased. Machine-learning techniques or a fully developed inverse acoustic model would likely need to be employed for such a large dataset. This is especially true for the necessity of utilizing multivariable regression models for mixed impacts measured by the larger sensor array. Supervised machine learning algorithms can be developed from training datasets, which could be larger sets similar to data gathered in this study, in order to predict impact characteristics. The inverse acoustic model would necessarily be quite complex due to the frequency-dependent nature of the material properties associated with soft tissue.

The current work was necessary to establish the feasibility of utilizing microphones to measure acoustic waveforms at the skin's surface as a part of a novel method to infer information about internal forces transferred between bones during biomechanical motion. While the conclusion can be made that the measurement technique itself is feasible, future work will need to increase the complexity of the experimental methods applied here as the next steps to developing a novel inverse method to inferring internal forces during biomechanical motion.

REFERENCES

- Ackerman, M. J. (2019, July 8). The Visible Human Project - Getting the Data. Retrieved from https://www.nlm.nih.gov/research/visible/getting_data.html
- Black, T. K. (1978). A new method for assessing the sex of fragmentary skeletal remains: Femoral shaft circumference. *American Journal of Physical Anthropology*, 48(2), 227–231. doi: 10.1002/ajpa.1330480217
- Campoli, G., Baka, N., Kaptein, B., Valstar, E., Zachow, S., Weinans, H., & Zadpoor, A. (2014). Relationship between the shape and density distribution of the femur and its natural frequencies of vibration. *Journal of Biomechanics*, 47(13), 3334–3343. doi: 10.1016/j.jbiomech.2014.08.008
- Caresta, M. (2009, June 3). Vibrations of a Free-Free Beam - University of New South Wales. Retrieved from http://www.varg.unsw.edu.au/Assets/link_pdfs/Beam_vibration.pdf
- Chen, H., Zhao, X., Lu, X., & Kassab, G. (2013). Non-linear micromechanics of soft tissues. *International Journal of Non-Linear Mechanics*, 56, 79–85. doi: 10.1016/j.ijnonlinmec.2013.03.002
- Control Systems. (2017). Retrieved from https://en.wikibooks.org/wiki/Control_Systems/Print_version
- Dąbrowska, A. K., Rotaru, G.-M., Derler, S., Spano, F., Camenzind, M., Annaheim, S., ... Rossi, R. M. (2015). Materials used to simulate physical properties of human skin. *Skin Research and Technology*, 22(1), 3–14. doi: 10.1111/srt.12235
- Dourmashkin, P. A. (2014). *Classical mechanics: Mit 8.01 course notes*. Hoboken, NJ: Wiley Custom Learning Solutions.
- Farrer, A. I., Odéen, H., Bever, J. D., Coats, B., Parker, D. L., Payne, A., & Christensen, D. A. (2015). Characterization and evaluation of tissue-mimicking gelatin phantoms for use with MRgFUS. *Journal of Therapeutic Ultrasound*, 3(1). doi: 10.1186/s40349-015-0030-y
- Hastie, T., Friedman, J., & Tibshirani, R. (2017). *The Elements of statistical learning: data mining, inference, and prediction*. New York: Springer.
- Holzappel, G. A. (2001). Biomechanics of Soft Tissue. *Handbook of Materials Behavior Models*, 1057–1071. doi: 10.1016/b978-012443341-0/50107-1

- Jurist, J. M. (1970). In vivo determination of the elastic response of bone. I. Method of ulnar resonant frequency determination. *Physics in Medicine and Biology*, *15*(3), 417–426. doi: 10.1088/0031-9155/15/3/002
- Keller, J. A. A dictionary of terms for machinery diagnostics of gearboxes. US Army RDECOM, AED, Redstone Arsenal, AL.
- Keller, T., Weisberger, A., Ray, J., Hasan, S., Shiavi, R., & Spengler, D. (1996). Relationship between vertical ground reaction force and speed during walking, slow jogging, and running. *Clinical Biomechanics*, *11*(5), 253–259. doi: 10.1016/0268-0033(95)00068-2
- Kim, W., Voloshin, A. S., Johnson, S. H., & Simkin, A. (1993). Measurement of the Impulsive Bone Motion by Skin-Mounted Accelerometers. *Journal of Biomechanical Engineering*, *115*(1), 47–52. doi: 10.1115/1.2895470
- Liu, J., Zheng, H., Poh, P., Machens, H.-G., & Schilling, A. (2015). Hydrogels for Engineering of Perfusible Vascular Networks. *International Journal of Molecular Sciences*, *16*(7), 15997–16016. doi: 10.3390/ijms160715997
- Mckay, H. (2005). Ground reaction forces associated with an effective elementary school based jumping intervention. *British Journal of Sports Medicine*, *39*(1), 10–14. doi: 10.1136/bjsm.2003.008615
- Meirovitch, L. (1975). *Elements of vibration analysis* (2nd ed.). New York: McGraw-Hill.
- Miwa, H., & Sakai, K. (2009). Development of heart rate and respiration rate measurement system using body-sound. *2009 9th International Conference on Information Technology and Applications in Biomedicine*. doi: 10.1109/itab.2009.5394438
- Mony, P., Swaminathan, S., Gajendran, J., & Vaz, M. (2016). Quality assurance for accuracy of anthropometric measurements in clinical and epidemiological studies [Errare humanum est = to err is human]. *Indian Journal of Community Medicine*, *41*(2), 98. doi: 10.4103/0970-0218.173499
- Mouser, “POW-1644L-LWC50-B-R Omni-Directional Waterproof Microphone,” POW-1644L-LWC50-B-R datasheet, Revised Oct. 2015.
- Nikooyan, A. A., & Zadpoor, A. A. (2011). Mass–spring–damper modelling of the human body to study running and hopping – an overview. *Proceedings of the Institution of Mechanical Engineers, Part H: Journal of Engineering in Medicine*, *225*(12), 1121–1135. doi: 10.1177/0954411911424210
- Nikooyan, A. A., & Zadpoor, A. A. (2012). Effects of Muscle Fatigue on the Ground Reaction Force and Soft-Tissue Vibrations During Running: A Model Study. *IEEE Transactions on Biomedical Engineering*, *59*(3), 797–804. doi: 10.1109/tbme.2011.2179803
- Niu, W., Feng, T., Jiang, C., & Zhang, M. (2014). Peak Vertical Ground Reaction Force during Two-Leg Landing: A Systematic Review and Mathematical Modeling. *BioMed Research International*, *2014*, 1–10. doi: 10.1155/2014/126860
- Pal, S. (2014). *Design of Artificial Human Joints & Organs*. Springer Science Business Media. doi: 10.1007/978-1-4614-6255-2_2

- Perre, G. V. D., Audekercke, R. V., Martens, M., & Mulier, J. C. (1983). Identification of In-Vivo Vibration Modes of Human Tibiae by Modal Analysis. *Journal of Biomechanical Engineering*, *105*(3), 244–248. doi: 10.1115/1.3138412
- Pionteck, A., Chiementin, X., Munera, M., Murer, S., Chadeaux, D., & Rao, G. (2017). FE Model and Operational Modal Analysis of Lower Limbs. *Applied Sciences*, *7*(8), 853. doi: 10.3390/app7080853
- Scanlan, J., Li, F., Umnova, O., Rakoczy, G., Lövey, N., & Scanlan, P. (2018). Detection of Osteoporosis from Percussion Responses Using an Electronic Stethoscope and Machine Learning. *Bioengineering*, *5*(4), 107. doi: 10.3390/bioengineering5040107
- Sebo, P., Herrmann, F. R., & Haller, D. M. (2017). Accuracy of anthropometric measurements by general practitioners in overweight and obese patients. *BMC Obesity*, *4*(1). doi: 10.1186/s40608-017-0158-0
- Steele, K. M., Demers, M. S., Schwartz, M. H., & Delp, S. L. (2012). Compressive tibiofemoral force during crouch gait. *Gait & Posture*, *35*(4), 556–560. doi: 10.1016/j.gaitpost.2011.11.023
- Stern, B. (1983). The Basic Concepts of Diagnostic Ultrasound. Retrieved February 18, 2020, from <https://teachersinstitute.yale.edu/curriculum/units/1983/7/83.07.05.x.html>
- Teague, C. (2016). *A Robust System for Sensing Acoustic Emissions for Wearable Knee Health Assessment* (Doctoral dissertation). Available from SMARTech Georgia Tech Theses and Dissertations database.
- Thambyah, A., Pereira, B. P., & Wyss, U. (2005). Estimation of bone-on-bone contact forces in the tibiofemoral joint during walking. *The Knee*, *12*(5), 383–388. doi: 10.1016/j.knee.2004.12.005
- Toreyin, H., Jeong, H. K., Hersek, S., Teague, C. N., & Inan, O. T. (2016). Quantifying the Consistency of Wearable Knee Acoustical Emission Measurements During Complex Motions. *IEEE Journal of Biomedical and Health Informatics*, *20*(5), 1265–1272. doi: 10.1109/jbhi.2016.2579610
- Usta, M., Piech, D., Maccrone, R., & Hillig, W. (2003). Behavior and properties of neat and filled gelatins. *Biomaterials*, *24*(1), 165–172. doi: 10.1016/s0142-9612(02)00274-0
- Veltink, P., Liedtke, C., Droog, E., & Vanderkooij, H. (2005). Ambulatory Measurement of Ground Reaction Forces. *IEEE Transactions on Neural Systems and Rehabilitation Engineering*, *13*(3), 423–427. doi: 10.1109/tnsre.2005.847359
- “Visible Human Project: Anatomy of the Whole Human Body (Male Cadaver).” *IMAIOS*, <https://www.imaios.com/en/e-Anatomy/Thorax-Abdomen-Pelvis/Visible-Human-Project>.
- Wakeling, J. M., & Nigg, B. M. (2001). Modification of soft tissue vibrations in the leg by muscular activity. *Journal of Applied Physiology*, *90*(2), 412–420. doi: 10.1152/jap.2001.90.2.412
- Winter, D. A. (2009). *Biomechanics and Motor Control of Human Movement* (Fourth). Hoboken, NJ: John Wiley.

- Wodicka, G. R., Kraman, S. S., Zenk, G. M., & Pasterkamp, H. (1994). Measurement of Respiratory Acoustic Signals. *Chest*, *106*(4), 1140–1144. doi: 10.1378/chest.106.4.1140
- Wong, C., Zhang, Z., Lo, B. P. L., & Yang, G.-Z. (2015). Wearable Sensing for Solid Biomechanics. *IEEE Sensors Journal*, 1–1. doi: 10.1109/jsen.2015.2393883

APPENDICES

A1. Ballistic Gelatin Casting Process and Test Conditions

The ballistic gelatin used during testing was obtained from Custom Collagen Inc. and was Vyse® Professional Grade Ballistic Gelatin (250 Bloom). The mixture of warm water and gelatin consisted of 11.1% gelatin by weight. The gelatin was combined with water at 50° C in a large container, which sat in a warm water bath (also of 50° C). The solution was stirred slowly without introducing air bubbles until the gelatin was fully dissolved and a homogeneous solution was achieved. When the gelatin was fully dissolved, 1 mL of Propionic acid (99%, $\text{CH}_3\text{CH}_2\text{CO}_2\text{H}$) was added to the solution to prevent decomposition. The solution was poured into the 3D printed mold and the mold was clamped to reduce leaking. The filled mold was then placed in the refrigerator ($\approx 4^\circ\text{C}$) with the internal bar oriented vertically. Cure time for testing was approximately 48 hours. Before testing, the coupled bar and gelatin were removed from the mold and exposed to ambient temperature ($\approx 21^\circ\text{C}$) for about 2 hours. After this time, the gelatin reaches a constant internal temperature of about 16.3 °C. The temperature remains steady due to a phase change which occurs at this temperature. Testing at this temperature was preferable to testing at room temperature to ensure strong coupling between the bar and gelatin. A slightly increased stiffness of the gelatin likely resulted in comparison to nominal values, but the nominal values are lower than estimated bulk modulus of muscular tissue (see Section 2.5). All data was gathered in a one-hour window while monitoring the surface temperature of the gelatin at its axial center with a type K thermocouple (Klein Tools MM 400) to ensure there was no major

difference in temperature which might affect the model’s mechanical properties. Since the structure used during testing could not be damaged, its internal temperature could not be determined with the thermocouple. Therefore, a nearly identical secondary bar-gel structure was monitored at three different radial locations (at the same central axial location) within the secondary gel to ensure that the temperature was stable. The radial locations are described as “surface”, “shallow”, and “internal” to represent different depths that the gelatin was probed. Furthermore, the secondary bar-gel structure was weighed (Ohaus CS 5000) periodically to estimate water loss. The total lost weight associated with evaporation throughout testing was estimated to be 2.3% of the structure’s weight relative to the beginning of testing. The following tables show temperature data for the bar-gel sample used during testing as well as the secondary sample. Mass measurements are also shown for the secondary sample, which are assumed to be directly representative of the losses in the primary testing sample.

Table A1.1. Gelatin Temperature and Mass Data During Testing

Time	Elapsed Time (h:mm)	Ambient Temp. (°C)	Secondary Sample Mass (g)	Secondary Sample Surface Temp (°C)	Secondary Sample Shallow Temp (°C)	Secondary Sample Internal Temp (°C)	Primary Sample Gel Surface Temp (°C)
6:30 PM	0:00	19.6	342	15.7	16.8	15.2	15.8
6:54 PM	0:24	19.5	340	15.7	14.6	15.0	15.2
7:05 PM	0:35	19.9	337	15.5	14.8	14.9	15.3
7:12 PM	0:42	19.0	334	15.5	15.0	15.0	15.2
7:29 PM	0:59	19.7	333	15.9	15.3	15.2	15.7

A2. Supplementary Impact Hammer Model Criteria Tables: IP Transverse Impact

Table A2.1 Transverse IP Impact Model Criteria for Impact Hammer: Autospectral Amplitude vs. Peak Impact

Frequency (Hz)	Linear Model			Quadratic Model		
	R ² _{adj}	AIC	BIC	R ² _{adj}	AIC	BIC
54	0.9160	-574.8	-168.4	0.8797	-586.7	-582.4
72	0.8781	-645.53	-63.12	0.9064	-677.4	-673.0
80	0.8458	-656.55	-55.27	0.8580	-674.3	-670.0
100	0.9130	-654.2	-228.9	0.9099	-676.9	-672.6
124	0.8982	-622.3	-200.4	0.8851	-642.8	-638.5
150	0.9130	-684.6	-127.1	0.8865	-704.1	-699.8
160	0.8981	-741.2	-126.3	0.8884	-756.4	-752.0
212	0.8901	-651.4	-206.2	0.8806	-673.0	-668.6

Table A2.2. Transverse IP Impact Model Criteria for Impact Hammer: Acoustic Band Energy vs. Peak Impact

Frequency Band (Hz)	Linear Model			Quadratic Model		
	R ² _{adj}	AIC	BIC	R ² _{adj}	AIC	BIC
50 - 200	0.9266	-661.6	-659.4	0.9133	-686.9	-682.6
50 - 500	0.9076	-647.1	-645.0	0.8969	-677.2	-672.8
50 - 1200	0.9166	-661.3	-659.2	0.9004	-685.7	-681.4

Table A2.3. Transverse IP Impact Model Criteria for Impact Hammer: Autospectral Amplitude vs. Peak Impact

Frequency (Hz)	Linear Model			Quadratic Model		
	R ² _{adj}	AIC	BIC	R ² _{adj}	AIC	BIC
54	0.9777	-701.1	-265.0	0.9806	-705.1	-700.8
72	0.9533	-733.5	-158.2	0.9514	-733.5	-729.1
80	0.8465	-678.1	-84.02	0.8356	-677.1	-672.8
100	0.9869	-811.1	-329.1	0.9867	-809.1	-804.7
124	0.9763	-750.5	-316.4	0.9771	-749.8	-745.4
150	0.9745	-807.6	-241.1	0.9750	-806.4	-802.1
160	0.9522	-823.8	-235.5	0.9562	-824.4	-820.1
212	0.9840	-811.4	-376.4	0.9836	-810.1	-805.7

Table A2.4. Transverse IP Impact Model Criteria for Impact Hammer: Acoustic Band Energy vs. Peak Impact

Frequency Band (Hz)	Linear Model			Quadratic Model		
	R ² _{adj}	AIC	BIC	R ² _{adj}	AIC	BIC
50 - 200	0.9986	-948.4	-946.2	0.9985	-953.9	-949.5
50 - 500	0.9977	-930.3	-928.1	0.9985	-946.3	-942.0
50 - 1200	0.9994	-1013	-1011	0.9995	-1016	-1011

A3. Supplementary Impact Hammer Model Criteria Tables: OOP Transverse Impact

Table A3.1 Transverse OOP Impact Model Criteria for Impact Hammer: Autospectral Amplitude vs. Peak Impact

Frequency (Hz)	Linear Model			Quadratic Model		
	R ² _{adj}	AIC	BIC	R ² _{adj}	AIC	BIC
54	0.9421	-545.2	-276.3	0.9450	-564.3	-560.1
72	0.8818	-566.6	-226.9	0.8737	-569.8	-565.6
80	0.8279	-558.0	-229.8	0.8120	-559.0	-554.9
100	0.9274	-597.3	-340.0	0.9320	-611.5	-607.3
124	0.9188	-579.2	-330.1	0.9247	-595.2	-591.0
150	0.9208	-635.8	-269.1	0.9290	-654.6	-650.5
160	0.9360	-701.4	-293.0	0.9419	-717.2	-713.1
212	0.9175	-602.9	-270.4	0.9227	-627.2	-623.0

Table A3.2 Transverse OOP Impact Model Criteria for Impact Hammer: Acoustic Band Energy vs. Peak Impact

Frequency Band (Hz)	Linear Model			Quadratic Model		
	R ² _{adj}	AIC	BIC	R ² _{adj}	AIC	BIC
50 - 200	0.9402	-616.8	-614.7	0.9499	-638.5	-634.4
50 - 500	0.9297	-600.7	-598.7	0.9310	-620.7	-616.6
50 - 1200	0.9410	-620.2	-618.1	0.9462	-643.7	-639.5

Table A3. 3 Transverse OOP Impact Model Criteria for Impact Hammer: Autospectral Amplitude vs. Peak Impact

Frequency (Hz)	Linear Model			Quadratic Model		
	R^2_{adj}	AIC	BIC	R^2_{adj}	AIC	BIC
54	0.9863	-667.0	-271.9	0.9862	-665.0	-660.9
72	0.8924	-599.8	-230.1	0.8983	-598.8	-594.6
80	0.8181	-580.3	-245.5	0.8266	-578.9	-574.7
100	0.9795	-692.1	-352.8	0.9796	-690.6	-686.4
124	0.9747	-667.4	-335.4	0.9740	-665.7	-661.5
150	0.9696	-724.8	-272.2	0.9687	-723.2	-719.0
160	0.9721	-769.7	-302.9	0.9730	-768.7	-764.6
212	0.9848	-729.4	-276.3	0.9853	-733.7	-729.6

Table A3. 4 Transverse OOP Impact Model Criteria for Impact Hammer: Acoustic Band Energy vs. Peak Impact

Frequency Band (Hz)	Linear Model			Quadratic Model		
	R^2_{adj}	AIC	BIC	R^2_{adj}	AIC	BIC
50 - 200	0.9978	-817.7	-815.6	0.9978	-815.7	-811.6
50 - 500	0.9951	-783.9	-781.9	0.9952	-786.3	-782.2
50 - 1200	0.9993	-908.8	-906.8	0.9994	-913.5	-909.3

A4. MATLAB Code for Post-Processing and Figure Generation

```
clear;clc;close all;
%Program used for post-processing data for impact testing (axial,transverse IP, transverse OOP)
%Import data from one impact test, saved to excel from BK Connect
%Compare DataArraysNames cell position with DataArraysSorted
%Channel 1: Accel, Channel 2:Hammer,Channel 3:Electret 1 (003), Channel 4:Electret 2 (004)
%Written by Brandon McChristian 05/06/2020

excelSheetNameList =
[{'AxialNoCap1'},{'TransverseNoCapBendingDir'},{'TransverseNoCapAntiBendingDir'}];

%Specify which dataset to process and which figures to generate
excelSheetName = excelSheetNameList{3};
hammerData = 'Mag';%flag for switch case to determine analysis type. chose 'Mag' or 'Impulse'
fig_model_save = true;%flag to control model figure generation and autosaving to specified
directory
fig_gen_sample = false;% flag to generate sample figures

mkdir lin_figs
mkdir lin_pngs
mkdir quad_figs
mkdir quad_pngs
%C:\Users\bcmcc\Documents\MATLAB\ShepardLab\AxialTransverse
fpathlinfig =
strcat('C:\Users\bcmcc\Documents\MATLAB\ShepardLab\AxialTransverse\lin_figs');
fpathlinpng =
strcat('C:\Users\bcmcc\Documents\MATLAB\ShepardLab\AxialTransverse\lin_pngs');
fpathquadfig =
strcat('C:\Users\bcmcc\Documents\MATLAB\ShepardLab\AxialTransverse\quad_figs');
fpathquadpng =
strcat('C:\Users\bcmcc\Documents\MATLAB\ShepardLab\AxialTransverse\quad_pngs');

%Import data
[NumArray, HeaderArray] = xlsread(excelSheetName);
freq_array = NumArray(:,1);
freq_array = rmmissing(freq_array);
time_array = NumArray(:,15);

NumArrayClean = NumArray(:,~all(isnan(NumArray))); %remove NaN values from num array
where data was not collected
HeaderArrayClean = HeaderArray(:,~all(isnan(NumArray))); % do same with header array to
match indices
```

```
TransducerNamesList = [HeaderArrayClean(1,2), HeaderArrayClean(1,3),
HeaderArrayClean(1,4), HeaderArrayClean(1,5)];
```

```
%Routine to re-label empty header columns for complex FFT data (imaginary component
unlabeled)
```

```
for i = 1:length(HeaderArrayClean)
    if all(HeaderArrayClean(:,i)=='')
        HeaderArrayClean(:,i) = HeaderArrayClean(:,i-1);
    end
end
```

```
%Routine to sort data based on transducer name.
%Returns TransducerSortedData and TransducerSortedHeader
```

```
for i = 1:length(TransducerNamesList)
    TransducerSortedData{i} = zeros(size(NumArrayClean,1),size(NumArrayClean,2));
    HeaderSort = strfind(HeaderArrayClean, TransducerNamesList{i});
    TransducerSortedHeader{i} = cell(8,length(HeaderArrayClean));
    for j = 1:length(HeaderSort)
        if HeaderSort{1,j} == 1
            TransducerSortedData{i}(:,j) = NumArrayClean(:,j);
            for k=1:8
                TransducerSortedHeader{i}{k,j} = HeaderArrayClean{k,j};
            end
        end
    end
end
```

```
TransducerSortedDataClean = cell(1,length(TransducerSortedData));
TransducerSortedHeaderClean = cell(1,size(TransducerSortedData,2));
```

```
%Routine to remove empty columns from sorted transducer data and headers
```

```
for i = 1:length(TransducerSortedData)
    count = 0;
    num_row = size(TransducerSortedData{i},1);
    num_col = size(TransducerSortedData{i},2)/23;
    %TransducerSortedDataClean{i} = zeros(num_row,num_col);
    TransducerSortedHeaderPreClean{i} = cell(8,length(HeaderArrayClean));
    for j = 1:size(TransducerSortedData{i},2) %iterate through columns
        if ~isempty(TransducerSortedHeader{i}{1,j})
            count = count + 1;
            for k=1:8
                TransducerSortedDataClean{i}(:,count) = TransducerSortedData{i}(:,j);
                TransducerSortedHeaderPreClean{i}{k,count} = TransducerSortedHeader{i}{k,j};
            end
        end
    end
end
```

```

end
IsEmpty = cellfun('isempty',TransducerSortedHeaderPreClean{i});
RemovedEmpty = cell(8,size(TransducerSortedData,2));
for j =1:length(IsEmpty)
    if ~all(IsEmpty(:,j))
        for k = 1:8
            RemovedEmpty{k,j} = TransducerSortedHeaderPreClean{i}{k,j};
        end
    end
end
TransducerSortedHeaderClean{i}=RemovedEmpty;
end

%Routine to sort transducer data by data type(FFT,Time,Time-Weighted, etc.)
DataTypeHeaders = {'FFT (Autospectrum)','FFT (FRF H1) - ref. ImpulseHammer',...
    'FFT (Signal-to-Noise Ratio) - ref. ImpulseHammer','Time Block (Time - Transient
    weighted)','Time Block (Time)'};
DataArraysSorted = cell(length(DataTypeHeaders),length(TransducerNamesList));
DataArraysNames = cell(length(DataTypeHeaders),length(TransducerNamesList));
for i = 1:length(TransducerNamesList) %iterate transducers
    for j = 1:length(DataTypeHeaders) %iterate types of data (FFT, Time, Time-weighted, etc.)
        num_row = size(TransducerSortedData{4},1);
        num_col = size(TransducerSortedData{4},2)/23;
        DataArray = [];
        DataArrayName = [TransducerNamesList{i},',',DataTypeHeaders{j}];
        %for k = 1:length(TransducerSortedDataClean{i}) %sort by type of data for each
transducer
            DataTypeSort = strfind(TransducerSortedHeaderClean{i},DataTypeHeaders{j});
%binary array. True if all cell arrays in column empty
            for m =1:size(DataTypeSort,2)
                if DataTypeSort{7,m}==1
                    DataArray(:,m) = TransducerSortedDataClean{i}(:,m);
                end
                if DataTypeSort{6,m}==1
                    DataArray(:,m) = TransducerSortedDataClean{i}(:,m);
                end
            end
        end
    %end
        idx = find(~all(DataArray==0));
        DataArrayClean = DataArray(:,idx); %removes all zero columns corresponding to
other transducer/datatype combos
        DataArrayClean = rmmissing(DataArrayClean); %removes NaN values
        DataArraysSorted{j,i} = DataArrayClean;
        DataArraysNames{j,i} = DataArrayName;%named according to TransducerName +
DataType

```

```

end
end

%Create Array of impact peak values
ImpulseTransducerIndex = find(contains(TransducerNamesList,'ImpulseHammer')==1);
TimeDataTypeIndex = find(contains(DataTypeHeaders,'Time Block (Time)')==1);
PeakImpulseArray =
max(DataArraysSorted{TimeDataTypeIndex,ImpulseTransducerIndex});%Array of hammer
impact magnitude for each trial%

%Create Arrays that change based on type of impact:primary impulses,discrete freqs, and freq
bands
switch excelSheetName
case 'AxialNoCap1'
    ImpulseIntegralArray =
trapez(time_array(625:675),DataArraysSorted{TimeDataTypeIndex,ImpulseTransducerIndex}(62
5:675,:));%Row vector of hammer primary impulses, estimated with trapezoidal integration
    discrete_freq_list = [54,80,104,160,250,306,440]; %frequencies targeted for axial impact
    bndwdth = {[50,200],[50,500],[50,1200]};%bandwidth to analyze for axial impact
case 'TransverseNoCapBendingDir'
    ImpulseIntegralArray =
trapez(time_array(588:691),DataArraysSorted{TimeDataTypeIndex,ImpulseTransducerIndex}(58
8:691,:));
    discrete_freq_list = [54,72,80,100,124,150,160,212];
    bndwdth = {[50,200],[50,500],[50,1200]};
case 'TransverseNoCapAntiBendingDir'
    ImpulseIntegralArray =
trapez(time_array(588:691),DataArraysSorted{TimeDataTypeIndex,ImpulseTransducerIndex}(58
8:691,:));
    discrete_freq_list = [54,72,80,100,124,150,160,212];
    bndwdth = {[50,200],[50,500],[50,1200]};
end

%Create Cell Array of Arrays of max amplitude near discrete frequencies from Autospectrum
data for each sensor
AutospectrumIndexList = find(contains(DataArraysNames,'FFT (Autospectrum)')==1);
freq_mag_sorted = cell(1,length(TransducerNamesList));
for i = 1:length(AutospectrumIndexList)
    freq_mag_array = [];
    for j = 1:size(DataArraysSorted{AutospectrumIndexList(i),2})%iterate through number of
impacts
        for k = 1:length(discrete_freq_list)%iterate through number of chosen frequencies
            if i == 2 %for hammer impact, don't find nearest peak but instead use the discrete
frequency
                loc = find(freq_array == discrete_freq_list(k));

```

```

        freq_mag_array(k,j) =
DataArraysSorted{AutospectrumIndexList(i)}(loc,j);%magnitude of k_th freq for j_th impact
    else
        [pks,locs] = findpeaks(DataArraysSorted{AutospectrumIndexList(i)}(:,j)); %find local
maximums in freq domain
        locs_minus = (discrete_freq_list(k)/2+1)-locs; %find minimum difference between
discrete freq "guesses" and peaks
        [M,I] = min(abs(locs_minus));
        freq_mag_array(k,j) = DataArraysSorted{AutospectrumIndexList(i)}(locs(I),j);
    end
end
end
freq_mag_sorted{i} = freq_mag_array;
end

%Subroutine to determine RMS values of bandwidth (Hz)
freq_band_rms_sorted = cell(1,length(TransducerNamesList));
for i = 1:length(AutospectrumIndexList)
    freq_band_mag_array = [];
    for j = 1:size(DataArraysSorted{AutospectrumIndexList(i)},2)%iterate through number of
impacts
        for k = 1:length(bndwidth)%iterate through number of chosen frequencies
            loc_low = find(freq_array==bndwidth{k}(1)); %find index of band freq limits
            loc_high = find(freq_array==bndwidth{k}(2));
            freq_band_rms_array(k,j) =
rms(sqrt(DataArraysSorted{AutospectrumIndexList(i)}(loc_low:loc_high,j)));
        end
    end
    freq_band_rms_sorted{i} = freq_band_rms_array;
end

%% Generate Regression Models and Corresponding Figures
if fig_model_save
    MC1 = struct; %Linear Model Criterion
    MC2 = struct; %2nd Order Polynomial Model Criterion
    MCB1 = struct; %Linear Model Criterion for Bandwidth energy correlation
    MCB2 = struct; %2nd Order Polynommlial Model Criterion for Bandwidth energy correlation
    %LINEAR MODEL FOR BANDWIDTH ENERGY RMS
    for i =1:length(TransducerNamesList)
        %Struct containing model criteria for each sensor/frequency
        MCB1(i).sensor = TransducerNamesList{i};
        MCB1(i).band = bndwidth;
        MCB1(i).AIC = [];
        MCB1(i).BIC = [];
        MCB1(i).Rsquared = [];
        MCB1(i).Rsquared_adj =[];
    end
end

```

```

%Generate linear models
for j = 1:length(bndwidth)
    lin_fig_name = [excelSheetName, ', ', TransducerNamesList{i}, ', ', 'RMS of Bandwidth
Energy', ', ', num2str(bndwidth{j}(1)), ' - ', num2str(bndwidth{j}(2)), 'Hz', '.fig'];
    lin_png_name = [excelSheetName, ', ', TransducerNamesList{i}, ', ', 'RMS of Bandwidth
Energy', ', ', num2str(bndwidth{j}(1)), ' - ', num2str(bndwidth{j}(2)), 'Hz', '.png'];

    figure(i*j)
    switch hammerData
        case 'Mag'
            x = PeakImpulseArray';%column vector of impulse magnitudes
        case 'Impulse'
            x = ImpulseIntegralArray';%column vector of impulse of first hammer blow
    end
    y = freq_band_rms_sorted{i}(j,:);%column vector of frequency data
    t = table(x,y);
    lm = fitlm(t,'y~x-1');%create linear model

    %Remove outliers when line fit residuals more than 3 std from mean
    Res = lm.Residuals.Raw;
    Res_std = std(Res);
    Res_mean = mean(Res);
    Res_max = max(Res);
    Z_score = (Res - Res_mean)/Res_std; %calculate z-score of residuals
    outlier = abs(Z_score)>=3; %logical array to check if z_score>=3
    if any(outlier)%recalculate line fit after removing outliers
        rmv = find(outlier);
        x(rmv)=[];
        y(rmv)=[];
        t = table(x,y);
        lm = fitlm(t,'y~x-1');%create linear model after removing outliers
    end
    p = [lm.Coefficients.Estimate(1),0];
    x1 = linspace(0,max(x));
    y1 = polyval(p,x1);%line fit

    %save model criterion in struct
    MCB1(i).AIC(j) = lm.ModelCriterion.AIC;
    MCB1(i).BIC(j) = lm.ModelCriterion.BIC;
    MCB1(i).Rsquared_adj(j) = lm.Rsquared.adjusted;
    MCB1(i).Rsquared(j) = lm.Rsquared.ordinary;

    scatter(x,y,'x','HandleVisibility','off')
    hold on
    plot(x1,y1)

```

```

streqn = ['y = ' num2str(p(1)) 'x'];
strR2 = ['R^2(adj) = ' num2str(lm.Rsquared.adjusted)];
text(0.75*max(x),0.3*max(y),streqn,'FontSize',10)
text(0.75*max(x),0.2*max(y),strR2,'FontSize',10)

%title([excelSheetNameList{sheet} TransducerNamesList{i} 'RMS of Bandwidth
Energy ',num2str(bndwdth{j}(1)) ' - ' num2str(bndwdth{j}(2)) 'Hz'],'FontSize',10)
xlim([0 max(x)*1.1]);
ylim([0 max(y)*1.1]);
switch hammerData
    case 'Mag'
        xlabel('Peak Force (N)')
    case 'Impulse'
        xlabel('Primary Impulse (N*s)')
end
ylabel('Pressure (Pa)')
grid
legend('LS Fit','Location','southeast')
hold off

figfulldestination = fullfile(fpathlinfig, lin_fig_name);
pngfulldestination = fullfile(fpathlinpng, lin_png_name);
saveas(gca, figfulldestination)
saveas(gca, pngfulldestination)
end
close all;
end

%QUADRATIC MODEL FOR BANDWIDTH ENERGY RMS
for i = 1:length(TransducerNamesList)
    %Struct containing model criteria for each sensor/frequency
    MCB2(i).sensor = TransducerNamesList{i};
    MCB2(i).band = bndwdth;
    MCB2(i).AIC = [];
    MCB2(i).BIC = [];
    MCB2(i).Rsquared = [];
    MCB2(i).Rsquared_adj = [];
    for j = 1:length(bndwdth)
        quad_fig_name = [excelSheetName,' ',TransducerNamesList{i},' ','RMS of Bandwidth
Energy', ' ',num2str(bndwdth{j}(1)), ' - ',num2str(bndwdth{j}(2)),'Hz','.fig'];
        quad_png_name = [excelSheetName,' ',TransducerNamesList{i},' ','RMS of Bandwidth
Energy', ' ',num2str(bndwdth{j}(1)), ' - ',num2str(bndwdth{j}(2)),'Hz','.png'];

        figure(i*j)
        switch hammerData

```

```

    case 'Mag'
        x = PeakImpulseArray';%column vector of impulse magnitudes
    case 'Impulse'
        x = ImpulseIntegralArray';%column vector of impulse of first hammer blow
    end
y = freq_band_rms_sorted{i}(j,:);%column vector of bandwidth energy rms data
t = table(x,y);
lm = fitlm(t,'y~x^2-1');%create 2nd order polynomial model

%Remove outliers when line fit residuals more than 3 std from mean
Res = lm.Residuals.Raw;
Res_std = std(Res);
Res_mean = mean(Res);
Res_max = max(Res);
Z_score = (Res - Res_mean)/Res_std; %calculate z-score of residuals
outlier = abs(Z_score)>=3; %logical array to check if z_score>=3
if any(outlier)%recalculate line fit after removing outliers
    rmv = find(outlier);
    x(rmv)=[];
    y(rmv)=[];
    t = table(x,y);
    lm = fitlm(t,'y~x^2-1');%recreate model after removing outliers
end
p = [lm.Coefficients.Estimate(2),lm.Coefficients.Estimate(1),0];
x1 = linspace(0,max(x));
y1 = polyval(p,x1); %line fit

%save model criterion in struct
MCB2(i).AIC(j) = lm.ModelCriterion.AIC;
MCB2(i).BIC(j) = lm.ModelCriterion.BIC;
MCB2(i).Rsquared_adj(j) = lm.Rsquared.adjusted;
MCB2(i).Rsquared(j) = lm.Rsquared.ordinary;

scatter(x,y,'x','HandleVisibility','off')
hold on
plot(x1,y1)
streqn = ['y = ' num2str(p(1)) 'x^2 + ' num2str(p(2)) 'x'];
strR2 = ['R^2(adj) = ' num2str(lm.Rsquared.adjusted)];
text(0.6*max(x),0.3*max(y),streqn,'FontSize',10)
text(0.6*max(x),0.2*max(y),strR2,'FontSize',10)

%title([excelSheetNameList{sheet} TransducerNamesList{i} 'RMS of Bandwidth
Energy ',num2str(bndwdth{j}(1)) ' - ' num2str(bndwdth{j}(2)) 'Hz'],'FontSize',10)
xlim([0 max(x)*1.1]);
ylim([0 max(y)*1.1]);

```

```

switch hammerData
    case 'Mag'
        xlabel('Peak Force (N)')
    case 'Impulse'
        xlabel('Primary Impulse (N*s)')
end
ylabel('Pressure (Pa)')
grid
legend('LS Fit','Location','southeast')
hold off

figfulldestination = fullfile(fpathquadfig, quad_fig_name);
pngfulldestination = fullfile(fpathquadpng, quad_png_name);
saveas(gca, figfulldestination)
saveas(gca, pngfulldestination)
end
close all;
end

%LINEAR MODEL FOR RESONANT FREQUENCIES
for i = 1:length(TransducerNamesList)
    %Struct containing model criteria for each sensor/frequency
    MC1(i).sensor = TransducerNamesList{i};
    MC1(i).freq = discrete_freq_list;
    MC1(i).AIC = [];
    MC1(i).BIC = [];
    MC1(i).Rsquared = [];
    MC1(i).Rsquared_adj = [];
    %Generate linear models
    for j = 1:length(discrete_freq_list)
        lin_fig_name = [excelSheetName, '', TransducerNamesList{i}, ', ', 'FFT (Autospectrum)',
            ',num2str(discrete_freq_list(j)),', ', 'Hz', '.fig'];
        lin_png_name = [excelSheetName, '', TransducerNamesList{i}, ', ', 'FFT (Autospectrum)',
            ',num2str(discrete_freq_list(j)),', ', 'Hz', '.png'];

        figure(i*j)
        switch hammerData
            case 'Mag'
                x = PeakImpulseArray';%column vector of impulse magnitudes
            case 'Impulse'
                x = ImpulseIntegralArray';%column vector of impulse of first hammer blow
        end
        y = sqrt(freq_mag_sorted{i}(j,:));%column vector of frequency data
        t = table(x,y);
        lm = fitlm(t,'y~x-1');%create linear model
    end
end

```

```

%Remove outliers when line fit residuals more than 3 std from mean
Res = lm.Residuals.Raw;
Res_std = std(Res);
Res_mean = mean(Res);
Res_max = max(Res);
Z_score = (Res - Res_mean)/Res_std; %calculate z-score of residuals
outlier = abs(Z_score)>=3; %logical array to check if z_score>=3
if any(outlier)%recalculate line fit after removing outliers
    rmv = find(outlier);
    x(rmv)=[];
    y(rmv)=[];
    t = table(x,y);
    lm = fitlm(t,'y~x-1');%create linear model after removing outliers
end
p = [lm.Coefficients.Estimate(1),0];
x1 = linspace(0,max(x));
y1 = polyval(p,x1);%line fit

%save model criterion in struct
MC1(i).AIC(j) = lm.ModelCriterion.AIC';
MC1(i).BIC(j) = lm.ModelCriterion.BIC';
MC1(i).Rsquared_adj(j) = lm.Rsquared.adjusted';
MC1(i).Rsquared(j) = lm.Rsquared.ordinary';

scatter(x,y,'x','HandleVisibility','off')
hold on
plot(x1,y1)
streqn = ['y = ' num2str(p(1)) 'x'];
strR2 = ['R^2(adj) = ' num2str(lm.Rsquared.adjusted)];
text(0.75*max(x),0.3*max(y),streqn,'FontSize',10)
text(0.75*max(x),0.2*max(y),strR2,'FontSize',10)

%title([excelSheetNameList{sheet} TransducerNamesList{i} 'Autospectrum Amplitude
at ' num2str(discrete_freq_list(j)) ' Hz'],'FontSize',10)
xlim([0 max(x)*1.1]);
ylim([0 max(y)*1.1]);
switch hammerData
    case 'Mag'
        xlabel('Peak Force (N)')
    case 'Impulse'
        xlabel('Primary Impulse (N*s)')
end
ylabel('Pressure (Pa)')
grid

```

```

legend('LS Fit','Location','southeast')
hold off

figfulldestination = fullfile(fpathlinfig, lin_fig_name);
pngfulldestination = fullfile(fpathlinpng, lin_png_name);
saveas(gca, figfulldestination)
saveas(gca, pngfulldestination)
end
close all;
end

%QUADRATIC MODEL FOR RESONANT FREQUENCIES
for i = 1:length(TransducerNamesList)
    %Struct containing model criteria for each sensor/frequency
    MC2(i).sensor = TransducerNamesList{i};
    MC2(i).freq = discrete_freq_list';
    MC2(i).AIC = [];
    MC2(i).BIC = [];
    MC2(i).Rsquared = [];
    MC2(i).Rsquared_adj = [];
    for j = 1:length(discrete_freq_list)
        quad_fig_name = [excelSheetName, '', TransducerNamesList{i}, '', 'FFT (Autospectrum)',
',num2str(discrete_freq_list(j))', '', 'Hz', '.fig'];
        quad_png_name = [excelSheetName, '', TransducerNamesList{i}, '', 'FFT
(Autospectrum)', '', num2str(discrete_freq_list(j))', '', 'Hz', '.png'];

        figure(i*j)
        switch hammerData
            case 'Mag'
                x = PeakImpulseArray'; %column vector of impulse magnitudes
            case 'Impulse'
                x = ImpulseIntegralArray'; %column vector of impulse of first hammer blow
        end
        y = sqrt(freq_mag_sorted{i}(j,:)); %column vector of frequency data
        t = table(x,y);
        lm = fitlm(t, 'y~x^2-1'); %create 2nd order polynomial model

        %Remove outliers when line fit residuals more than 3 std from mean
        Res = lm.Residuals.Raw;
        Res_std = std(Res);
        Res_mean = mean(Res);
        Res_max = max(Res);
        Z_score = (Res - Res_mean)/Res_std; %calculate z-score of residuals
        outlier = abs(Z_score)>=3; %logical array to check if z_score>=3
        if any(outlier)%recalculate line fit after removing outliers

```

```

    rmv = find(outlier);
    x(rmv)=[];
    y(rmv)=[];
    t = table(x,y);
    lm = fitlm(t,'y~x^2-1');%recreate model after removing outliers
end
p = [lm.Coefficients.Estimate(2),lm.Coefficients.Estimate(1),0];
x1 = linspace(0,max(x));
y1 = polyval(p,x1);    %line fit

%save model criterion in struct
MC2(i).AIC(j) = lm.ModelCriterion.AIC';
MC2(i).BIC(j) = lm.ModelCriterion.BIC';
MC2(i).Rsquared_adj(j) = lm.Rsquared.adjusted';
MC2(i).Rsquared(j) = lm.Rsquared.ordinary';

scatter(x,y,'x','HandleVisibility','off')
hold on
plot(x1,y1)
streqn = ['y = ' num2str(p(1)) 'x^2 + ' num2str(p(2)) 'x'];
strR2 = ['R^2(adj) = ' num2str(lm.Rsquared.adjusted)];
text(0.6*max(x),0.3*max(y),streqn,'FontSize',10)
text(0.6*max(x),0.2*max(y),strR2,'FontSize',10)

%title([excelSheetNameList{sheet} TransducerNamesList{i} 'Autospectrum Amplitude
at ' num2str(discrete_freq_list(j)) ' Hz'],'FontSize',10)
xlim([0 max(x)*1.1]);
ylim([0 max(y)*1.1]);
switch hammerData
    case 'Mag'
        xlabel('Peak Force (N)')
    case 'Impulse'
        xlabel('Primary Impulse (N*s)')
end
ylabel('Pressure (Pa)')
grid
legend('LS Fit','Location','southeast')
hold off

figfulldestination = fullfile(fpathquadfig, quad_fig_name);
pngfulldestination = fullfile(fpathquadpng, quad_png_name);
saveas(gca, figfulldestination)
saveas(gca, pngfulldestination)
end
close all;

```

```

end

%%Create tables of Model Criteria for each LS regression model
tabl1 = table(discrete_freq_list',MC1(3).Rsquared_adj',MC1(3).AIC',MC1(3).BIC');%Electret
1 Linear
tabl2 = table(discrete_freq_list',MC1(4).Rsquared_adj',MC1(4).AIC',MC1(4).BIC');%Electret
2 Linear
tabl3 = table(discrete_freq_list',MC1(1).Rsquared_adj',MC1(1).AIC',MC1(1).BIC');%Accel
Linear
tabl4 = table(discrete_freq_list',MC1(2).Rsquared_adj',MC1(2).AIC',MC1(1).BIC');%Hammer
Linear

tabq1 = table(discrete_freq_list',MC2(3).Rsquared_adj',MC2(3).AIC',MC2(3).BIC');%Electret
1 Quadratic
tabq2 = table(discrete_freq_list',MC2(4).Rsquared_adj',MC2(4).AIC',MC2(4).BIC');%Electret
2 Quadratic
tabq3 = table(discrete_freq_list',MC2(1).Rsquared_adj',MC2(1).AIC',MC2(1).BIC');%Accel
Quadratic
tabq4 = table(discrete_freq_list',MC2(2).Rsquared_adj',MC2(2).AIC',MC2(2).BIC');%Accel
Quadratic

tabbndl1 = table(bndwidth',MCB1(3).Rsquared_adj',MCB1(3).AIC',MCB1(3).BIC');%Electret
1 Linear);
tabbndl2 = table(bndwidth',MCB1(4).Rsquared_adj',MCB1(4).AIC',MCB1(4).BIC');%Electret
2 Linear);
tabbndl3 = table(bndwidth',MCB1(1).Rsquared_adj',MCB1(1).AIC',MCB1(1).BIC');%Accel
Linear);
tabbndl4 =
table(bndwidth',MCB1(2).Rsquared_adj',MCB1(2).AIC',MCB1(2).BIC');%Hammer Linear);

tabbndq1 = table(bndwidth',MCB2(3).Rsquared_adj',MCB2(3).AIC',MCB2(3).BIC');%Electret
1 Linear);
tabbndq2 = table(bndwidth',MCB2(4).Rsquared_adj',MCB2(4).AIC',MCB2(4).BIC');%Electret
1 Linear);
tabbndq3 = table(bndwidth',MCB2(1).Rsquared_adj',MCB2(1).AIC',MCB2(1).BIC');%Electret
1 Linear);
tabbndq4 = table(bndwidth',MCB2(2).Rsquared_adj',MCB2(2).AIC',MCB2(2).BIC');%Electret
1 Linear);
end

if fig_gen_sample
    dbref = 20e-6;

    switch excelSheetName %switch case for which test is to have samples plotted

```

```

case 'AxialNoCap1'
    i1 = 32;% "impact 1" used for sample plots
    i2 = 41;
    i3 = 34;
case 'TransverseNoCapBendingDir'
    i1 = 47;
    i2 = 43;
    i3 = 58;
case 'TransverseNoCapAntiBendingDir'
    i1 = 55;
    i2 = 54;
    i3 = 53;
end
figure (1) %plot sample impulse in time domain (zoomed)
plot(time_array(625:1025),DataArraysSorted{ 10}(625:1025,i1),'-','color',[0, 0.4470,
0.7410]);%blue
hold on
plot(time_array(625:1025),DataArraysSorted{ 10}(625:1025,i2),'--','color',[0.8500, 0.3250,
0.0980]);%orange
plot(time_array(625:1025),DataArraysSorted{ 10}(625:1025,i3),'-','color',[0.9290, 0.6940,
0.1250]);%yellow
%title('Sample Time Data for Impulse Hammer','Units', 'normalized', 'Position', [0.5, 1, 0]);
xlabel('Time (s)')
ylabel('Force (N)')
legend('Impact 1','Impact 2', 'Impact 3')
hold off

figure (2) %plot sample electret signal (003) in time domain
plot(time_array,DataArraysSorted{ 15}(:,i1),'-','color',[0, 0.4470, 0.7410]);%blue
hold on
plot(time_array,DataArraysSorted{ 15}(:,i2),'--','color',[0.8500, 0.3250, 0.0980]);%orange
plot(time_array,DataArraysSorted{ 15}(:,i3),'-','color',[0.9290, 0.6940, 0.1250]);%yellow
%title('Sample Time Signal for Electret 1')
xlabel('Time (s)')
ylabel('Pressure (Pa)')
legend('Impact 1','Impact 2', 'Impact 3')
hold off

figure (3) %plot sample autospectrum for 003 up to 1200 Hz (linear)
plot(freq_array(1:600),DataArraysSorted{ AutospectrumIndexList(3)}(1:600,32),'-','color',[0,
0.4470, 0.7410]);%blue
hold on
plot(freq_array(1:600),DataArraysSorted{ AutospectrumIndexList(3)}(1:600,41),'--
','color',[0.8500, 0.3250, 0.0980]);%orange

```

```

    plot(freq_array(1:600),DataArraysSorted{AutospectrumIndexList(3)}(1:600,34),'-
','color',[0.9290, 0.6940, 0.1250]);%yellow
    xlabel('Frequency (Hz)')
    ylabel('Pa^2')
    legend('Impact 1','Impact 2', 'Impact 3')
    hold off
    %title('Sample Autospectrum Data for Electret 1')

```

figure (4) %plot sample autospectrum for 003 up to 500 Hz (dB)

```

plot(freq_array(1:250),20*log10(sqrt(DataArraysSorted{AutospectrumIndexList(3)}(1:250,i1))/
dbref),'-','color',[0, 0.4470, 0.7410]);%blue
    hold on

```

```

plot(freq_array(1:250),20*log10(sqrt(DataArraysSorted{AutospectrumIndexList(3)}(1:250,i2))/
dbref),'-','color',[0.8500, 0.3250, 0.0980]);%orange

```

```

plot(freq_array(1:250),20*log10(sqrt(DataArraysSorted{AutospectrumIndexList(3)}(1:250,i3))/
dbref),'-','color',[0.9290, 0.6940, 0.1250]);%yellow
    xlabel('Frequency (Hz)')
    ylabel('SPL (dB)')
    legend('Impact 1','Impact 2', 'Impact 3')
    hold off
    %title('Sample Autospectrum Data for Electret 1')

```

figure (5) %plot sample autospectrum for hammer up to 1200 Hz (dB)

```

plot(freq_array(1:600),20*log10(sqrt(DataArraysSorted{AutospectrumIndexList(2)}(1:600,i1))/
dbref),'-','color',[0, 0.4470, 0.7410]);%blue
    hold on

```

```

plot(freq_array(1:600),20*log10(sqrt(DataArraysSorted{AutospectrumIndexList(2)}(1:600,i2))/
dbref),'-','color',[0.8500, 0.3250, 0.0980]);%orange

```

```

plot(freq_array(1:600),20*log10(sqrt(DataArraysSorted{AutospectrumIndexList(2)}(1:600,i3))/
dbref),'-','color',[0.9290, 0.6940, 0.1250]);%yellow
    xlabel('Frequency (Hz)')
    ylabel('SPL (dB)')
    legend('Impact 1','Impact 2', 'Impact 3')
    hold off
    %title('Sample Autospectrum Data for Electret 1')

```

figure (6) %plot sample autospectrum for 004 up to 500 Hz(dB)

```

plot(freq_array(1:250),20*log10(sqrt(DataArraysSorted{AutospectrumIndexList(4)}(1:250,i1))/
dbref),'-','color',[0, 0.4470, 0.7410]);%blue
hold on

```

```

plot(freq_array(1:250),20*log10(sqrt(DataArraysSorted{AutospectrumIndexList(4)}(1:250,i2))/
dbref),'-','color',[0.8500, 0.3250, 0.0980]);%orange

```

```

plot(freq_array(1:250),20*log10(sqrt(DataArraysSorted{AutospectrumIndexList(4)}(1:250,i3))/
dbref),'-','color',[0.9290, 0.6940, 0.1250]);%yellow
%title('Sample Autospectrum Data for Electret 2')
xlabel('Frequency (Hz)')
ylabel('SPL (dB)','interpreter','Tex')
legend('Impact 1','Impact 2', 'Impact 3')
hold off

```

figure (7) %plot sample autospectrum for bar accel up to 500 Hz (log)

```

plot(freq_array(1:250),10*log10(sqrt(DataArraysSorted{AutospectrumIndexList(1)}(1:250,i1))),
'-','color',[0, 0.4470, 0.7410]);%blue
hold on

```

```

plot(freq_array(1:250),10*log10(sqrt(DataArraysSorted{AutospectrumIndexList(1)}(1:250,i2))),
'-','color',[0.8500, 0.3250, 0.0980]);%orange

```

```

plot(freq_array(1:250),10*log10(sqrt(DataArraysSorted{AutospectrumIndexList(1)}(1:250,i3))),
'-','color',[0.9290, 0.6940, 0.1250]);%yellow
%title('Sample Autospectrum Data for Bar Accel')
xlabel('Frequency (Hz)')
ylabel('10log_{10}[a(m/s^2)]')
legend('Impact 1','Impact 2', 'Impact 3')
hold off

```

figure (8) %plot sample autospectrum for bar accel (log) 1200Hz

```

plot(freq_array(1:600),10*log10(DataArraysSorted{AutospectrumIndexList(1)}(1:600,i1)),'-
','color',[0, 0.4470, 0.7410]);%blue
hold on
plot(freq_array(1:600),10*log10(DataArraysSorted{AutospectrumIndexList(1)}(1:600,i2)),'-
','color',[0.8500, 0.3250, 0.0980]);%orange
plot(freq_array(1:600),10*log10(DataArraysSorted{AutospectrumIndexList(1)}(1:600,i3)),'-
','color',[0.9290, 0.6940, 0.1250]);%yellow
%title('Sample Autospectrum Data for Bar Accel')
xlabel('Frequency (Hz)')
ylabel('10log_{10}(a)')
legend('Impact 1','Impact 2', 'Impact 3')

```

```
hold off
```

```
figure (9) %plot sample autospectrum for bar accel (linear) 1200Hz
plot(freq_array(1:600),DataArraysSorted{AutospectrumIndexList(1)}(1:600,i1),'-','color',[0,
0.4470, 0.7410]);%blue
hold on
plot(freq_array(1:600),DataArraysSorted{AutospectrumIndexList(1)}(1:600,i2),'-
','color',[0.8500, 0.3250, 0.0980]);%orange
plot(freq_array(1:600),DataArraysSorted{AutospectrumIndexList(1)}(1:600,i3),'-
','color',[0.9290, 0.6940, 0.1250]);%yellow
%title('Sample Autospectrum Data for Bar Accel')
xlabel('Frequency (Hz)')
ylabel('10log_{10}(a)')
legend('Impact 1','Impact 2', 'Impact 3')
hold off
```

```
figure (10) %plot sample autospectrum for bar accel (linear) 10000Hz
plot(freq_array(1:5000),DataArraysSorted{AutospectrumIndexList(1)}(1:5000,i1),'-
','color',[0, 0.4470, 0.7410]);%blue
hold on
plot(freq_array(1:5000),DataArraysSorted{AutospectrumIndexList(1)}(1:5000,i2),'-
','color',[0.8500, 0.3250, 0.0980]);%orange
plot(freq_array(1:5000),DataArraysSorted{AutospectrumIndexList(1)}(1:5000,i3),'-
','color',[0.9290, 0.6940, 0.1250]);%yellow
%title('Sample Autospectrum Data for Bar Accel')
xlabel('Frequency (Hz)')
ylabel('a^2 (m/s^2)')
legend('Impact 1','Impact 2', 'Impact 3')
hold off
```

```
figure (11) %plot sample autospectrum for bar accel (log) 10000Hz
```

```
plot(freq_array(1:5000),10*log10(sqrt(DataArraysSorted{AutospectrumIndexList(1)}(1:5000,i1
))),'-','color',[0, 0.4470, 0.7410]);%blue
```

```
hold on
```

```
plot(freq_array(1:5000),10*log10(sqrt(DataArraysSorted{AutospectrumIndexList(1)}(1:5000,i2
))),'-','color',[0.8500, 0.3250, 0.0980]);%orange
```

```
plot(freq_array(1:5000),10*log10(sqrt(DataArraysSorted{AutospectrumIndexList(1)}(1:5000,i3
))),'-','color',[0.9290, 0.6940, 0.1250]);%yellow
```

```
%title('Sample Autospectrum Data for Bar Accel')
```

```
xlabel('Frequency (Hz)')
```

```
ylabel('10log_{10}[a(m/s^2)]')
```

```
legend('Impact 1','Impact 2', 'Impact 3')
```

```
hold off
```

```
figure (12) %plot sample accel signal in time domain
```

```
plot(time_array,DataArraysSorted{5}(:,i1),'-','color',[0, 0.4470, 0.7410]);%blue
```

```
hold on
```

```
plot(time_array,DataArraysSorted{5}(:,i2),'-','color',[0.8500, 0.3250, 0.0980]);%orange
```

```
plot(time_array,DataArraysSorted{5}(:,i3),'-','color',[0.9290, 0.6940, 0.1250]);%yellow
```

```
%title('Sample Time Signal for Electret 1')
```

```
xlabel('Time (s)')
```

```
ylabel('a (m/s^2)')
```

```
legend('Impact 1','Impact 2','Impact 3')
```

```
hold off
```

```
figure (13) %plot sample accel signal in time domain (zoom)
```

```
plot(time_array(625:2000),DataArraysSorted{5}(625:2000,i1),'-','color',[0, 0.4470,  
0.7410]);%blue
```

```
hold on
```

```
plot(time_array(625:2000),DataArraysSorted{5}(625:2000,i2),'-','color',[0.8500, 0.3250,  
0.0980]);%orange
```

```
plot(time_array(625:2000),DataArraysSorted{5}(625:2000,i3),'-','color',[0.9290, 0.6940,  
0.1250]);%yellow
```

```
%title('Sample Time Signal for Electret 1')
```

```
xlabel('Time (s)')
```

```
ylabel('a (m/s^2)')
```

```
legend('Impact 1','Impact 2','Impact 3')
```

```
hold off
```

```
end
```